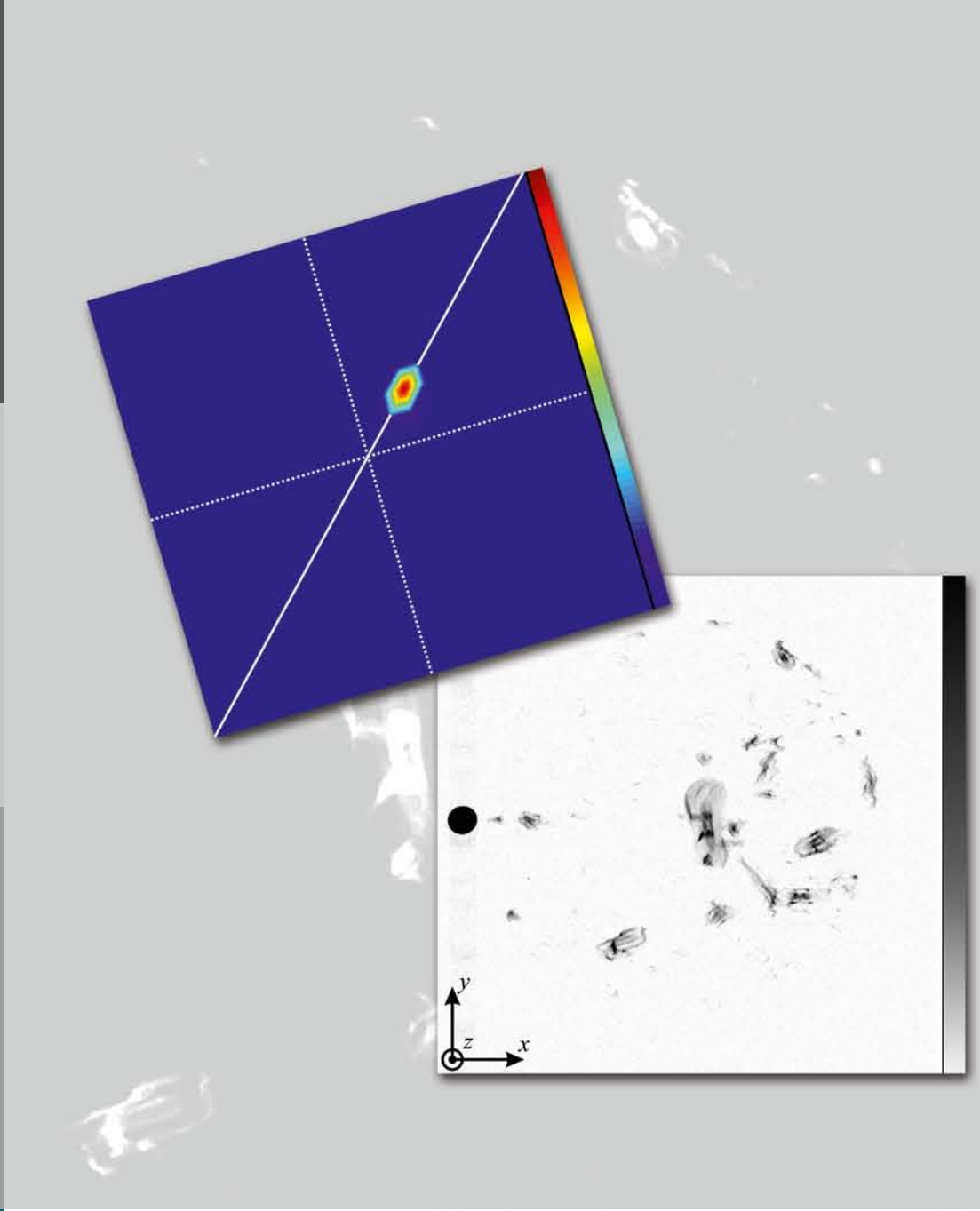

Diffusion and Flow Investigations in Natural Porous Media by Nuclear Magnetic Resonance

Natascha Spindler

Mitglied der Helmholtz-Gemeinschaft

JÜLICH
FORSCHUNGSZENTRUM

Diffusion and Flow Investigations in Natural Porous Media by Nuclear Magnetic Resonance

Von der Fakultät für Mathematik, Informatik und Naturwissenschaften der RWTH Aachen University zur Erlangung des akademischen Grades einer Doktorin der Naturwissenschaften genehmigte Dissertation

vorgelegt von

Diplom-Physikerin
Natascha Spindler
aus Naila

Berichter:
Universitätsprofessor Dr. rer. nat. Bernhard Blümich
Universitätsprofessor Dr. rer. nat. Harry Vereecken

Tag der mündlichen Prüfung: 19. April 2011

Forschungszentrum Jülich GmbH
Institut für Bio- und Geowissenschaften (IBG)
Agrosphäre (IBG-3)

Diffusion and Flow Investigations in Natural Porous Media by Nuclear Magnetic Resonance

Natascha Spindler

Schriften des Forschungszentrums Jülich
Reihe Energie & Umwelt / Energy & Environment Band / Volume 112

ISSN 1866-1793 ISBN 978-3-89336-719-1

Bibliographic information published by the Deutsche Nationalbibliothek.
The Deutsche Nationalbibliothek lists this publication in the Deutsche Nationalbibliografie; detailed bibliographic data are available in the Internet at http://dnb.d-nb.de.

Publisher and Distributor:	Forschungszentrum Jülich GmbH Zentralbibliothek 52425 Jülich Phone +49 (0) 24 61 61-53 68 · Fax +49 (0) 24 61 61-61 03 e-mail: zb-publikation@fz-juelich.de Internet: http://www.fz-juelich.de/zb
Cover Design:	Grafische Medien, Forschungszentrum Jülich GmbH
Printer:	Grafische Medien, Forschungszentrum Jülich GmbH
Copyright:	Forschungszentrum Jülich 2011

Schriften des Forschungszentrums Jülich
Reihe Energie & Umwelt / Energy & Environment Band / Volume 112

D 82 (Diss.,RWTH Aachen University, 2011)

ISSN 1866-1793
ISBN 978-3-89336-719-1

There are two ways to live :

You can live as if nothing is a miracle;
you can live as if everything is a miracle.

Albert Einstein

Zusammenfassung

Der Klimawandel und die wachsende Weltbevölkerung üben extremen Druck auf die Sicherstellung der Nahrungsversorgung der Menschen aus. Einen wesentlichen Aspekt hierbei stellt die Möglichkeit dar, die Kultivierung von Nutzpflanzen an die sich ändernden Umweltbedingungen anzupassen. Dies ist eine starke Motivation, sich für die Mechanismen der Wasseraufnahme von pflanzlichen Wurzeln zu interessieren. Um zu einem verbesserten Verständnis dieser Mechanismen zu gelangen ist es notwendig, die Bewegung von Wassermolekülen sowohl in Wurzeln als auch im Boden hin zu den Wurzeln zu analysieren.

Ziel dieser Arbeit war die Bestimmung der Wasserbewegung in natürlichen porösen Medien wie etwa Pflanzenwurzeln oder Böden durch die Nutzung von verschiedenen Methoden der Kernspinresonanz (engl. nuclear magnetic resonance, NMR). Diese in der medizinischen Diagnostik verbreitete Technik erlaubt die nichtinvasive Untersuchung von intakten Pflanzen und natürlichen Böden. Da die Modellierung der Wasseraufnahme von Wurzeln eine vollständige, dreidimensionale Rekonstruktion des Wurzelskeletts verlangt, erscheint die Magnetresonanztomographie (engl. magnetic resonance imaging, MRI) sehr vielversprechend. Aus der räumlichen Analyse der Probenantwort auf magnetische Pulse kann auf Wasserverteilung und -bewegung innerhalb der Probe geschlossen werden.

Im ersten Teil dieser Arbeit wird dargestellt, dass herkömmliche NMR-Bildgebungsverfahren zu einer nur unvollständigen Darstellung der Wurzelstruktur führen. Die Ursache liegt in Suszeptibilitätseffekten an Übergängen verschiedener Materialien. Um diese Effekte zu umgehen, wurde in dieser Arbeit Diffusion Tensor Imagings (DTI) auf die Anforderungen von Pflanzenwurzeln übertragen und erstmals erfolgreich angewandt. DTI ist ein weiteres in der medizinischen Forschung bekanntes NMR-Verfahren, welches die diffusive Verschiebung von Molekülen innerhalb des Untersuchungsobjekts mit hoher räumlicher Auflösung bestimmt. In Pflanzenwurzeln ist die Molekülbewegung beispielsweise entlang der Zellwand eingeschränkt, damit ist das Diffusionsvermögen begrenzt. Besteht wie im Beispiel der Zellwand

eine Einschränkung nicht in alle Raumrichtungen gleichermaßen, ist die Diffusion anisotrop. Mathematisch kann ein solches Verhalten mit einem Tensor beschrieben werden. Mit DTI werden Diffusionstensoren an verschiedenen Orten innerhalb der Probe bestimmt. Die Herausforderung dabei war, trotz des sehr geringen Verhältnisses von Signalstärke zum Umgebungsrauschen bei Pflanzenwurzeln, DTI erfolgreich durchzuführen. Aus diesem Grund wurde in dieser Arbeit ein alternatives Verfahren zur herkömmlichen Datenauswertung eingeführt. Damit war es erstmalig möglich, durch eine dreidimensionale Tensorvisualisierung einen zusammenhängenden Wurzelstrang zu rekonstruieren.

Einen zweiten Schwerpunkt bildet die ortsgemittelte Bestimmung von makroskopischer und mikroskopischer Diffusion in natürlichem Boden. Hierbei werden Korrelationen von Diffusion in unterschiedliche Raumrichtungen mittels der Diffusion Diffusion Correlation Spectroscopy (DDCOSY) untersucht. Böden wie beispielsweise natürliche Sande besitzen starke interne Magnetfeldgradienten, die das NMR-Signal beeinflussen. Des Weiteren wird in natürlichen Sanden das NMR-Signal durch eine sehr kurze T_2-Relaxationszeit beeinträchtigt. Um diesen beiden Einschränkungen entgegenzuwirken, wurde eine neuartige Pulssequenz implementiert. Durch die Halbierung der Pulssequenzdauer sowie der Erweiterung mit alternierenden gepulsten Magnetfeldgradienten (engl. alternating pulsed magnetic field gradient, APFG) entstand die Pulssequenz 13-interval sDDCOSY. Mit dieser Pulssequenz war es möglich, die vollständige Isotropie des natürlichen Sandes zu zeigen.

Eine weitere Möglichkeit zur Quantifizierung von Wasserbewegungen in natürlichen porösen Medien bietet die direkte Messung der Geschwindigkeit. Im dritten Teil dieser Arbeit wurde mittels NMR-Flussbildgebung der Wasserfluss durch natürlichen Sand analysiert. Da auch hier interne Gradienten das NMR-Signal beeinflussen, war die Erweiterung der herkömmlichen Flussbildgebung durch APFGs zur Reduktion der Gradienten notwendig, was mit der Pulssequenz 13-interval STEMSI realisiert wurde. Bei hohen Flussgeschwindigkeiten war eine Abweichung von der erwarteten, extern angelegten Geschwindigkeit zu beobachten. Diese Abweichung ließ sich als T_1-ähnliche Relaxation charakterisieren. Nach einer entsprechenden Korrektur des NMR-Signals stimmten Messwerte und Erwartungswert für alle Geschwindigkeiten sehr gut überein. Hiermit war es schließlich möglich, eine untere Grenze von detektierbaren Flüssen im untersuchten natürlichen Sand zu finden. Diese lag bei $v = 60\,\mu\mathrm{m\,s^{-1}}$ und ist damit die bislang kleinste mit NMR detektierte Flussgeschwindigkeit in porösen Medien, die Einflüsse von internen Gradienten zeigen.

Abstract

Climate change and a growing global population impose severe pressure on securing the supply of nutrition to mankind. A crucial aspect thereby is the possibility to adopt the cultivation of crops to the changing climatic conditions. This is a strong motivation for being interested in root water uptake of plants. To obtain a better understanding of these mechanisms, analysis of water motion inside and towards plant roots in natural soil are essential.

This work aims on the determination of water motion in natural porous media such as roots and soil using different techniques of nuclear magnetic resonance (NMR). NMR is known from medical diagnosis and allows non-invasive investigations of natural soil and intact plants. Therefore, NMR is best suited for investigating root water uptake processes. Since modeling of root water uptake processes requires an unambiguous three-dimensional reconstruction of the root skeleton, magnetic resonance imaging (MRI) is an appropriate technique for this challenge. From the spatial analysis of the answer of the sample to excitation with radio frequency (rf) pulses, the water distribution and motion inside the sample can be determined.

This thesis shows how common imaging techniques introduce gaps in reconstructed roots due to susceptibility effects. To compensate for these effects, diffusion tensor imaging (DTI) was transformed to the requirements of plant roots and successfully applied for the first time. DTI is also an NMR-technique known from medical research, which detects local diffusive displacements of water molecules with high spatial resolution. Restrictions such as cell walls in plant roots limit the diffusion. If such restrictions are spatially dependent, diffusion is called anisotropic. This can be mathematically expressed by a tensor, describing the local anisotropy. DTI determines the diffusion tensors at different positions in the sample. Since DTI on plant roots shows typically a low signal to noise ratio (SNR), this work presents a new approach for data analyzing beside the common medical procedure. In the end, it was possible to visualize a single root of the root skeleton three-dimensionally by measuring diffusion tensors inside the root.

Furthermore, non-localized NMR diffusion measurements were performed identifying isotropy of natural soil on the macroscopic and microscopic scale. Hereby, correlations of diffusion in different spatial directions are investigated by diffusion diffusion correlation spectroscopy (DDCOSY). Soils such as natural sand have strong internal magnetic field gradients that impact on the NMR signal. Additionally, the signal intensity is lowered by short T_2 relaxation times. To challenge these effects a new pulse sequence taking into account both internal magnetic field gradients and short relaxation time was developed. Shortening the DDCOSY pulse sequence and extending the sequence with alternating pulsed magnetic field gradients (APFG) reduce the influence of internal magnetic field gradients. The new developed pulse sequence is named 13-interval sDDCOSY. Using this pulse sequence it was possible to show that natural sand is macroscopically and microscopically isotropic.

Another approach of detecting water motion in natural porous media is the direct flow measurement. In this thesis flow measurement was realized by velocity imaging of water flowing through natural sand. Internal magnetic field gradients again distort the NMR signal. Therefore, also the common approach of velocity mapping was extended with APFGs to a new pulse sequence named 13-interval STEMSI. At high applied pore flow the velocity detected by NMR deviated from the externally measured velocity. This could be explained with relaxation effects similar to T_1 relaxation, which can be corrected. For slow velocities, the NMR detected mean pore flow velocities agree with the applied velocities. Finally, a lower limit value for MRI detectable velocities was found at $v_{\mathrm{appl,min}} = 60\,\mu\mathrm{m\,s^{-1}}$. This limit is so far the lowest velocity detected with nuclear magnetic resonance in porous media influenced by internal magnetic field gradients.

Contents

1. Introduction **1**

2. Equipment and materials **7**

2.1. NMR scanners 7

2.1.1. 7 T scanner for root imaging and DTI 7

2.1.2. 9.4 T scanner for diffusion investigations and velocity imaging on natural sand 7

2.2. Further experimental equipment 8

2.2.1. Optical microscopy of plant roots 9

2.2.2. Peristaltic pump for induced water flow through natural sand 9

2.3. Samples used for NMR experiments 9

2.3.1. Growing conditions of the maize plant 9

2.3.2. Properties of the natural sand used for flow investigations . . 11

3. Diffusion in natural porous media **13**

3.1. Restricted self-diffusion 15

3.2. Anisotropic diffusion 15

3.3. Flow in porous media 16

4. Theory of NMR and MRI **17**

4.1. Fundamentals of nuclear magnetic resonance 17

4.1.1. Naming convention 17

4.1.2. Nuclear spins in the static magnetic field 18

4.1.3. Nuclear spins in a radio frequency alternating field 19

4.1.4. Nuclear spins in magnetic field gradients 22

4.2. Magnetic resonance imaging 23

4.2.1. NMR signal from the $\boldsymbol{k}$-space and the $\boldsymbol{q}$-space 23

4.2.2. The slice selective gradient $\boldsymbol{G}_\mathrm{s}$ and multislicing 26

4.2.3. The read out gradient $\boldsymbol{G}_{\mathrm{r}}$ and the phase-encoding gradient $\boldsymbol{G}_{\mathrm{p}}$ 26

5. Pulse sequences – methods currently known 29

5.1. 1D pulse sequences 29
5.1.1. The spin echo 29
5.1.2. NMR with pulsed field gradients for probing diffusion and flow 30
5.1.3. The influence of constant magnetic field gradients 35
5.1.4. The stimulated echo 37
5.1.5. Stimulated echo with pulsed field gradients 38
5.1.6. The 13-interval pulse sequence 40
5.1.7. Theory of PFG NMR with anisotropic diffusion 42
5.2. The 2D pulse sequence DDCOSY 45
5.3. Magnetic resonance imaging pulse sequences 50
5.3.1. Imaging with the spin echo pulse sequence 50
5.3.2. Diffusion tensor imaging pulse sequence 52
5.3.3. The stimulated echo pulse sequence combined with imaging 54
5.3.4. NMR velocity imaging 55

6. Pulse sequences – further developments 61

6.1. Improvements of DDCOSY 61
6.1.1. Shortening of DDCOSY to sDDCOSY 61
6.1.2. sDDCOSY with cross term suppression 65
6.2. 13-interval STEMSI for flow in natural porous media 66

7. Techniques of NMR data evaluation 69

7.1. Methods currently known 69
7.1.1. DDCOSY: Inverse Laplace transformation 69
7.1.2. MRI and velocity imaging: Fourier transformation 70
7.1.3. DTI: Moore-Penrose pseudoinverse matrix for tensor determination 71
7.2. New approach of determining diffusion tensors 74
7.2.1. The concept of least squares fitting 74
7.2.2. Demonstration on model data 75
Moore-Penrose pseudoinverse 76
Levenberg-Marquardt least squares fit 77

8. Results and discussion **79**

8.1. Diffusion tensor imaging on plant roots 79

8.1.1. Experimental setup for high resolution MRI and DTI measurements 79

8.1.2. High resolution NMR imaging on plant roots 79

8.1.3. Diffusion tensor imaging on plant roots 84

8.2. One- and two-dimensional diffusion measurements in natural sand . . 96

8.2.1. Experimental setup for 1D and 2D diffusion measurements . . 96

8.2.2. The influence of internal field gradients on the 1D diffusion determination 96

8.2.3. 2D investigations of diffusion behavior in natural sand 100

8.3. Velocity imaging in natural sand 103

8.3.1. Experimental setup for flow investigations on natural sand . . 103

8.3.2. Velocity mapping on flow in natural sand 105

9. Conclusion and outlook **119**

Bibliography **121**

List of Figures **129**

A. Abbreviations and symbols **131**

B. Acknowledgments **139**

C. Curriculum Vitae **141**

D. Publications **143**

1. Introduction

The understanding of water motion in soils and plant roots is of high importance for securing nutrition by plants in the context of climate change. Since roots are the "hidden half" of the plant [WEK91], in most experimental investigations the acquisition of information about processes in the soil-root-system took place either invasively or in very restricted geometries such as two-dimensional (2D) rhizotrones [Gre06].

In the last decade, nuclear magnetic resonance (NMR) and magnetic resonance imaging (MRI) received significant attention as methods for the non-invasive investigation of plants. NMR and MRI were applied to investigate three-dimensional (3D) structures in above-ground parts of plants [KPS04, MOP07] and to elucidate fluid motion. Different velocity scales from macroscopic flow to molecular self-diffusion were measured using flow imaging, diffusion, and $\boldsymbol{q}$-space methods [KKT98, Koe01, PRZ01, RZH99, SDJ00-1, SDJ00-2, SHJ02, SVW01, WRW00]. However, MRI mostly concentrated on aboveground parts of plants, neglecting the root system and its interaction with the surrounding soil matrix. Only recently it was possible to observe root system development and water uptake indirectly and non-invasively [BKC90, JRM03, NBN02, POP07, POP08] using MRI.

However, the theoretical understanding of root water uptake requires the integration of both experimental information and theoretical concepts [DPG06, GDP06, JTV08]. If the root system should serve as basis for numerical simulation of root water uptake by fully coupled soil-root models, an unambiguous representation of the root system in 3D is required. Technically, the 3D visualization of the root system architecture in natural soil by MRI is difficult. In the course of a single root strand gaps may occur, which originate from image distortions due to susceptibility effects; or at very common crossings of two roots it is ambiguous which root is continuing in which direction [POP08].

Therefore, a method is required that helps to reconstruct the course of root strands including additional information beyond the simple representation of the root sys-

tem based on spin density contrast, as it is delivered by conventional imaging. Such a method could be the spatially resolved measurement of diffusion or flow-induced dispersion processes, which also allows the measurement of flux processes in porous media such as the soil surrounding roots [POP08]. Here, diffusion tensor imaging (DTI) additionally allows identifying both direction and magnitude of water diffusion for every pixel within an image.

While diffusion as an NMR imaging contrast providing process was introduced in the mid-eighties [MHF85] and rapidly gained success in the investigation of stroke in brain tissue [MCM90], the anisotropy of diffusion came to the focus of diffusion MRI in the late eighties [CBP90]. However, only with the rigorous formulation of the diffusion tensor formalism of Basser et al. [BML94] the entire 3D process of diffusion was adequately described. A recent review on diffusion tensor imaging mathematics is presented in [Kin06-1, Kin06-2, Kin06-3]. So far, there are only very few examples of DTI applied to investigate plants and soil [BLE01], and none of the investigation of plant roots.

Since the inner structure of roots is not homogeneous, spatially different diffusion behavior is expected within the roots. Since the vascular bundles transport water in the xylem system alongside the roots, higher diffusion in the direction of the bundles than perpendicular to that direction is expected. In contrast, the surrounding cells in the cortex are more spherical and should exhibit no favored diffusion direction. The advantage of DTI compared to one-dimensional diffusion investigations is the possibility to quantify with DTI diffusion in any direction of the laboratory coordinate system.

A foreseeable difficulty in applying DTI on naturally grown roots are the very small root structures (mm to sub-mm diameter for maize plants). This requires small pixels which in turn result in low signal to noise ratios (SNR) of the diffusion weighted images.

Commonly used tensor calculations use the DTI signal obtained in multiple measurement directions and b-weightings [BML94]. The logarithms of these signals form a system of linear equations, which is simply solved without any additional constraints. For a diagonalized tensor of low SNR this leads to an overestimation of the principal eigenvalue and an underestimation of the smallest eigenvalue in the benign case and to negative eigenvalues (non-positive definite diffusion tensors) in the more severe cases. Furthermore in the presence of noise, the formulation of diffusion as a system of linear equations may not hold anymore, requiring a non-linear

fitting approach to solve it.

Since root water uptake does not only affect the plant roots but also the surrounding soil, water motion inside the soil structure have to be understood.

In the past, transport processes in soils were investigated with black-box methods combined with model calculations to characterize the internal structure of porous media. Invasive probes such as time domain reflectometry (TDR) [JV03] or in situ extraction of the liquid phase [WSD07] yield information about empirical parameters such as water content and solute composition at few defined sites inside the sample. For determining possible microscopic or macroscopic anisotropy of the soil, diffusion measurements give information about any restrictions to water motion [CGR03]. Since natural porous media may be quite heterogeneous, for monitoring water transport within the porous medium at least a spatial resolution in the range of the mean pore size is necessary.

Although MRI offers direct observation of fluxes by flow imaging techniques [Cal91], this method was used so far for investigations of flow rates ranging from 1 m/s [GC06, HMG01] down to several mm/s [SDJ00-1]. Slower flow rates and water fluxes, which are more typical for soils, were only monitored in glass bead packagings or indirectly with tracer substances [HPG02, PDW09, SC96, VAD97].

Measuring local velocities in porous media combining flow-encoding with imaging techniques is subject of many publications such as [HWV07, MGW99, RZH99]. However, none of these publications consider signal artifacts resulting from influences of internal magnetic field gradients induced by susceptibility effects. To avoid this impact, in the past systems providing long relaxation times have been selected for observing moving fluids [ALS05, CW99, GMP69, WF96]. However, the influences of internal magnetic field gradients on flow measurements in porous media were recently taken into account by Li et al. [LCM09], where water flow through a carbonate limestone reservoir core plug was monitored. Flow-encoding in Li et al. [LCM09] was obtained by reducing influences of internal magnetic field gradients according to Cotts et al. [CHS89], combined with the SPRITE pulse sequence (single-point ramped imaging with T_1 enhancement). However, for the purpose of investigating water flow close to plant roots, due to root water uptake the spatial resolution provided with SPRITE is not sufficient. Homan et al. [HVV10] also investigated the influence of internal magnetic field gradients on velocity mapping using pulsed magnetic field gradients combined with stimulated echo and turbo spin echo at different observation times. However, the influence of internal magnetic field

gradients on the signal intensity was not reduced as introduced by Li et al. [LCM09]. The flow investigations in Homan et al. [HVV10] were done on different types of model samples with grain sizes around 3.5 mm and only one velocity was applied to the samples. This sample size is one order of magnitude away from natural porous media having mean grain sizes around 0.35 mm. Therefore, the transfer of results from flow in model samples to natural porous media has to be handled carefully since wall effects cannot be neglected.

Aim of this work

The aim of this thesis is to understand water motion both in plant roots as well as in natural soil using different types of NMR and MRI techniques. Figure 1.1 shows a general overview of the investigations done in this context.

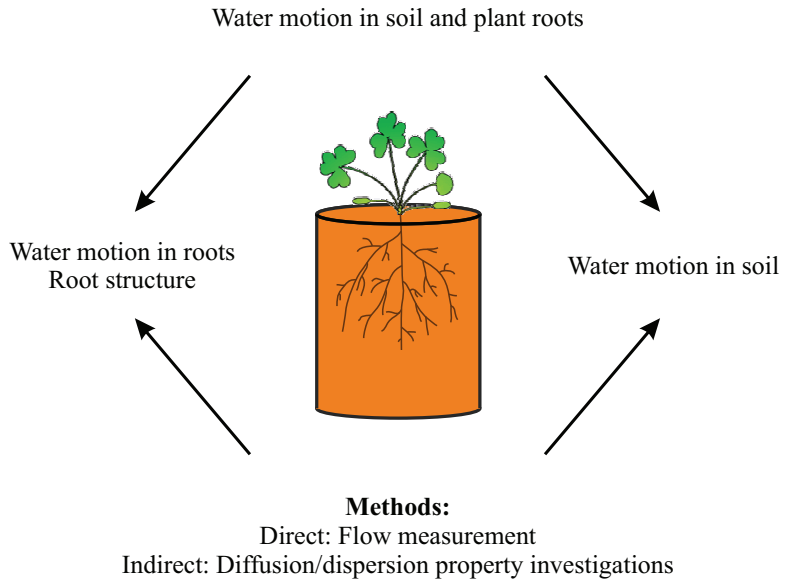

Figure 1.1: *Overview of investigations presented in this thesis for understanding root water uptake.*

Within this thesis the ability of DTI to reconstruct a single plant root from an entire plant root skeleton by visualizing diffusion directions is explored. Since the common method to determine the diffusion tensors is inaccurate due to the low signal

to noise ratio of the measurements, an improved approach has to be developed.

A two-dimensional diffusion method can be used for determining the grade of isotropy of the soil. Since natural soil shows both a short T_2 relaxation time and influences from internal magnetic field gradients, the common pulse sequence for determining diffusion correlations (diffusion diffusion correlation spectroscopy pulse sequence, DDCOSY) has to be modified in two steps. First, the duration of the pulse sequence itself is reduced by half. Second, the pulse sequence is further modified to reduce influences of internal magnetic field gradients. With this modifications it should be possible to determine the correct diffusion coefficients and to state that the investigated sample is microscopically and macroscopically isotropic.

While DTI is based on the indirect detection of water motion, water motion in soil can be investigated directly by velocity imaging. Due to the significant influence of internal magnetic field gradients to the NMR signal again the common pulse sequence for flow imaging has to be modified. As the modified DDCOSY pulse sequence, this modified pulse sequence can reduce the influence of internal magnetic field gradients. In this work, it will be applied on the mapping of local flow velocities. The detection limit of velocity imaging will be determined as well as the reliability of the flow velocity determination.

This work is structured into nine major chapters, whereby the first chapter gives an introduction to the research field of this thesis. In the second chapter the basic experimental equipment used for the measurements discussed later on is presented. Chapter 3 explains diffusion in natural porous media and shows the relation between diffusion and the mean displacement of molecules. This chapter also describes the difference between isotropic and anisotropic diffusion. In Chapter 4.1 the basics of nuclear magnetic resonance are explained, while Chapter 4.2 describes the principle of magnetic resonance imaging. Currently known NMR pulse sequences relevant for this thesis are presented in Chapter 5 together with a theoretical consideration of the expected recordable NMR signal. Thereby, the concept of pulsed and constant magnetic field gradients for detecting molecular motion is explained first on one-dimensional pulse sequences. Afterwards, these concepts are extended to two-dimensional and to imaging pulse sequences. In Chapter 6 the NMR pulse sequences developed for the investigations in this thesis are presented, while Chapter 7 deals with techniques for the evaluation of the NMR data. This chapter also contains a new approach for DTI data processing. Results from applying the pulse sequences

on different natural porous media are discussed in Chapter 8. Besides anatomical investigations of a maize root, in Chapter 8.1 the results of DTI on plant roots including a 3D tensor reconstruction of a single maize root are presented. The results of the shortened correlation pulse sequence for spectroscopic investigations of diffusion behavior is demonstrated on measuring water saturated natural sand in comparison to one-dimensional (1D) investigations. This is discussed in Chapter 8.2, taken into account the reduction of internal magnetic field gradients. Chapter 8.3 presents flow investigations through natural sand at different applied flow velocities together with a new combined pulse sequence reducing influences of internal magnetic field gradients. A lower limit of detectable velocity was found at the range of expectable water velocities in natural soil. Finally, Chapter 9 summarizes the results obtained in this thesis and gives an outlook to further investigations.

2. Equipment and materials

In this chapter the experimental equipment used in the measurements presented in this thesis is introduced. Thereby, this chapter deals only with the general instrumentation and samples. For each actual experiment, the individual setups are described later on in Chapters 8.1.1, 8.2.1, and 8.3.1.

2.1. NMR scanners

The nuclear magnetic resonance (NMR) experiments were performed on two high field scanners with magnetic fields of 7 T and 9.4 T.

2.1.1. 7 T scanner for root imaging and DTI

All investigations on plant roots such as high resolution imaging and diffusion tensor imaging measurements were performed using a 7 T vertical wide bore magnet system (Oxford Instruments, UK) operated by a Varian console (VnmrJ software; Varian, USA) in the Forschungszentrum Jülich, Germany. The left picture of Figure 2.1 shows the magnet system set up in the GreenNMRHouse in Jülich.

A Bruker micro imaging gradient system (maximal gradient strength 0.3 T m^{-1}; Bruker, Germany) and a birdcage resonator (38 mm internal diameter with a sensitive height of 50 mm; Bruker, Germany) were used for all NMR imaging investigations on this system.

2.1.2. 9.4 T scanner for diffusion investigations and velocity imaging on natural sand

One- and two-dimensional diffusion experiments as well as velocity imaging on natural sand were performed on a wide bore Bruker AVANCE 400 9.4 T scanner with

Figure 2.1: *Magnet systems used for the measurements presented in this thesis. The picture of the left hand side shows the* 7 T *system at the Forschungszentrum Jülich, Germany. On the right hand side is presented a picture of the* 9.4 T *system at the Victoria University of Wellington, New Zealand.*

an 89 mm vertical bore (Bruker, Germany) at the Victoria University of Wellington, New Zealand (Figure 2.1, right).

For both diffusion measurements and velocity mapping a Bruker micro imaging gradient system (Bruker, Germany) was used, having a maximum gradient strength of 1.45 T m^{-1} and a birdcage resonator with 15 mm internal diameter and a sensitive height of 20 mm.

2.2. Further experimental equipment

Beside the NMR scanners other instruments were needed to run the experiments. First, an optical microscope was used to identify the root anatomy; second, a peristaltic pump was used to apply a constant water flux to a sand column for flow investigations.

2.2.1. Optical microscopy of plant roots

Optical microscopy of thinly sliced, freshly cut maize roots was performed using the optical microscope Zeiss Axiophot 2 equipped with the digital camera Nikon D200. For better delineation of the different tissues, the thin slices were dyed with astra blue (marking cellulose walls) and safranin red (marking lignified cell walls). With this dying technique it is possible to distinguish the longitudinal extended lignified vascular bundles from the remaining spheroidal root tissue.

2.2.2. Peristaltic pump for induced water flow through natural sand

Flow through a column filled with natural sand was induced by the peristaltic pump Minipuls 3 (Gilson, USA). Tubes with an internal diameter of 3.16 mm were used, which leads to a maximal flow rate of $J_{\max} = 29\,\mathrm{mL\,min^{-1}}$ at the highest pump rate of $n_{\max} = 48\,\mathrm{rpm}$ [Gil07].

2.3. Samples used for NMR experiments

In different types of NMR experiments diffusion and flow properties of water in natural porous media were investigated. As samples served maize plants and natural sand.

2.3.1. Growing conditions of the maize plant

The fast formation of thick roots (typical diameter between 0.3 mm and 1.0 mm) qualifies maize plants best for the high resolution magnetic resonance imaging (MRI) experiments conducted here. With the given image resolution the roots extend over several pixels. Therefore, it was concluded that this species is favorable for diffusion tensor imaging (DTI) investigations.

A maize plant (*Zea mais 'Helix'*) was grown in a transparent Perspex® tube (outer diameter: 37 mm, length: 150 mm) on natural sand, covered with a 2 cm layer of coarse construction sand for the seedling. The bottom of the tube consisted of a porous glass plate for drainage. A photograph of the maize plant growing in the Perspex® tube is shown in Figure 2.2.

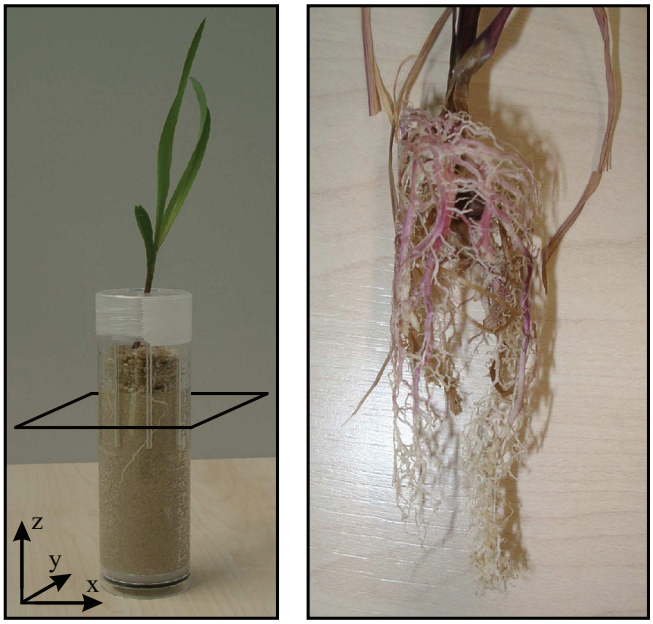

Figure 2.2: *Maize plant in Perspex® tube, grown on natural sand with a layer of* 2 cm *of coarse construction sand for the seedling. Optical microscopic slices and MR images (Chapter 8.1) were taken from the upper part of the root system where roots branch off from the spear. Left: The plant was seeded in the upper layer of coarse sand, wherefrom roots were growing into the natural sand. The black frame indicates the position and orientation of the slice taken into account for anatomical high resolution MRI and DTI measurements. The coordinate system denotes the laboratory coordinate system. Right: Maize plant roots excavated after all NMR measurements were finished.*

In the image a black frame indicates representatively the position and orientation of the slices taken into account for anatomical high resolution MRI and DTI measurements. The coordinate system denotes the laboratory coordinate system and orientation of the plant inside the NMR scanner.

The plant was grown in the temperature and humidity controlled GreenNMR-House in the Forschungszentrum Jülich, Germany, where also the NMR equipment is set up. Ambient temperature was stable at 18 °C during day and night. Watering was only performed via the porous plate from the bottom. Therefore, the plant tube stood upright in a water bath that reached the height of the sand inside the tube. Thus, it can be assumed that the sand was completely water saturated. About

two months after seeding the roots were thick enough (diameter up to 1.0 mm) for anatomical high resolution MRI and DTI measurements. Since the roots were strongest close to the seed, this region was selected for the DTI measurements. The right hand side of Figure 2.2 presents the excavated roots of the maize plants after all NMR measurements were finished.

As a reference probe a capillary filled with an aqueous solution of 5 mmol L^{-1} $NiCl_2$ was included in all NMR measurements undertaken on the maize plant.

2.3.2. Properties of the natural sand used for flow investigations

For flow imaging as well as for one- and two-dimensional diffusion investigations a polyvinyl chloride column with an inner diameter of $d_i = 13.5$ mm and a length of 95 mm was used. This column was filled with natural sand (FH 31, Quarzwerke Frechen GmbH, Frechen, Germany). The sand consists of 99.7 % SiO_2, 0.1 % Al_2O_3 and 0.04 % Fe_2O_3 and is characterized by a mean grain size of about 0.35 mm and a specific surface of 71 $cm^2\,g^{-1}$ [QuF09]. The water content of the sand column was $\theta = (0.35 \pm 0.01)\,cm^3\,cm^{-3}$.

3. Diffusion in natural porous media

One major objective of this thesis is to investigate diffusion behavior in natural porous media in order to determine pathways of water motion. Therefore, in the following the theory of diffusion is presented, and the mathematical description of diffusion via a tensor is introduced.

Diffusion is caused by a concentration gradient $\nabla c(\boldsymbol{r}, t)$ of molecules inside a system. Diffusion reduces the concentration gradient until the molecules are distributed according to the thermodynamic equilibrium. The diffusion process is expressed as a flux $\boldsymbol{j}(\boldsymbol{r}, t)$ of molecules in a volume through a section. This relation was found 1855 by Fick [Cra75] and is called Fick's first law,

$$\boldsymbol{j}(\boldsymbol{r}, t) = -D\nabla c(\boldsymbol{r}, t). \tag{3.1}$$

The proportionality constant is named the diffusion coefficient D. c denotes the molecule concentration. The nabla operator ∇ is defined as

$$\nabla = \frac{\partial}{\partial x}\,\boldsymbol{e}_x + \frac{\partial}{\partial y}\,\boldsymbol{e}_y + \frac{\partial}{\partial z}\,\boldsymbol{e}_z \tag{3.2}$$

with the unit vectors $\boldsymbol{e}_x$, $\boldsymbol{e}_y$ and $\boldsymbol{e}_z$ of a Cartesian coordinate system.

If the number of molecules is conserved, the time dependent change of the concentration is associated with a change in flux and the continuity theorem applies,

$$\nabla \boldsymbol{j}(\boldsymbol{r}, t) = -\frac{\partial c(\boldsymbol{r}, t)}{\partial t}. \tag{3.3}$$

The combination of Eq. (3.1) and Eq. (3.3) leads to Fick's second law,

$$\frac{\partial c(\boldsymbol{r}, t)}{\partial t} = \nabla(D\nabla c(\boldsymbol{r}, t)). \tag{3.4}$$

If the diffusion coefficient is independent on the spatial coordinates, Eq. (3.4) can

be simplified to:

$$\frac{\partial c(\boldsymbol{r},t)}{\partial t} = D\nabla^2 c(\boldsymbol{r},t). \tag{3.5}$$

Diffusion becomes self-diffusion when the concentration gradient disappears, $\nabla c \to 0$. In this case the thermodynamic equilibrium is reached and no macroscopic transport of molecules is observed. Since this work is based on water diffusion without any concentration gradient, the presented experiments always observe the self-diffusion of water.

If the boundary conditions are simple enough [Cra75], Eq. (3.5) can be easily solved. One premise is that the region is extended in order to avoid boundary effects. A second premise is that the system is sufficiently homogeneous. Starting with a point source described with the Dirac delta function $c(\boldsymbol{r},0) = \delta(\boldsymbol{r}-\boldsymbol{r}_0)$ as initial condition, the following Gaussian distribution is found as a solution of the partial differential Eq. (3.5):

$$P(\boldsymbol{r},\boldsymbol{r}_0,t) \equiv c(\boldsymbol{r},t) = \frac{1}{\sqrt{(4\pi D t)^3}} \exp\left\{-\frac{(\boldsymbol{r}-\boldsymbol{r}_0)^2}{4Dt}\right\}. \tag{3.6}$$

$P(\boldsymbol{r},\boldsymbol{r}_0,t)$ is the so called propagator of the diffusion process [KH83]. The propagator describes the probability density for finding molecules at the local position $\boldsymbol{r}$ at the time t, if the molecules were located at $\boldsymbol{r}_0$ at $t = 0$. The standard deviation $\sigma = \sqrt{2Dt}$ describes the spreading of the molecules with time.

Averaging over all molecules using the propagator of Eq. (3.6) results in the so called Einstein equation,

$$\left\langle (\boldsymbol{r}-\boldsymbol{r}_0)^2 \right\rangle = 6D\Delta. \tag{3.7}$$

This relationship combines the mean squared displacement $\langle(\boldsymbol{r}-\boldsymbol{r}_0)^2\rangle$ and the observation time $t = \Delta$. From Eq. (3.7) the mean displacement $\boldsymbol{R}$ of molecules can be extracted,

$$\boldsymbol{R} = \sqrt{\langle(\boldsymbol{r}-\boldsymbol{r}_0)^2\rangle} = \sqrt{6D\Delta}. \tag{3.8}$$

3.1. Restricted self-diffusion

So far the diffusion coefficient was considered to be independent of the observation time Δ and the distribution of the molecules is assumed to be Gaussian at any time. This assumption is only valid, if no obstacle interferes with the freely moving molecules. Whether an obstacle interferes depends on the probability that a molecule meets the obstacle in the time Δ; the longer Δ the more likely a collision will take place. Such collisions are the reason that in reality the distribution of the molecules deviates from a Gaussian and the diffusion coefficient is not constant for small times. For sufficiently long observation times Δ all molecules will collide with the obstacles. In this case the diffusion coefficient approaches the so called long time limit.

3.2. Anisotropic diffusion

In natural or complex systems, very often the diffusion is observed to be anisotropic. For example in a tube with a diameter smaller than $\boldsymbol{R}$ but much longer than $\boldsymbol{R}$, diffusion will be restricted perpendicular to the tube direction. However, diffusion parallel to the tube will not be restricted. Therefore, the diffusion behavior is in this case no longer isotropic, i. e. independent of spatial direction, and cannot be described with a scalar D. Instead, diffusion is expressed as the Cartesian diffusion tensor $\mathbf{D}$,

$$\mathbf{D} = \begin{pmatrix} D_{xx} & D_{xy} & D_{xz} \\ D_{yx} & D_{yy} & D_{yz} \\ D_{zx} & D_{zy} & D_{zz} \end{pmatrix}, \tag{3.9}$$

whereby the indices denote the directions in the Cartesian coordinate system. Since the vascular bundles of roots are shaped such as the described tube, anisotropic diffusion is expected. The diffusion tensor is mathematically positive definite and with that symmetric, therefore the three pairs of corresponding off-diagonal elements are equal, $D_{ij} = D_{ji}$. With the tensor definition in Eq. (3.9) the Fick's second law becomes

$$\frac{\partial c(\boldsymbol{r}, t)}{\partial t} = \nabla(\mathbf{D}\nabla c(\boldsymbol{r}, t)). \tag{3.10}$$

The off-diagonal elements of the diffusion tensor vanish, if the principal axes system of the diffusion tensor coincides with the Cartesian coordinate system. In this case only diffusion coefficients on the diagonal of the tensor remain. Together with the basis vectors of the tensor (here the unity vectors of the laboratory coordinate system in x, y, and z direction), the tensor elements describe the actual diffusion behavior of the sample. However, in the case of plant roots growing in different spatial directions, normally the basis of the tensors do not coincide with the laboratory coordinate system. Therefore, in Chapter 7.1.3 the diagonalization of diffusion tensors is described, allowing the formulation of diffusion in the sample coordinate system.

3.3. Flow in porous media

For considering flow in porous media, isotropic diffusion is assumed, but the diffusion of molecules is superimposed by a dispersive effect from the tortuous flow. Thus, the effective dispersion coefficient D_{eff} of water flowing through the porous medium with velocity $\boldsymbol{v}$ is increased. Compared to the self-diffusion coefficient D of undisturbed water D_{eff} becomes due to inhomogeneous flow paths of water molecules [HPG02, Rot07]:

$$D_{\text{eff}} = D + \Lambda|\boldsymbol{v}|. \tag{3.11}$$

In the empirical description in Eq. (3.11), Λ denotes the dispersivity parameter of the porous medium. The second term of Eq. (3.11), $\Lambda|\boldsymbol{v}|$, is often called "mechanical dispersion". Similar to self-diffusion, the effective dispersion has to be described with a tensor $\mathbf{D}_{\text{eff}}$ according to Eq. (3.9).

4. Theory of NMR and MRI

The measurements and results presented in this thesis are based on the theoretical concept of NMR. To understand the underlying theory of the experiments, the basics of NMR are introduced in the following. Since the main focus in this work is on NMR imaging, the second part of this chapter explains the principal concept of MRI. For a more comprehensive discussion of these and many more experimental NMR research methods, the references Callaghan [Cal91] and Blümich [Blu00] are very suitable sources.

4.1. Fundamentals of nuclear magnetic resonance

In this chapter the basic theoretical aspects of NMR are presented, covering relaxation times as well as the introduction of magnetic field gradients. All considerations are based on the vector model of classical mechanics.

4.1.1. Naming convention

First, magnetic fields, flow, and diffusion are directed quantities. Therefore, a coordinate system is required to describe equations and measurements. Throughout this work, a Cartesian coordinate system (x, y, z) is used where the z direction points upwards in the laboratory. In addition, the static external magnetic field first discussed in Chapter 4.1.2 and used in all measurements points always in z direction. Furthermore, also externally applied pulsed magnetic field gradients (PFGs) are aligned along this coordinate system.

Second, NMR is based on magnetic fields. Electric fields also involved in electromagnetic signal propagation are not regarded here. Therefore, the term "magnetic" is omitted in the discussion of fields, pulses, and gradients to improve readability.

4.1.2. Nuclear spins in the static magnetic field

Many atomic nuclei have a non-vanishing nuclear spin $\boldsymbol{I}$. The spin is a particular property of a quantum mechanical particle and can be described equivalent to the angular momentum in classical mechanics. Conventionally, the coordinate system is chosen such that its z component coincides with the direction of the polarizing field $\boldsymbol{B_0}$. In the following, the z direction is also called longitudinal and x and y directions are called transversal directions.

Since every atomic nucleus carries a charge, the spin is associated with a magnetic moment $\boldsymbol{\mu} = \gamma\hbar\boldsymbol{I}$. Here, $\hbar = h/2\pi$, where $h = 6.636\times10^{-34}\,\mathrm{J\,s}$ is Planck's constant and γ is the gyromagnetic ratio, which is characteristic to every nucleus. This work is focused on the nuclei of hydrogen atoms, i. e. protons (p), with a gyromagnetic ratio of $\gamma_\mathrm{p} = 2.675\times10^{8}\,\mathrm{s^{-1}\,T^{-1}}$ and $|\boldsymbol{I}| = 1/2$. In the following, all element specific constants such as γ_p refer to hydrogen and the index "p" is omitted.

In a polarizing magnetic field $\boldsymbol{B_0} = (0, 0, B_0)^\mathrm{T}$ a spin $\boldsymbol{I}$ may have any of several discrete relative orientations to the magnetic field. Each orientation is associated with the characteristic energy

$$E_m = \hbar\gamma m B_0. \tag{4.1}$$

Hereby, the magnetic quantum number m defines the number of energy levels. m can take values in the range of $m \in \{-|\boldsymbol{I}|, -(|\boldsymbol{I}|-1), ..., (|\boldsymbol{I}|-1), |\boldsymbol{I}|\}$. Thus, in the case of protons two energy levels $m = -1/2$ and $m = +1/2$ exist. These energy levels are occupied according to Boltzmann statistics. Since the lower energy level contains slightly more spins than the upper energy level, a classical net magnetization results. The z component of the magnetization vector is described by Curie's law,

$$M_z = \frac{n\gamma^2\hbar^2 B_0}{4k_\mathrm{B}T}. \tag{4.2}$$

This equation depends on the temperature T, the spin density n, and Boltzmann's constant $k_\mathrm{B} = 1.381\times10^{-23}\,\mathrm{J\,K^{-1}}$. The macroscopic equilibrium magnetization $\boldsymbol{M} = (M_x, M_y, M_z)^\mathrm{T}$ of a sample is formed by the sum of projections of all magnetic moments of the individual spins in the sample onto the axis of the magnetic field.

The Bohr-Einstein relation associates a frequency to a transition between two energy levels,

$$\Delta E = \hbar\omega_0, \tag{4.3}$$

which is referred to as Larmor frequency ω_0,

$$\omega_0 = -\gamma B_0. \tag{4.4}$$

Speaking classically, the net magnetization rotates with the Larmor frequency ω_0 around the direction of the applied external magnetic field $\boldsymbol{B_0}$, in this case clockwise (indicated by "−") around the z direction of the laboratory coordinate system.

4.1.3. Nuclear spins in a radio frequency alternating field

The static field $\boldsymbol{B_0}$ only orients the spins without enabling the measurement of the magnetization, since the voltage induced by the alternating magnetization is too low to be detected. Instead, it is necessary to excite spins from the lower energy level into the higher level. Technically, in addition to the static field $\boldsymbol{B_0}$, an rf alternating field $\boldsymbol{B_1}$ is applied perpendicular to $\boldsymbol{B_0}$. The frequency of $\boldsymbol{B_1}$ is the Larmor frequency $\omega_0 = \gamma B_0$. This linear polarized rf field can be decomposed into two circular polarized fields with the amplitude B_1, rotating clockwise and counterclockwise. One circular field rotates with ω_0 in the counter direction of the magnetization. This field is with a difference of $\Delta\omega = 2\omega_0$ off-resonant. The other circular field then rotates in resonance with the magnetization vector. This field impacts on the net magnetization such as an additional stationary magnetic field. As a result, the net magnetization in the rotating frame precesses additionally with the frequency ω_1,

$$\omega_1 = \gamma|\boldsymbol{B_1}|, \tag{4.5}$$

around $\boldsymbol{B_1}$. If the $\boldsymbol{B_1}$ alternating field is only applied for a short period of time (in the range of several μs up to a few ms), it is called an rf pulse. The rf pulse allows transition between the two energy levels. This is a gradual process, thus the more spins flip, the stronger the total magnetization changes. The magnitude of $\boldsymbol{B_1}$ and the duration of the pulse define the flip angle of the magnetization. Thereby, a 90° pulse corresponds to a complete transfer of the longitudinal magnetization in

z direction into a transversal magnetization in the xy plane perpendicular to the static field $\boldsymbol{B_0}$. If $\omega = \omega_0$, the effective longitudinal field is zero. If $\omega \neq \omega_0$ (off-resonant behavior), the effective longitudinal field in the rotating frame is no longer zero but takes the value $B = B_0 - \omega/\gamma$. The first 90° pulse applied in an NMR experiment is often called "excitation pulse", since this pulse leads to magnetization that can be detected as an NMR signal.

Detecting a signal – the Bloch equations

The precessing transversal magnetization induces a voltage in a surrounding coil with frequency ω_0, which is the detectable NMR signal. Right after the excitation an exponential decay of the signal can be observed, which is commonly called free induction decay (FID). The decay results from the interaction between the proton spins themselves and is called T_2 relaxation. Another relaxation process influencing the magnetization is the longitudinal T_1 relaxation, which is based on energy transfer between spins and the surrounding molecules, called lattice.

The time dependence of the magnetization $\boldsymbol{M}$ in the static field $\boldsymbol{B_0}$ can be described with a set of vector differential equations, known as the Bloch equations [Blo46]:

$$\frac{\mathrm{d}M_x}{\mathrm{d}t} = \gamma M_y(B_0 - \omega/\gamma) - \frac{M_x}{T_2}, \tag{4.6a}$$

$$\frac{\mathrm{d}M_y}{\mathrm{d}t} = \gamma M_z B_1 - \gamma M_x(B_0 - \omega/\gamma) - \frac{M_y}{T_2}, \tag{4.6b}$$

$$\frac{\mathrm{d}M_z}{\mathrm{d}t} = \gamma M_y B_1 - \frac{(M_z - M_0)}{T_1}. \tag{4.6c}$$

The NMR signal measured by the rf receiver is [Blu00, Cal91]

$$S(t) = S_0 \exp\{\mathrm{i}\,\varphi\} \exp\{\mathrm{i}\,\Delta\omega t\}(1 - \exp\{-t/T_1\}) \exp\{-t/T_2\} \tag{4.7}$$

at the offset frequency $\Delta\omega = \omega_0 - \omega_\mathrm{r}$, where ω_r is the mixing frequency included for reference purposes in the experimental setup. φ is the absolute receiver phase and S_0 is the signal amplitude immediately following the excitation pulse, a number which is simply proportional to M_0.

In the following, the influence of the two relaxation effects on the magnetization and, with that, on the NMR signal are discussed separately.

Relaxation of the longitudinal magnetization: T_1 relaxation

In interactions with the surrounding, spins loose energy to the lattice. By this T_1 relaxation the spin system returns to thermodynamic equilibrium after an excitation, until finally $\boldsymbol{M_0} = (0, 0, M_0)$ is directed back along the longitudinal field $\boldsymbol{B_0}$. This process described with Eq. (4.6c) has the solution:

$$M_z(t) = M_0(1 - \exp\{-t/T_1\}). \tag{4.8}$$

Relaxation of the transversal magnetization: T_2 and T_2^* relaxation

Mainly two mechanisms are responsible for the signal decay resulting from T_2 relaxation. On the one hand, different spin ensembles have various Larmor frequencies due to several effects. First, $\boldsymbol{B_0}$ contains inhomogeneities. Furthermore, interfaces between different materials or different tissues cause susceptibility effects. These invoke additional inhomogeneities in the magnetic field by creating local magnetic field gradients. Third, embedded paramagnetic or even ferromagnetic particles also distort the local magnetic field. Due to the inhomogeneities, the rotation frequencies ω of the spins are distributed around ω_0. The magnetization dephases with time and thus also the signal decreases with the absolute value of the magnetization. The signal decay due to field inhomogeneities is approximated by an exponential decay with the time constant T_{inhom}.

The second mechanism is relaxation due to interactions only between the nuclear spins. In this so-called spin-spin relaxation the spins exchange energy via level transitions but do not loose energy to the lattice. Spin-spin relaxation is expressed by the time constant T_2. Due to the energy exchange the spins loose their phase coherence. Since the vector sum of the magnetization decreases, also this process results in a signal reduction.

Due to these two relaxation effects, the actual relaxation time has to be defined as T_2^* relaxation and can be expressed by the equation

$$\frac{1}{T_2^*} = \frac{1}{T_2} + \frac{1}{T_{\text{inhom}}}, \tag{4.9}$$

considering both pure relaxation (T_2) and static field inhomogeneities (T_{inhom}). Thereby, T_2^* relaxation is mostly dominated by the inhomogeneities of the sample. In the following, the transversal relaxation time is named T_2 instead of T_2^* to

improve readability.

In sum the effect of T_2 relaxation on the magnetization can be described with the differential equation

$$\frac{\mathrm{d}M_{x,y}}{\mathrm{d}t} = \frac{-M_{x,y}}{T_2} \tag{4.10}$$

with solution

$$M_{x,y}(t) = M_{x,y}(0)\exp\{-t/T_2\}. \tag{4.11}$$

Phase cycling

Since the phase of the NMR signal depends on the rf pulse phase, it becomes possible to distinguish the NMR signal from any background interference by rf phase alternation. For example, shifting the rf phase by 180° leads to signal inversion. Therefore, successive phase alternations in steps of 180° are applied. The inverted signal is subtracted from the not inverted signal. This leads to coherent superposition of the NMR signal while the background interference is nullified.

A complex Fourier transformation is applied to the data during the analysis process as shown in Chapter 7.1.2. If the amplitude of the signal recording channels do not match or the relative phases are not precisely 90° apart, the complex Fourier transformation results in refolding artifacts. By successively swapping the channels used to acquire the real and imaginary signals, equivalent to a 90° transmitter and receiver phase shift, the error of the recorded NMR signal is compensated to first order.

For the NMR measurements presented in this thesis, this phase cycling resulted in different numbers of scans, depending on the applied pulse sequence.

4.1.4. Nuclear spins in magnetic field gradients

In the presence of an external applied field gradient $\boldsymbol{G}$,

$$\boldsymbol{G} = (G_x, G_y, G_z)^{\mathrm{T}} = \left(\frac{\partial B_z}{\partial x}, \frac{\partial B_z}{\partial y}, \frac{\partial B_z}{\partial z}\right)^{\mathrm{T}}, \tag{4.12}$$

the magnetic field and such also the Larmor frequency become dependent on the position $\boldsymbol{r}$,

$$\omega(\boldsymbol{r}) = \gamma\left(B_0 + \boldsymbol{G}\cdot\boldsymbol{r}\right). \tag{4.13}$$

Gradient fields are typically much smaller than the polarizing field B_0.

Applied field gradients allow spatial resolution of the NMR signal as well as detection of spin motion in a sample. In the following imaging chapter the concepts of $\boldsymbol{k}$- and $\boldsymbol{q}$-space are introduced. These are essential for the imaging and water motion experiments in this work. Further on magnetic field gradients used for imaging are discussed. In Chapter 5 NMR pulse sequences using applied magnetic field gradients for diffusion and flow measurements are introduced.

4.2. Magnetic resonance imaging

The basis of NMR imaging are field gradients causing spins to precess with differing Larmor frequencies according to their location in the sample.

MRI was first proposed by Lauterbur [Lau73]. It started out as a tomographic imaging technique, which produces an image of the NMR signal in a thin slice through the sample of interest. MRI has since then advanced beyond a tomographic imaging technique to a volume imaging technique.

4.2.1. NMR signal from the $\boldsymbol{k}$-space and the $\boldsymbol{q}$-space

Magnetic field gradients allow to detect the position of molecules in a sample. Scanning the position from where the signal is obtained creates an image of the spin density $\rho(\boldsymbol{r})$ in the sample. To translate measured temporal NMR signal into an image, first the signal is mapped onto the reciprocal space vector $\boldsymbol{k}$ [MG73]. If the sample is affected by flow, additionally a reciprocal velocity vector $\boldsymbol{q}$ has to be considered. The respective spaces are called $\boldsymbol{k}$-space and $\boldsymbol{q}$-space [Blu00, Cal91]. After this transformation, the spatially resolved spin density $\rho(\boldsymbol{r})$ can be obtained by a Fourier transformation. This process is explained in detail in the following.

Spins at position $\boldsymbol{r}$ in the sample are considered, occupying a small volume element $\mathrm{d}\boldsymbol{r}$ with local spin density $\rho(\boldsymbol{r})$. There are $\rho(\boldsymbol{r})\,\mathrm{d}\boldsymbol{r}$ spins in this volume element. Following Eq. (4.7) and ignoring relaxation and a phase offset, the NMR signal

integrated over the entire sample volume V may be written as

$$\begin{aligned} S(\boldsymbol{G},t) &= \int\limits_V \mathrm{d}\boldsymbol{r}\rho(\boldsymbol{r}) \exp\Big\{ \mathrm{i} \int\limits_0^t \mathrm{d}t'\omega(t') \Big\} \\ &= \int\limits_V \mathrm{d}\boldsymbol{r}\rho(\boldsymbol{r}) \exp\Big\{ \mathrm{i}\,\gamma \int\limits_0^t \mathrm{d}t'[B_0(t') + \boldsymbol{G}(t')\boldsymbol{r}(t')] \Big\}. \end{aligned} \tag{4.14}$$

$\mathrm{d}\boldsymbol{r}$ represents the volume integration. By choosing the reference frequency $\omega_\mathrm{r} = \gamma B_0$ ("on-resonance"), the detected signal rotates with a frequency $\gamma\,\boldsymbol{G}\cdot\boldsymbol{r}$. Here, it is assumed that the observer rotates together with the magnetization with ω_0 around the direction of the static magnetic field. This is termed rotating coordinate frame (RCF). Thus, the term γB_0 in Eq. (4.14) may be neglected. Therefore, the integrated signal amplitude in the RCF can be written as

$$S(\boldsymbol{G},t) = \int\limits_V \mathrm{d}\boldsymbol{r}\rho(\boldsymbol{r}) \exp\Big\{ \mathrm{i}\,\gamma \int\limits_0^t \mathrm{d}t'\boldsymbol{G}(t')\boldsymbol{r}(t') \Big\}. \tag{4.15}$$

The time integral in the exponent resulting in a phase shift $\Phi(t)$ can be rewritten as

$$\Phi(t) = \gamma \int\limits_0^t \mathrm{d}t'\boldsymbol{G}(t')\,\boldsymbol{r}(t'). \tag{4.16}$$

A Taylor expansion of $\boldsymbol{r}$ as

$$\boldsymbol{r}(t) = \boldsymbol{r_0} + \boldsymbol{v_0}t + \dots\,, \tag{4.17}$$

where $\boldsymbol{v_0}$ denotes the velocity of the spins at $\boldsymbol{r}(t=0) = \boldsymbol{r_0}$. This leads to

$$\Phi(t) = \gamma\,\boldsymbol{r_0} \int\limits_0^t \mathrm{d}t'\boldsymbol{G}(t') + \gamma\,\boldsymbol{v_0} \int\limits_0^t \mathrm{d}t'\boldsymbol{G}(t')t' + \dots\ . \tag{4.18}$$

$\Phi(t)$ is part of the so called matrix of phase terms [Blu00]. The elements of this matrix are the moments of the gradient function

$$\boldsymbol{m}_k(t) = \int_0^t \mathrm{d}t' \boldsymbol{G}(t') t'^k. \tag{4.19}$$

The Fourier conjugates $\boldsymbol{k}$ and $\boldsymbol{r}$, as well as $\boldsymbol{q}$ and mean velocity $\boldsymbol{v}$ are straightforward defined as

$$\boldsymbol{k}(t) = \frac{\gamma}{2\pi}\boldsymbol{m}_0(t) = \frac{\gamma}{2\pi}\int_0^t \mathrm{d}t' \boldsymbol{G}(t'), \tag{4.20a}$$

$$\boldsymbol{q}(t) = \frac{\gamma}{2\pi}\boldsymbol{m}_1(t) = \frac{\gamma}{2\pi}\int_0^t \mathrm{d}t' \boldsymbol{G}(t') t'. \tag{4.20b}$$

Inserting the $\boldsymbol{k}$-vector (Eq. (4.20a)) in the NMR signal (Eq. (4.15)) results in the signal intensity in $\boldsymbol{k}$-space. The Fourier transformation of $S(\boldsymbol{k})$ results in the spin density at any position in the sample:

$$S(\boldsymbol{k}) = \int_V \mathrm{d}\boldsymbol{r} \rho(\boldsymbol{r}) \exp\{\mathrm{i}\, 2\pi \boldsymbol{k}\cdot\boldsymbol{r}\}, \tag{4.21a}$$

$$\rho(\boldsymbol{r}) = \int_{V^{-1}} \mathrm{d}\boldsymbol{k} S(\boldsymbol{k}) \exp\{-\mathrm{i}\, 2\pi \boldsymbol{k}\cdot\boldsymbol{r}\}. \tag{4.21b}$$

Equation (4.21) is the fundamental relationship for NMR imaging, since it gives information about the spin density at each position in the sample. Thereby, the resolution of an NMR image is reciprocally proportional to the difference between highest and lowest applied field gradient,

$$\mathrm{res} \propto \frac{1}{|\boldsymbol{G}_{\max} - \boldsymbol{G}_{\min}|} \propto \frac{1}{|\boldsymbol{k}_{\max} - \boldsymbol{k}_{\min}|}. \tag{4.22}$$

The entire spatial extent of the NMR image is expressed by the field of view (FOV). The FOV is reciprocally proportional to the difference between two successive PFGs, $\mathrm{FOV} \propto \frac{1}{|\Delta \boldsymbol{G}|} \propto \frac{1}{|\Delta \boldsymbol{k}|}$.

4.2.2. The slice selective gradient $\boldsymbol{G}_\mathrm{s}$ and multislicing

In many applications the observer is interested in a cross-sectional image of the sample. To create the image, a magnetic field gradient is applied during spin excitation with an rf pulse. This so called "slice selective" gradient $\boldsymbol{G}_\mathrm{s}$ encodes the Larmor frequency depending on the position. Assuming a slice selective gradient in z direction, $\boldsymbol{G}_\mathrm{s} = (0, 0, G_z)^\mathrm{T}$, the Larmor frequency becomes $\omega(z) = \gamma(B_0 + G_z \cdot z)$ according to Eq. (4.13). The linear relationship between frequency and position transforms the frequency spectrum $B_{1,z}(\omega)$ of the exciting pulse directly to the excitation profile $\alpha(z) = \gamma B_{1,z}(\omega(z))$ perpendicular to the selected slice. Thus, the envelope of the Fourier transformed pulse shape approximates the slice profile. Therefore, the bandwidth of the pulse, which is inversely proportional to its duration, defines the slice thickness. For exciting only a narrow frequency band, imaging pulse sequences apply "soft" rf pulses with durations of typically 1 ms. For exciting a large area of the sample with broad frequency bands, "hard" rf pulses with durations of typically $10 - 100\,\mu$s are applied.

The slice selective gradient applied during the rf pulse dephases the magnetization in z direction. To compensate for that, an inverse slice selective gradient pulse right after the first gradient is applied.

Typically, between two NMR experiments a time *TR* has to be waited to allow T_1 recovery. In multislicing experiments it is possible to usefully employ the waiting interval thus reducing total measurement time. In a cycle time sufficient for a first slice in the sequence to recover, adjacent or interleaved slices are sequentially imaged. This works since selective excitation ideally disturbs only one slice in the sample so that spins in adjacent slices will remain in thermal equilibrium. The unperturbed spins are available for immediate excitation following the signal acquisition from the first slice.

4.2.3. The read out gradient $\boldsymbol{G}_\mathrm{r}$ and the phase-encoding gradient $\boldsymbol{G}_\mathrm{p}$

When the NMR signal is acquired in the presence of a gradient, signal points lie along a single line in $\boldsymbol{k}$-space. In Fourier transformation based NMR imaging this line is oriented along one of the Cartesian axes. The associated gradient is known as "read out" gradient $\boldsymbol{G}_\mathrm{r}$. In the following the x coordinate is ascribed to this

direction, $\boldsymbol{G}_\mathrm{r} = (G_x, 0, 0)^\mathrm{T}$. The intercept of this line with the orthogonal axis can be changed by imposing the gradient in y direction for a fixed time before sampling begins. This gradient is named "phase-encoding" gradient $\boldsymbol{G}_\mathrm{p}$ with $\boldsymbol{G}_\mathrm{p} = (0, G_y, 0)^\mathrm{T}$ since it imparts a phase modulation to the NMR signal, dependent on the position of volume elements along the y direction.

The components k_x and k_y of the $\boldsymbol{k}$-vector are given by

$$k_x = \frac{\gamma}{2\pi} G_x t_x, \tag{4.23a}$$

$$k_y = \frac{\gamma}{2\pi} G_y t_y, \tag{4.23b}$$

according to Eq. (4.20a). Thereby, t_x and t_y denote different periods of time and involve evolutions under the influence of different gradients. During the phase-encoding time period ($k_x = 0$ and $k_y \neq 0$) the spins evolve along $+k_y$ with time. Subsequently, during the read out period ($k_x \neq 0$ and $k_y = 0$) the signal is mapped along $+k_x$ at an intercept of k_y set by the previous evolution. Commonly, the intercept is chosen using a fixed phase period and adjusting the magnitude of the phase gradient.

Following Eq. (4.21a) the signal is therefore

$$S(k_x, k_y) = \int_{-a/2}^{a/2} \mathrm{d}z \left[\int_{-\infty}^{\infty} \int_{-\infty}^{\infty} \mathrm{d}x\, \mathrm{d}y\, \rho(x, y, z) \exp\{\mathrm{i}\, 2\pi (k_x x + k_y y)\} \right], \tag{4.24}$$

where a is the slice thickness. The outer integral merely represents the process of integrating across the slice. For convenience, this contribution is neglected in the following. Thus, Eq. (4.24) simplifies to

$$S(k_x, k_y) = \int_{-\infty}^{\infty} \int_{-\infty}^{\infty} \mathrm{d}x\, \mathrm{d}y\, \rho(x, y) \exp\{\mathrm{i}\, 2\pi (k_x x + k_y y)\}, \tag{4.25}$$

where $\rho(x, y)$ is the volume density function integrated normal to the slice. $S(k_x, k_y)$ is the 2D Fourier transform of the spin area density function $\rho(x, y)$. Reconstructing $\rho(x, y)$ from $S(k_x, k_y)$ simply requires the calculation of the inverse Fourier transfor-

mation according to Eq. (4.21b),

$$\rho(x,y) = \int_{-\infty}^{\infty}\int_{-\infty}^{\infty} \mathrm{d}k_x\,\mathrm{d}k_y\, S(k_x,k_y)\exp\{-\mathrm{i}\,2\pi(k_x x + k_y y)\}. \tag{4.26}$$

Recording the signal $S(k_x, k_y)$ is the heart of NMR imaging based on Fourier transformation.

Sampling the $\boldsymbol{k}$-space along k_x with a fixed read gradient is repeated for increasing values of the k_y intercept until a full map of the $\boldsymbol{k}$-space is obtained.

5. Pulse sequences – methods currently known

In this chapter common NMR pulse sequences are introduced, forming the basis for the experiments presented in this thesis. First, one-dimensional pulse sequences show the principle of NMR measurements. Further on in this chapter the concept of two-dimensional correlation spectroscopy of diffusion and the NMR imaging principle with the possibility of diffusion and velocity mapping are presented.

5.1. 1D pulse sequences

This section describes basic NMR pulse sequences. It is discussed how NMR echoes are formed and in which ways pulsed field gradients are applied. For convenience, the effects of basic NMR pulse sequences are described using simple 1D pulse sequences as discussed in detail in Stallmach and Galvosas [SG07], and Zheng and Price [ZP07].

5.1.1. The spin echo

Inhomogeneous polarizing magnets cause a field spread of ΔB_0 across the sample. Consequently, the transverse magnetization dephases after applying an exciting 90° pulse. In fact, phase coherence of the transverse magnetization exists only for a time of order $(\gamma \Delta B_0)^{-1}$. This limits the time during which the magnetization can be manipulated or detected. Hahn found in 1950 [Hah50] that dephasing is principally reversible. A second 180° pulse after a time delay τ refocuses the spins at the total time 2τ as shown in Figure 5.1. The resulting phase coincidence is known as a spin echo with the phase of the 180° pulse determining the sign of the echo signal.

Due to T_2 relaxation the transverse magnetization at the echo time $t_e = 2\tau$ is

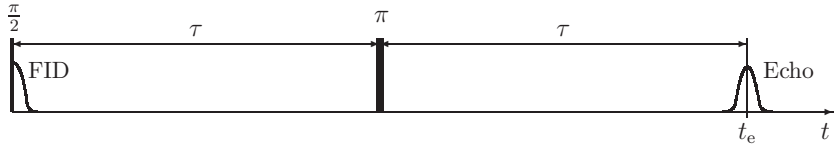

Figure 5.1: *Spin echo pulse sequence as suggested by Hahn [Hah50] to refocus the spins. At the time τ after the exciting 90° pulse a second, 180° pulse is applied. This results in a spin echo at the time 2τ.*

given by

$$M_{x,y}(2\tau) = M_{x,y}(0)\exp\{-2\tau/T_2\}, \tag{5.1}$$

according to Eq. (4.11).

5.1.2. NMR with pulsed field gradients for probing diffusion and flow

NMR experiments with pulsed field gradients (PFGs) are mainly based on spin echo pulse sequences. Stejskal and Tanner [ST65] inserted two pulsed field gradients with duration δ to the original spin echo pulse sequence, see Figure 5.2.

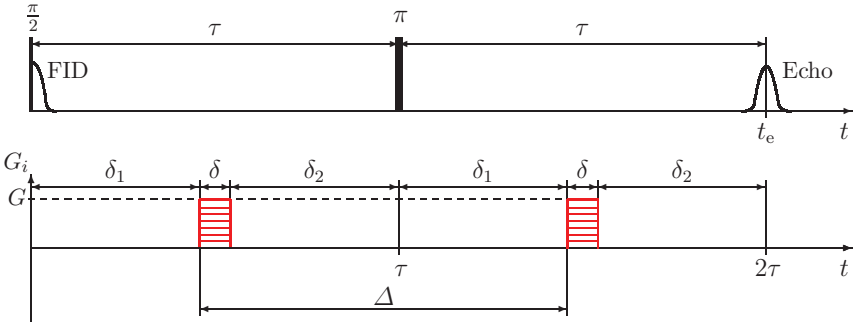

Figure 5.2: *Spin echo pulse sequence with applied pulsed field gradients $\boldsymbol{G}(t)$ (PFGs). The 180° pulse inverts the effect of the first gradient pulse, which is considered with the definition of effective pulsed field gradients $\boldsymbol{G}^*(t)$. The gradient direction G_i represents all three possible directions (x, y, and z direction) in the laboratory coordinate system for the application of PFGs.*

The first pulsed field gradient is applied between the exciting 90° pulse and the refocusing 180° pulse. According to Eq. (4.13), the PFG produces a linear spatial dependence of the Larmor frequency $\omega(\boldsymbol{r})$. The duration δ and the amplitude $|\boldsymbol{G}(t)|$ of the PFG influences the dephasing effect. Therefore, the spins are locally phase labeled. The second, identical PFG is placed between the refocusing 180° pulse and the spin echo. Both PFGs have the same temporal offset δ_1 from the preceding pulses. Since the 180° pulse inverts the effect of any PFG, the second pulsed field gradient rephases the spins. If spins move during the observation time Δ between the two PFGs, the rephasing stays incomplete. Thus, the signal intensity of the detected spin echo decreases. This signal attenuation indicates a displacement of molecules and also a change in the diffusion coefficient according to Eq. (3.7).

In a PFG NMR experiment the amplitude or pulse duration of the PFGs is stepwise increased, holding the observation time Δ constant. This creates a set of decreasing spin echo signal intensities. Fitting the data yields the mean squared displacement of the molecules during the time Δ and thus the mean velocity of the molecules or the diffusion coefficient.

Effective magnetic field gradients

Previously it was already mentioned that a 180° pulse inverts the effect of PFGs. The concept of effective magnetic field gradients [KL80] states that 180° pulses generally change the sign of all field gradients applied before [MP78]. Starting at the echo time t_e and moving backwards in time this holds for every applied 180° pulse. For the spin echo pulse sequence with two applied PFGs shown in Figure 5.2 this means

$$\int_0^{t_\mathrm{e}} \mathrm{d}t\, \boldsymbol{G}^*(t) = 0 \quad \Leftrightarrow \quad \boldsymbol{G}^*(t) = \begin{cases} -\boldsymbol{G}(t) & \text{for} \quad 0 \le t \le \tau, \\ \boldsymbol{G}(t) & \text{for} \quad \tau \le t \le t_\mathrm{e}. \end{cases} \tag{5.2}$$

$\boldsymbol{G}^*(t)$ is introduced as effective pulsed field gradient of $\boldsymbol{G}(t)$. $\boldsymbol{G}^*(t)$ depends on time, but not on the local position. If still an NMR signal should be detected at t_e, the phase shift caused by the first PFG has to be canceled. In case of the spin echo pulse sequence, cancellation is performed by the second effective PFG $\boldsymbol{G}^*(t)$.

With Eq. (5.2) this results in the condition

$$-\int_0^{\tau} \mathrm{d}t\boldsymbol{G}(t) + \int_{\tau}^{t_e} \mathrm{d}t\boldsymbol{G}(t) = 0. \tag{5.3}$$

The Bloch-Torrey equations

To infer mean squared displacements and molecular diffusion coefficients from PFG NMR experiments, the dependence of the detected signal on the PFGs must be known. Starting from Bloch's equations (Eq. (4.6)), Torrey [Tor56] added an additional term considering diffusive influences on the NMR signal according to Eq. (3.10), expressed by the diffusion tensor $\mathbf{D}$:

$$\frac{\partial \boldsymbol{M}(\boldsymbol{r},t)}{\partial t} = \gamma \boldsymbol{M} \times \boldsymbol{B} - \frac{M_x \boldsymbol{e}_x + M_y \boldsymbol{e}_y}{T_2} - \frac{M_z - M_0}{T_1}\boldsymbol{e}_z + \nabla \mathbf{D} \nabla \boldsymbol{M}. \tag{5.4}$$

$\boldsymbol{M}(\boldsymbol{r},t)$ depends on time and the local position. The macroscopic magnetization $\boldsymbol{M}(t)$ which is only time dependent is calculated by integrating $\boldsymbol{M}(\boldsymbol{r},t)$ over the entire sample volume.

In the following, isotropic diffusion is assumed. Then, the last term of the Bloch-Torry equation Eq. (5.4) can be simplified to

$$\nabla \mathbf{D} \nabla \boldsymbol{M} = D\nabla^2 \boldsymbol{M} \tag{5.5}$$

with the diffusion coefficient D. After the exciting 90° pulse at $t = 0$, the magnetization is only transverse, $M_z(\boldsymbol{r},0) = 0$. Since $\boldsymbol{B}(\boldsymbol{r},t) = (0,0,B_z(\boldsymbol{r},t))^{\mathrm{T}}$ the z component of the local magnetization $\boldsymbol{M}(\boldsymbol{r},t)$ decouples from the x and y direction. With the linear combination $\mathcal{M}(\boldsymbol{r},t) = M_x(\boldsymbol{r},t) + \mathrm{i}\, M_y(\boldsymbol{r},t)$ the transverse equations can be combined to [Tor56]

$$\frac{\partial \mathcal{M}(\boldsymbol{r},t)}{\partial t} = \left[\mathrm{i}\,\gamma B_z(\boldsymbol{r},t) - \frac{1}{T_2} + D\nabla^2\right] \mathcal{M}(\boldsymbol{r},t). \tag{5.6}$$

Solving this differential equation is done by a separation of variables:

$$\begin{aligned}\mathcal{M}(\boldsymbol{r},t) &= S(t)\exp\left\{-\frac{t}{T_2} - \mathrm{i}\,\gamma\int_0^t \mathrm{d}t' B_z(\boldsymbol{r},t')\right\} \\ &= S(t)\exp\left\{-\frac{t}{T_2} - \mathrm{i}\,\omega_0 t - \mathrm{i}\,\gamma\,\boldsymbol{r}\int_0^t \mathrm{d}t' \boldsymbol{G}^*(t'')\right\}, \end{aligned} \tag{5.7}$$

where $S(t)$ is the complex signal amplitude of the local transverse magnetization. The first term in the exponent describes the transverse T_2 relaxation. For better readability the effect of T_2 relaxation on the NMR signal is not considered in the following. Influences of field gradients on the NMR signal are discussed in the rotating frame, therefore the term $\omega_0 t$ does no longer appear. The last part of Eq. (5.7) describes the time depending phase of the local magnetization according to the Larmor condition $\omega(\boldsymbol{r},t) = -\gamma|\boldsymbol{B}(\boldsymbol{r},t)|$. Integrating over $\mathcal{M}(\boldsymbol{r},t)$ following Eq. (5.7) results in the macroscopic complex transverse magnetization $M_{xy}(t)$:

$$M_{xy}(t) = M_x(t) + \mathrm{i}\,M_y(t) = \int_V \mathrm{d}\boldsymbol{r}\,\mathcal{M}(\boldsymbol{r},t) \tag{5.8}$$

with the sample volume V. At $t = 0$ the local magnetization is $\mathcal{M}(\boldsymbol{r},0) = S(0)$. Here, the local magnetization is coherent at all positions with an absolute phase giving by $S(0)$. Thus, the initial magnetization is

$$M_{xy}(0) = S(0)V. \tag{5.9}$$

Inserting Eq. (5.7) in Eq. (5.6) and considering Eq. (4.13) results in an ordinary differential equation for $S(t)$,

$$\frac{\mathrm{d}S(t)}{\mathrm{d}t} = -S(t)D\left[\gamma\int_0^t \mathrm{d}t' \boldsymbol{G}^*(t')\right]^2, \tag{5.10}$$

with the solution

$$S(t) = S(0)\exp\left\{-D\gamma^2\int_0^t \mathrm{d}t'\left[\int_0^{t'} \mathrm{d}t'' \boldsymbol{G}^*(t'')\right]^2\right\}. \tag{5.11}$$

Note that t' and t'' are used as substitutes for the time integrals, since t is the upper integration limit. In both equations the definition of effective PFGs $\boldsymbol{G}^*(t)$ is used to consider the inverting effect of 180° pulses. For known PFGs the signal amplitude $S(t)$ can be directly calculated from Eq. (5.11).

The effective PFGs of the spin echo pulse sequence shown in Figure 5.2 are

$$\boldsymbol{G}^*(t) = \begin{cases} 0 & \text{for} \quad 0 \leq t \leq \delta_1, \\ -\boldsymbol{G}(t) & \text{for} \quad \delta_1 \leq t \leq \delta_1 + \delta, \\ 0 & \text{for} \quad \delta_1 + \delta \leq t \leq \tau + \delta_1, \\ \boldsymbol{G}(t) & \text{for} \quad \tau + \delta_1 \leq t \leq \tau + \delta_1 + \delta, \\ 0 & \text{for} \quad \tau + \delta_1 + \delta \leq t \leq t_\mathrm{e}. \end{cases} \tag{5.12}$$

Introducing these definitions, with Eq. (5.11) the signal amplitude of the spin echo pulse sequence at echo time t_e yields

$$S(t_\mathrm{e}) = S(0) \exp\left\{-D\gamma^2\delta^2\left(\Delta - \tfrac{1}{3}\delta\right)\boldsymbol{G}^2\right\}. \tag{5.13}$$

Therefore, Eq. (5.11) provides together with the pulse sequence specific definitions of the type defined in Eq. (5.12) a general method to determine diffusion coefficients with PFG NMR.

Coming back to Eq. (5.9), the initial magnetization has a constant, unlocalized phase. According to Eq. (5.7), for times $t > 0$ the local magnetization $m(\boldsymbol{r}, t)$ is both influenced by a constant Larmor frequency $\omega_0 = -\gamma B_0$ and by a Larmor frequency $\omega(\boldsymbol{r}, t) = -\gamma\, \boldsymbol{r}\boldsymbol{G}^*(\boldsymbol{t})$ dependent on position. Since PFGs impose an additional field $B_\mathrm{PFG}(\boldsymbol{r}, t)$ for a short time, the z component of the total field $B_z(\boldsymbol{r}, t)$ in the becomes also dependent on position:

$$B_z(\boldsymbol{r}, t) = B_0 + B_\mathrm{PFG}(\boldsymbol{r}, t). \tag{5.14}$$

Note that $B_0 = 0$ in the rotating frame. The additional field causes at any position $\boldsymbol{r} \neq \boldsymbol{r}_0$ a phase shift from the Larmor frequency $\omega_0 t$ that grows linearly with time. This translates into an increasing spiral torsion of the local magnetization vector $m(\boldsymbol{r}, t)$ along the gradient. Consequently, due to Eq. (5.8) the macroscopic magnetization M_{xy} disappears with time.

5.1.3. The influence of constant magnetic field gradients

As long as the amplitudes of constant magnetic field gradients $\boldsymbol{g}$ (CFGs) are small and $\boldsymbol{r}\boldsymbol{g} \ll B_0$ is fulfilled for all positions in the sample, CFGs (Figure 5.3) have the same influence on the signal $S(t_\mathrm{e})$ as PFGs.

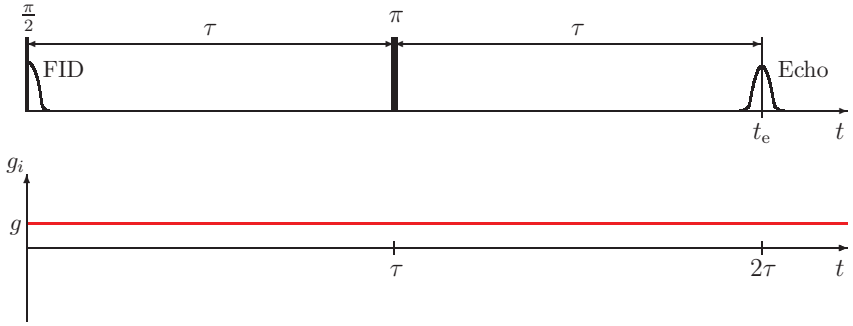

Figure 5.3: *Spin echo pulse sequence with a constant field gradient $\boldsymbol{g}$ (CFG). The 180° pulse inverts the effect of CFGs for $t \leq \tau$. g_i stands for any direction (x, y, and z) of the gradient in the laboratory coordinate system.*

The effect of a CFG $\boldsymbol{g}$ on the signal $S(t_\mathrm{e})$ can be determined and with the condition $\boldsymbol{G}^*(t) = \boldsymbol{g}^*(t)$ for Eq. (5.11), this effect leads to [CP54]

$$S(t_\mathrm{e}) = S(0)\exp\left\{-\tfrac{2}{3}D\gamma^2\tau^3\boldsymbol{g}^2\right\} \quad \text{with} \quad \boldsymbol{g}^*(t) = \begin{cases} -\boldsymbol{g} & \text{for} \quad t \leq \tau, \\ \boldsymbol{g} & \text{for} \quad t \geq \tau. \end{cases} \tag{5.15}$$

Due to the inverting effect of the 180° pulse, inhomogeneities in the static field $\boldsymbol{B}_0$ can be taken into account as long as the CFGs do not depend on position.

A significant issue with NMR experiments on natural porous media is the influence of so called internal field gradients in the sample. Internal field gradients result in sections with a different susceptibility χ than the bulk sample and can also be described as CFGs. In the presence of internal field gradients the local field $\boldsymbol{B}$ and with that also the gradient depend on $\boldsymbol{r}$. In the following, internal field gradients are defined as constant, if they do not change significantly along the diffusion from $\boldsymbol{r}_i(0)$ to $\boldsymbol{r}_i(\Delta)$ of spin i during the observation time Δ. This constraint does not exclude homogeneous changes of the internal field gradient over the entire sample volume.

The effective field gradient $\boldsymbol{G}^*(t)$ is replaced by the sum of effective CFGs $\boldsymbol{g}^*(t)$ and PFGs $\boldsymbol{G}^*(t)$,

$$\boldsymbol{G}^*(t) \quad \rightarrow \quad \boldsymbol{G}^*(t) + \boldsymbol{g}^*(t). \tag{5.16}$$

With that, Eq. (5.11) can be written as [GSK04]:

$$S(t) = S(0) \exp\left\{-D\gamma^2 \left[A_\mathrm{p}(t) + A_\mathrm{c}(t) + A_\mathrm{i}(t)\right]\right\} \quad \text{with} \tag{5.17}$$

$$A_\mathrm{p}(t) = \int_0^t \mathrm{d}t' \left[\int_0^{t'} \mathrm{d}t''\, \boldsymbol{G}^*(t'')\right]^2, \tag{5.17a}$$

$$A_\mathrm{c}(t) = 2\int_0^t \mathrm{d}t' \int_0^{t'} \mathrm{d}t''\, \boldsymbol{G}^*(t'') \int_0^{t'} \mathrm{d}t''\, \boldsymbol{g}^*(t''), \tag{5.17b}$$

$$A_\mathrm{i}(t) = \int_0^t \mathrm{d}t' \left[\int_0^{t'} \mathrm{d}t''\, \boldsymbol{g}^*(t'')\right]^2. \tag{5.17c}$$

$A_\mathrm{p}(t)$ and $A_\mathrm{i}(t)$ describe the quadratic fractions of the spin echo attenuation caused by the pulsed and internal field gradients, respectively. Since the sign of $\boldsymbol{g}^*(t)$ depends on the 180° pulses and with that on the specific pulse sequence, the integrals in Eq. (5.17b) and Eq. (5.17c) cannot be solved in general. This holds even for time independent $\boldsymbol{g}$. For a specific pulse sequence $A_\mathrm{i}(t)$ only depends on temporal parameters as τ or Δ. Therefore, this term is constant during an entire NMR experiment and results only in an unknown, but constant signal attenuation. So the signal attenuation caused by PFGs and CFGs is still the same, only with an additional offset. Diffusion is determined from the slope of the signal attenuation with increasing PFG amplitude and can therefore still be obtained. In contrast to Eq. (5.17a) the so called cross term $A_\mathrm{c}(t)$ between the pulsed and constant field gradients depends only linearly on $\boldsymbol{G}(t)$. This term introduces a non-quadratic dependence to the signal in contrast to Eq. (5.13). Due to the unknown internal field gradients the cross term can significantly complicate or even inhibit the correct determination of diffusion coefficients with PFG NMR.

In summary, a spin echo pulse sequence distorted by internal field gradients gives the following contributions to the spin echo attenuation at $t_e = 2\tau$ [ST65]:

$$A_p(t_e) = \delta^2 \left(\Delta - \tfrac{1}{3}\delta\right) \boldsymbol{G}^2, \tag{5.18a}$$

$$A_c(t_e) = \delta \left[2\tau^2 - \tfrac{2}{3}\delta^2 - (\delta_1^2 + \delta_2^2) - \delta(\delta_1 + \delta_2)\right] \boldsymbol{G}\boldsymbol{g}, \tag{5.18b}$$

$$A_i(t_e) = \tfrac{2}{3}\tau^3 \boldsymbol{g}^2. \tag{5.18c}$$

Since the internal gradients are assumed to be constant, they are omitted in the following pulse sequence plots.

5.1.4. The stimulated echo

In many materials, especially in natural porous media such as soil, the transverse relaxation time T_2 is considerably shorter than T_1. This is advantageous, if coherence is to be stored for a longer time. Assume that the macroscopic transverse magnetization M_{xy} is required to be stored for later recall. The method used for storing is shown in Figure 5.4.

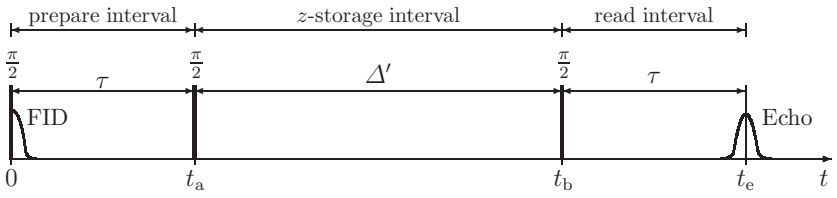

Figure 5.4: *Scheme of the rf pulses applied in a stimulated echo pulse sequence with the prepare, storage and read interval.*

Here, at $t = t_a$ a 90° pulse rotates the transverse magnetization into a longitudinal magnetization M_z. In this state only T_1 relaxation will occur. Depending on the direction in which the pulse is applied, the 90° pulse affects only the magnetization either in x or y direction. Therefore, only half the transverse magnetization can be stored in this way. The magnetization is recalled after the storage time Δ' at $t = t_b$ using another 90° pulse. This leads to an echo after the time interval τ at $t_e = \Delta' + 2\tau$ after the first excitation pulse. The echo shows the macroscopic

magnetization $M_{xy}(t_e)$ [Tan70]:

$$M_{xy}(t_e) = \tfrac{1}{2} M(0) \exp\left\{-\frac{2\tau}{T_2} - \frac{\Delta'}{T_1}\right\} \tag{5.19}$$

This pulse sequence, known as stimulated echo pulse sequence [Hah50], is of particular importance in NMR imaging applications [FMH85], especially by measuring the translational motion of molecules using pulsed field gradient methods.

5.1.5. Stimulated echo with pulsed field gradients

The stimulated echo pulse sequence also generates two additional spin echoes. First, an echo of the initial pulse FID induced by the second pulse appears. After that, there is an echo of the second pulse FID induced by the third pulse. An efficient approach to avoid interference between the stimulated echo and the two spin echoes is the insertion of a field gradient pulse. Applying such a spoiler during the storage period Δ' (in the interests of clarity not shown in following schemes of pulse sequences) destroys the unwanted transverse magnetization without influencing the magnetization which has been stored along the z direction.

The pulse sequence of Tanner [Tan70] combines pulsed field gradients with the stimulated echo pulse sequence and is shown in Figure 5.5.

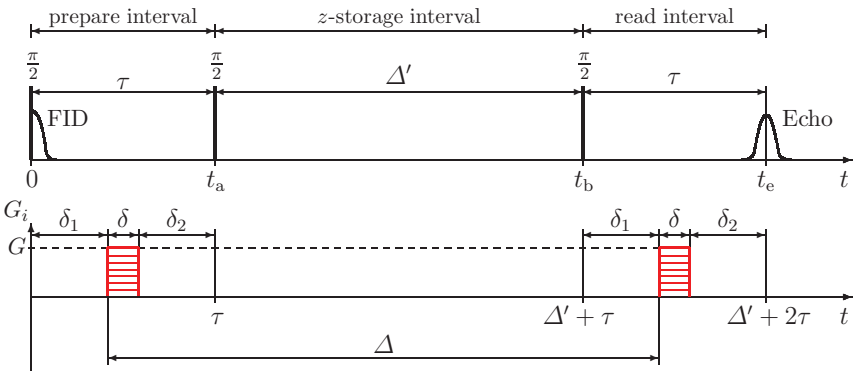

Figure 5.5: *Stimulated echo pulse sequence with pulsed field gradients* $\boldsymbol{G}$ *as introduced by Tanner [Tan70].* G_i *stands for any direction (x, y, and z) of the gradient in the laboratory coordinate system.*

During the storage time Δ' field gradients have no influence on the magnetization stored in z direction [Tan70]. Therefore, the effective field gradient becomes $\boldsymbol{g}^*(t) = \boldsymbol{G}^*(t) = 0$. Also the integral over these gradients disappears.

Following Cotts et al. [CHS89], two conditions exist for the formation of a stimulated echo. The first one (Condition I) employs the integral over the effective field gradients during the preparation time,

$$I_\mathrm{p}(t) = \int_0^t \mathrm{d}t' \left[\boldsymbol{G}^*(t') + \boldsymbol{g}^*(t')\right], \tag{5.20}$$

and the integral over the effective field gradients during the reading time,

$$I_\mathrm{r}(t) = \int_{t_\mathrm{b}}^t \mathrm{d}t' \left[\boldsymbol{G}^*(t') + \boldsymbol{g}^*(t')\right]. \tag{5.21}$$

Condition I requires the following relationship:

$$0 = I_\mathrm{p}(t_\mathrm{a}) - I_\mathrm{r}(t_\mathrm{e}). \tag{5.22}$$

However, a stimulated spin echo also appears, if both integrals have different sign,

$$0 = I_\mathrm{p}(t_\mathrm{a}) + I_\mathrm{r}(t_\mathrm{e}), \tag{5.23}$$

which is called Condition II. Therefore, Condition II is equivalent to the echo condition of Eq. (5.3) since the effective field gradients disappear during the storage time. In contrast, Condition I is not equivalent to Eq. (5.3). Thus, Eq. (5.11) has to be rewritten for Condition I by separating Eq. (5.11) in three parts corresponding to the three time intervals "preparing", "storing" and "reading" shown in Figure 5.5:

$$S(t_\mathrm{e}) = S(0) \exp\left\{-D\gamma^2 \left[\int_0^{t_\mathrm{a}} \mathrm{d}t I_\mathrm{p}^2(t) + \Delta' I_\mathrm{p}^2(t_\mathrm{a}) + \int_{t_\mathrm{b}}^{t_\mathrm{e}} \mathrm{d}t \left\{I_\mathrm{p}(t_\mathrm{a}) - I_\mathrm{r}(t)\right\}^2\right]\right\}. \tag{5.24}$$

The integral over the storage time Δ' is already calculated since the integrand stays constant in $t_\mathrm{a} \leq t \leq t_\mathrm{b}$.

Following Cotts et al. [CHS89] there is no principal difference between the magnetization shortly before the first and shortly before the third 90° pulse since only M_z is of interest. Therefore, it is physically useful to assume the repetition of the effective field gradient, $\boldsymbol{g}^*(0) = \boldsymbol{g}^*(t_\mathrm{b})$. Thus, the reference system for the direction of all effective field gradients is given by the constant gradients. Now, the pulsed field gradients $\boldsymbol{G}^*(t)$ have to be chosen such that Condition I or II is fulfilled.

According to the last section, in the intervals $0 \leq t \leq \tau$ and $\Delta' + \tau \leq t \leq \Delta' + 2\tau$ the effective constant field gradients have to be $\boldsymbol{g}^*(t) = \boldsymbol{g}$ and also $\boldsymbol{G}^*(t) = \boldsymbol{G}(t)$. Except for the disappearing effective constant field gradient during Δ', in this pulse sequence the effective field gradients are identical to the gradients in the laboratory coordinate frame and obviously only Condition I is fulfilled.

Using the PFGs shown in Figure 5.5 as effective gradients, for the spin echo attenuation part follows with Condition I and Eq. (5.17) [Tan70]

$$A_\mathrm{p}(t_\mathrm{e}) = \delta^2 \left(\Delta - \tfrac{1}{3}\delta\right) \boldsymbol{G}^2, \tag{5.25a}$$

$$A_\mathrm{c}(t_\mathrm{e}) = \delta \left[2\tau(\Delta' + \tau) - \tfrac{2}{3}\delta^2 - (\delta_1^2 + \delta_2^2) - \delta(\delta_1 + \delta_2)\right] \boldsymbol{G}\boldsymbol{g}, \tag{5.25b}$$

$$A_\mathrm{i}(t_\mathrm{e}) = \tau^2(\Delta' + \tfrac{2}{3}\tau)\boldsymbol{g}^2. \tag{5.25c}$$

Comparing Eq. (5.25) and Eq. (5.18), the same expression results for $\Delta' = 0$.

5.1.6. The 13-interval pulse sequence

The introduction of alternating pulsed field gradients (APFGs) by Karlicek and Lowe [KL80] was the precondition to reduce or suppress the influence of the cross term Eq. (5.17b). Cotts et al. [CHS89] suggested in total six pulse sequences based on the stimulated echo with additional rf pulses during the preparation and reading times. These pulse sequences are called 9-, 13- and 17-interval pulse sequences. Each pulse sequence is performed for Condition I or II. The names result from the number of time intervals with constant effective field gradients. All six pulse sequences were developed to reduce the influence of internal field gradients. In this thesis only the 13-interval pulse sequence according to Condition I was used. This pulse sequence is shown in Figure 5.6.

The principle is based on changing the sign of the effective constant field gradients similar to the pulse sequences introduced by Karlicek and Lowe [KL80]. Therefore, the 13-interval pulse sequence following Condition I results in the terms for the spin

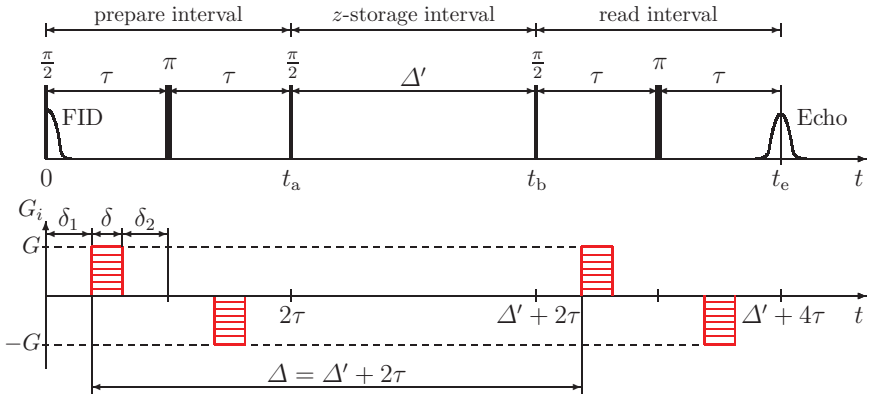

Figure 5.6: *13-interval pulse sequence with pulsed field gradients* $\boldsymbol{G}$ *following Condition I as introduced by Cotts et al. [CHS89]. The gradient pulse duration* δ *and the distance from the previous applied rf pulse* δ_1 *are the same for all four intervals with the duration* τ*.* G_i *represents any direction (*x*,* y*, and* z*) in the laboratory coordinate system.*

echo attenuation

$$A_\mathrm{p}(t_\mathrm{e}) = \delta^2 \left[4(\Delta' + \tau) + 2\tau - \tfrac{2}{3}\delta\right] \boldsymbol{G}^2, \tag{5.26a}$$

$$A_\mathrm{c}(t_\mathrm{e}) = 2\delta\tau(\delta_1 - \delta_2)\boldsymbol{G}\boldsymbol{g}, \tag{5.26b}$$

$$A_\mathrm{i}(t_\mathrm{e}) = \tfrac{4}{3}\tau^3 \boldsymbol{g}^2. \tag{5.26c}$$

If the PFGs are centered in the τ-intervals between the rf pulses, it follows the relation

$$\delta_1 = \delta_2 = \tfrac{1}{2}(\tau - \delta), \tag{5.27}$$

so the cross term $A_\mathrm{c}(t_\mathrm{e})$ disappears.

Furthermore, the term $A_\mathrm{i}(t_\mathrm{e})$ describing the pure influence of internal field gradients does no longer depend on the storage time Δ'. The reason is that at $t = t_\mathrm{a}$ the integral of $\boldsymbol{g}^*(t)$ is zero and does therefore not contribute to $I_\mathrm{p}(t_\mathrm{a})$ in Eq. (5.20). For NMR samples with high internal field gradients and for the observation of large displacements, respectively, this can result in a significantly improved signal compared to the conventional stimulated echo pulse sequence. This results from comparing $A_\mathrm{i}(t_\mathrm{e})$ in Eq. (5.25) and Eq. (5.26).

Choosing the delays δ_1 and δ_2 according to Eq. (5.27) this opens the possibility to reduce or even suppress the influence of the cross term $A_\mathrm{c}(t_\mathrm{e})$. With that, the 13-interval pulse sequence is a powerful tool for NMR investigations on samples with high internal field gradients such as natural porous media.

5.1.7. Theory of PFG NMR with anisotropic diffusion

For convenience, the described pulse sequences spin echo and stimulated echo assume isotropic diffusion in the sample, expressed by one single diffusion coefficient. However, especially for water motion in plant roots anisotropic diffusion can be expected due to the tube-shape of the vascular bundles. Anisotropic diffusion behavior can be described by the diffusion tensor as introduced in Chapter 3. In this chapter the influence of field gradients on the NMR signal at the presence of a diffusion tensor $\mathbf{D}$ is discussed.

Investigating $\mathbf{D}$ with PFG NMR leads to a more general NMR signal in the Bloch-Torrey equation (Eq. (5.4)). The following considerations follow the concept of Stejskal [Ste65].

For anisotropic samples Eq. (5.6) has to be generalized using a diffusion tensor instead of a diffusion coefficient. The second term on the right becomes similar to the last term of the Bloch-Torrey equation:

$$\frac{\partial \mathcal{M}(\boldsymbol{r},t)}{\partial t} = \left[\mathrm{i}\,\gamma B_z(\boldsymbol{r},t) - \frac{1}{T_2} + \nabla \mathbf{D} \nabla\right] \mathcal{M}(\boldsymbol{r},t). \tag{5.28}$$

With Eq. (5.7),

$$\begin{aligned}\mathcal{M}(\boldsymbol{r},t) &= S(t) \exp\left\{-\frac{t}{T_2} - \mathrm{i}\,\gamma \int_0^t \mathrm{d}t' B_z(\boldsymbol{r},t')\right\} \\ &= S(t) \exp\left\{-\frac{t}{T_2} - \mathrm{i}\,\gamma\,\boldsymbol{r} \int_0^t \mathrm{d}t' \left[\boldsymbol{G}^*(t') + \boldsymbol{g}^*(t')\right]\right\},\end{aligned} \tag{5.29}$$

the NMR signal $S(t)$ with the effective PFG $\boldsymbol{G}^*(t)$ results in:

$$S(t) = S(0) \tag{5.30}$$
$$\cdot \exp\left\{-\gamma^2 \int_0^t \mathrm{d}t' \left[\left(\int_0^{t'} \mathrm{d}t'' [\boldsymbol{G}^{*\mathrm{T}}(t'') + \boldsymbol{g}^{*\mathrm{T}}(t'')] \right) \mathbf{D} \left(\int_0^{t'} \mathrm{d}t'' [\boldsymbol{G}^{*}(t'') + \boldsymbol{g}^{*}(t'')] \right) \right] \right\},$$

also assuming influences of internal field gradients to the NMR signal by $\boldsymbol{g}^*(t)$. $\boldsymbol{G}^{*\mathrm{T}}$ and $\boldsymbol{g}^{*\mathrm{T}}$ are the transposed vectors of $\boldsymbol{G}^*$ and $\boldsymbol{g}^*$, respectively. For isotropic diffusion Eq. (5.30) simplifies to the double integral solution in Eq. (5.11).

Similar to Eq. (5.11) it is possible to split the influences of applied and constant field gradients as

$$S(t) = S(0) \exp\left\{-\gamma^2 \left[A_{\mathrm{p,gen}}(t) + A_{\mathrm{c,gen}}(t) + A_{\mathrm{i,gen}}(t)\right]\right\} \quad \text{with} \tag{5.31}$$

$$\begin{aligned} A_{\mathrm{p,gen}}(t) &= \int_0^t \mathrm{d}t' \left(\int_0^{t'} \mathrm{d}t'' \boldsymbol{G}^{*\mathrm{T}}(t'') \right) \mathbf{D} \left(\int_0^{t'} \mathrm{d}t'' \boldsymbol{G}^{*}(t'') \right) \\ &= A'_{\mathrm{p,gen}}\, \boldsymbol{G}^{*\mathrm{T}}\, \mathbf{D}\, \boldsymbol{G}^{*}, \end{aligned} \tag{5.31a}$$

$$\begin{aligned} A_{\mathrm{c,gen}}(t) &= \int_0^t \mathrm{d}t' \left(\int_0^{t'} \mathrm{d}t'' \boldsymbol{G}^{*\mathrm{T}}(t'') \right) \mathbf{D} \left(\int_0^{t'} \mathrm{d}t'' \boldsymbol{g}^{*}(t'') \right) \\ &\quad + \int_0^t \mathrm{d}t' \left(\int_0^{t'} \mathrm{d}t'' \boldsymbol{g}^{*\mathrm{T}}(t'') \right) \mathbf{D} \left(\int_0^{t'} \mathrm{d}t'' \boldsymbol{G}^{*}(t'') \right) \\ &= \tfrac{1}{2} A'_{\mathrm{c,gen}} \left[\boldsymbol{G}^{*\mathrm{T}}\, \mathbf{D}\, \boldsymbol{g}^{*} + \boldsymbol{g}^{*\mathrm{T}}\, \mathbf{D} \boldsymbol{G}^{*}\right] = A'_{\mathrm{c,gen}}\, \boldsymbol{G}^{*\mathrm{T}} \mathbf{D}\, \boldsymbol{g}^{*}, \end{aligned} \tag{5.31b}$$

$$\begin{aligned} A_{\mathrm{i,gen}}(t) &= \int_0^t \mathrm{d}t' \left(\int_0^{t'} \mathrm{d}t'' \boldsymbol{g}^{*\mathrm{T}}(t'') \right) \mathbf{D} \left(\int_0^{t'} \mathrm{d}t'' \boldsymbol{g}^{*}(t'') \right) \\ &= A'_{\mathrm{i,gen}}\, \boldsymbol{g}^{*\mathrm{T}}\, \mathbf{D}\, \boldsymbol{g}^{*}. \end{aligned} \tag{5.31c}$$

$A_{\mathrm{p,gen}}(t)$, $A_{\mathrm{c,gen}}(t)$ and $A_{\mathrm{i,gen}}(t)$ are the generalized terms of Eq. (5.17) contributing to the NMR signal. The simplifying terms $A'_{\mathrm{p,gen}}$, $A'_{\mathrm{c,gen}}$ and $A'_{\mathrm{i,gen}}$ are justified for rectangular PFGs and denote the pulse sequence timing on the NMR signal. Due to the symmetric diffusion tensor (see Chapter 3.2) both matrix multiplications $\boldsymbol{G}^{*\mathrm{T}}\, \mathbf{D}\, \boldsymbol{g}^{*}$ and $\boldsymbol{g}^{*\mathrm{T}}\, \mathbf{D}\, \boldsymbol{G}^{*}$ in Eq. (5.31b) result in the same expression. Therefore, both terms can be combined by taking a factor of two into account.

In the literature it is common to introduce the so called **b**-matrix [BML94] for simplification of the term $A_{\mathrm{p,gen}}(t)$ in Eq. (5.31a).

$$\begin{aligned} A_{\mathrm{p,gen}}(t) &= \int_0^t \mathrm{d}t' \left(\int_0^{t'} \mathrm{d}t'' \boldsymbol{G}^{*\mathrm{T}}(t'') \right) \mathbf{D} \left(\int_0^{t'} \mathrm{d}t'' \boldsymbol{G}^{*}(t'') \right) \\ &= \int_0^t \mathrm{d}t' \left(\int_0^{t'} \mathrm{d}t'' \boldsymbol{G}^{*}(t'') \right) \left(\int_0^{t'} \mathrm{d}t'' \boldsymbol{G}^{*\mathrm{T}}(t'') \right) \mathbf{D} \\ &= \frac{1}{\gamma^2} \mathbf{b}\,\mathbf{D} \end{aligned} \tag{5.32}$$

The diffusion tensor **D** is defined as an average value of the exponent in Eq. (5.31a) over the time interval $t = [\,0;\, t_{\mathrm{e}}]$. The symmetric **b**-matrix is defined as

$$\mathbf{b} = \gamma^2 \int_0^t \mathrm{d}t' \left(\int_0^{t'} \mathrm{d}t'' \boldsymbol{G}^{*}(t'') \right) \left(\int_0^{t'} \mathrm{d}t'' \boldsymbol{G}^{*\mathrm{T}}(t'') \right). \tag{5.33}$$

Without internal field gradients, inserting the **b**-matrix definition of Eq. (5.33) in Eq. (5.31a), the NMR signal of Eq. (5.31) simplifies to

$$S(t) = S(0) \exp\{-\mathbf{b}\,\mathbf{D}\} = S(0) \exp\left\{ - \sum_{i=x,y,z} \sum_{j=x,y,z} b_{ij} D_{ij} \right\}. \tag{5.34}$$

b_{ij} and D_{ij} are the ijth element of the **b**-matrix and the diffusion tensor, respectively. This equation can be linearized by:

$$\ln\left\{ \frac{S(t)}{S(0)} \right\} = -\mathbf{b}\,\mathbf{D} = - \sum_{i=x,y,z} \sum_{j=x,y,z} b_{ij} D_{ij}, \tag{5.35}$$

which is useful for fitting data as shown in Chapter 7.1.3.

The **b**-matrices for the spin echo and stimulated echo pulse sequences look similar to the 1D form in Eq. (5.18),

$$\mathbf{b} = (\gamma G \delta)^2 \left(\Delta - \tfrac{1}{3}\delta \right) \frac{1}{|\boldsymbol{G}|^2} \boldsymbol{G}\,\boldsymbol{G}^{\mathrm{T}}. \tag{5.36}$$

This **b**-matrix is formed by the product of the normalized $\boldsymbol{G}$ with its transposed form $\boldsymbol{G}^{\mathrm{T}}$. This also results for PFGs in the stimulated echo pulse sequence.

If the duration of the PFGs δ is small compared to the observation time Δ (as

$\frac{1}{3}\,\delta \ll \Delta$), the result becomes even simpler:

$$\mathbf{b} = (\gamma G\delta)^2 \Delta \frac{1}{|\boldsymbol{G}|^2} \boldsymbol{G}\,\boldsymbol{G}^{\mathrm{T}} = 4\pi^2 \Delta\, \boldsymbol{q}\,\boldsymbol{q}^{\mathrm{T}}. \tag{5.37}$$

The expression for the $\mathbf{b}$-matrix was redefined by using the definition of the reciprocal velocity vector $\boldsymbol{q}(t)$ as defined in Eq. (4.2.1) of Chapter 4.2.1 [Cal91, ST65],

$$\boldsymbol{q}(t) = \frac{\gamma}{2\pi} \int_0^t \mathrm{d}t' \boldsymbol{G}(t'), \tag{5.38}$$

whose direction is given by $\boldsymbol{G}$, and t represents the pulse duration. Thus, inserting Eq. (5.37) in Eq. (5.34) leads to the NMR signal

$$S(t) = S(0) \exp\left\{-4\pi^2 \Delta\, \boldsymbol{q}^{\mathrm{T}}\, \mathbf{D}\, \boldsymbol{q}\right\}. \tag{5.39}$$

Both the $\mathbf{b}$-matrix and the $\boldsymbol{q}$-vector are commonly used describing diffusion and flow processes. Thereby, the term "$\mathbf{b}$-matrix" is more often used in medical diffusion imaging terminology while the expression "$\boldsymbol{q}$-vector" is conventionally used in spectroscopic diffusion and flow investigations. Since this work consists of both imaging and spectroscopic experiments, both terms are used with respect to the subject in the following.

5.2. The 2D pulse sequence DDCOSY

The pulse sequences which are described in Chapter 5.1 give information about diffusion properties in the main directions x, y, and z. However, they cannot give information about correlations between these directions that occur for instance in the presence of anisotropies.

Correlations can be investigated with a two-dimensional pulse sequence as suggested by Callaghan et al. [CGR03]. The sequence determines the conditional probability of diffusion in one direction depending on diffusion in another, usually perpendicular direction. As the 1D pulse sequences presented in Chapter 5.1, this 2D pulse sequence also provides no spatial resolution. "Two-dimensional" refers to two individual PFG diffusion sub-experiments with independent gradient strength. Therefore, the sequence is called Diffusion Diffusion COrrelation SpectroscopY (DD-

COSY). Figure 5.7 shows a scheme of this pulse sequence.

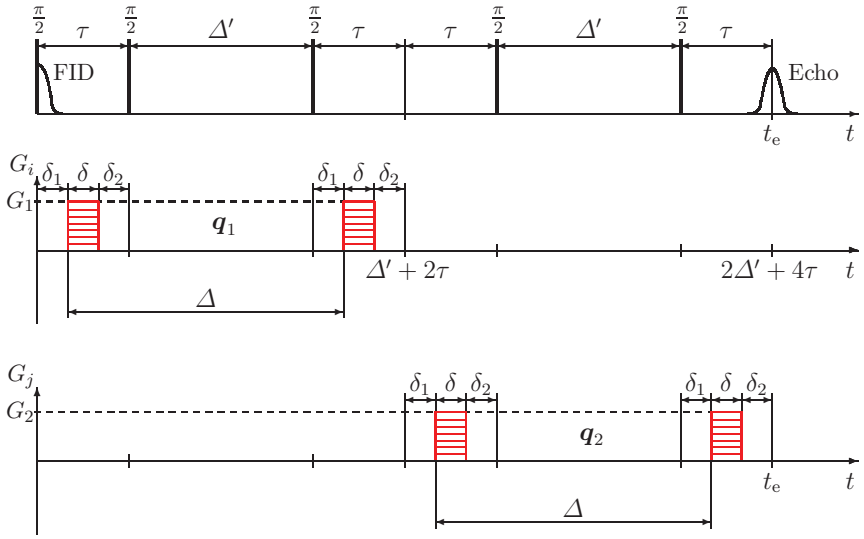

Figure 5.7: *Diffusion diffusion correlation spectroscopy pulse sequence (DDCOSY) based on the stimulated echo pulse sequence. The necessary gradient steps q_1 and q_2 of each PFG pair $\boldsymbol{q}_1$ and $\boldsymbol{q}_2$, respectively, are indicated by the horizontal lines inside the gradient pulses. G_i and G_j represent any perturbation of x, y and z in the laboratory coordinate system. The PFG pairs can also be applied in the same direction ($i = j$).*

DDCOSY is based on the stimulated echo pulse sequence presented in Chapters 5.1.4 and 5.1.5. Instead of recording the spin echo after the first stimulated echo experiment at $t = \Delta' + 2\tau$, a second stimulated echo experiment is added at this time. Since for the second experiment the magnetization is already transverse, the first 90° pulse is not employed. After the time τ the magnetization is stored in z direction again by a 90° pulse. After a storage time Δ' the magnetization is brought back into the xy plane with the last 90° pulse. Finally, the spin echo is recorded at $t = t_e = 2\Delta' + 4\tau$.

In the following the term inverse velocity vector $\boldsymbol{q}$ as introduced in Chapter 5.1.7 and the term PFG are used as synonyms, since the $\boldsymbol{q}$-vector is proportional to the PFG according to Eq. (5.38).

During the measurements, one pair of PFGs $\boldsymbol{q}_1$ is increased stepwise while the

other pair $\boldsymbol{q}_2$ stays at a constant value. When all steps q_1 in one observation direction are completed, the gradient strength of the second pair is increased until after q_2 steps also this observation direction is complete. The resulting data set has a size of $q_1 \times q_2$.

The PFG pairs can point in all combinations of directions $i, j = x, y, z$. The direction can also be the same within a PFG pair ($i = j$).

Similar to the one-dimensional case of PFGs introduced in Eq. (5.39) the NMR signal in the two-dimensional DDCOSY experiment becomes [Cal91, CCS99, CF04]

$$S(t) = S(0) \exp\left\{-4\pi\Delta\left(\boldsymbol{q}_1^{\mathrm{T}}\,\mathbf{D}\,\boldsymbol{q}_1 + \boldsymbol{q}_2^{\mathrm{T}}\,\mathbf{D}\,\boldsymbol{q}_2\right)\right\}. \tag{5.40}$$

Using the PFGs shown in Figure 5.7 as effective gradients, for the signal attenuation according to Eq. (5.31) follows

$$A'_{\mathrm{p}} = 2\delta^2\left(\Delta - \tfrac{1}{3}\delta\right), \tag{5.41a}$$

$$A'_{\mathrm{c}} = 2\delta\left[2\tau(\Delta' + \tau) - \tfrac{2}{3}\delta^2 - (\delta_1^2 + \delta_2^2) - \delta(\delta_1 + \delta_2)\right], \tag{5.41b}$$

$$A'_{\mathrm{i}} = 2\tau^2(\Delta' + \tfrac{2}{3}\tau). \tag{5.41c}$$

The three terms A'_{p}, A'_{c} and A'_{i} describing the influence of the pulse sequence timing on the NMR signal were introduced in Eq. (5.31). In contrast to the 1D stimulated echo with PFGs of Chapter 5.1.5 all three terms in Eq. (5.41) are doubled compared to the 1D case in Eq. (5.17).

The two-dimensional inverse Laplace transformation analyses correlations between the diffusion coefficients and plots the results in 2D maps such as presented in Figure 5.8.

The axes of the map represent the observed diffusion directions. In Figure 5.8, four different scenarios of two-dimensional artificial diffusion coefficient distributions are shown. The diffusion coefficients D_i and D_j are given in arbitrary units on logarithmic scales, whereby i and j denote any direction in the laboratory coordinate system. The color bars denote the probability of finding diffusion coefficients with the respective values. The probability is also given in arbitrary units.

One single peak on the diagonal of the map as shown in the top left panel in Figure 5.8 appears under three scenarios. First, in a completely isotropic sample with unrestricted diffusion, diffusion is governed by the same free diffusion coefficient in any direction. Second, both PFGs are applied in the same direction, $i = j$. Third,

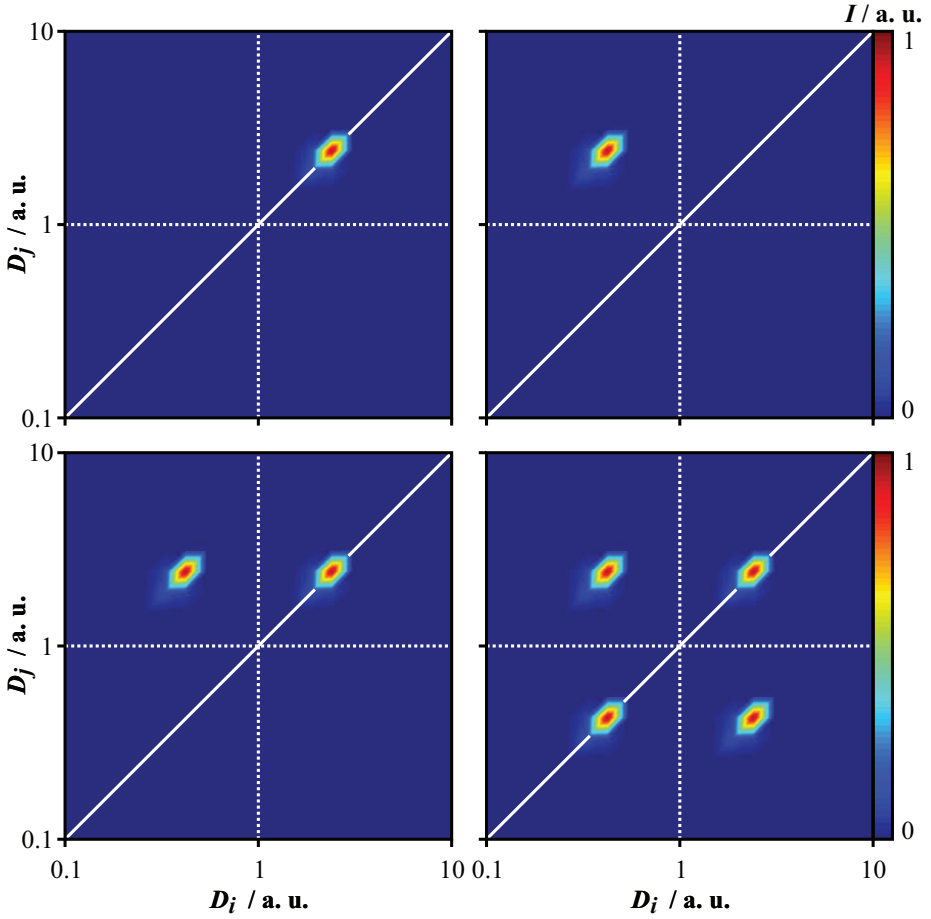

Figure 5.8: *Exemplary 2D maps of diffusion coefficient distributions resulting from measurements with the DDCOSY pulse sequence. Presented are four different possible scenarios of diffusion distributions (isotropy, anisotropy, restricted diffusion), which are discussed in the text in detail. The diffusion coefficients D_i and D_j plotted on the horizontal and vertical axes represent any perturbation of x, y and z in the laboratory coordinate system. For convenience, they are given in arbitrary units on logarithmic scales, since this representation shows no actually measured data. The color bars indicate in arbitrary units the probability of diffusion coefficients at different values. The diagonal line in each plot represents the position of isotropic diffusion.*

in the case of isotropically restricted diffusion, for example of water in spherical plant cells.

If the diffusion coefficient in one direction differs from the value in the second observed direction, the peak appears no longer on the diagonal. This is shown in the top right panel in Figure 5.8. Instead, such an off-diagonal peak indicates macroscopic and microscopic anisotropy in the sample. Such behavior can be expected for water in tube-shaped vascular bundles in a plant stem. In the case of a plant stem orientation along one observation direction, the diffusion coefficient perpendicular to the plant stem will be restricted and therefore reduced to the value of free diffusion parallel to the vascular bundles.

The situation becomes more complicated, if the conventional 1D spectrum of diffusion coefficients D_i shows two peaks, indicating two diffusion coefficients from free diffusion and restricted diffusion. Still, this 1D spectrum yields no information about anisotropies. A qualitative statement about anisotropy can be obtained, if diffusion in two perpendicular directions is investigated. Two peaks in the 2D map of such a DDCOSY measurement can appear as shown in the bottom left panel in Figure 5.8. While the projection of diffusion coefficient on the i direction shows still two peaks, in the j direction appears only one single peak. This is plotted as one diagonal and one off-diagonal peak in the shown 2D map. Thereby, the diagonal peak represents isotropic diffusion while the off-diagonal peak denotes restricted and anisotropic diffusion. Such behavior can be found for instance probing parallel arranged tubes with two different diameters, whereas the larger diameter allows free diffusion. While in this case free diffusion can be observed along the tubes, in perpendicular observation direction two diffusion coefficients appear. Thereby, the diagonal peak belongs to molecules in the tubes with larger diameter, and the off-diagonal peaks results from restricted and anisotropic diffusion in the smaller tubes. Note that such a 2D map results only from samples with macroscopic anisotropy, i.e. diffusion is anisotropic also in the microscopic range.

The DDCOSY map becomes even more useful, if the 1D diffusion coefficient spectrum shows more than two peaks.

In the case of a sample which is macroscopically isotropic, it is interesting to study the diffusion behavior on the microscopic scale. Microscopic anisotropies always appear as two peaks symmetric to the diagonal but far away from that line. The reason for the symmetry is that the sample does not depend on the observation direction in the laboratory coordinate system. An example for such a possible observation is shown in the bottom right panel in Figure 5.8. In this map both diagonal and off-diagonal peaks appear. This means diffusion is both free

and restricted, i.e. anisotropic, in both examined directions. Such behavior can again be described with tubes having two different diameters. However, this time, the tubes are cut in small pieces but still long enough to allow free diffusion. If the tubes are randomly oriented, the sample is macroscopically isotropic. Only the two-dimensional DDCOSY measurement shows that beside isotropic free diffusion in the thicker tubes, diffusion is anisotropic in the thinner tubes. Since the tubes are randomly orientated, diffusion is restricted in both observed directions, resulting in the off-diagonal peaks as well as in the diagonal peak at a lower value than the free diffusion peak.

This is an example where a macroscopically isotropic sample shows microscopic anisotropy. It demonstrates that it is possible to distinguish between macroscopic and microscopic diffusion using the DDCOSY pulse sequence.

5.3. Magnetic resonance imaging pulse sequences

Pulsed magnetic field gradients have been introduced as essential parts of MRI in Chapter 4.2. This section starts with describing imaging pulse sequences on the basis of spin echo and stimulated echo pulse sequences employed in the experiments discussed later. The section also introduces the pulse sequence used for diffusion tensor imaging (DTI). This is a standard pulse sequence and was not modified in the experiments. Finally, the concept of flow-encoding is introduced.

5.3.1. Imaging with the spin echo pulse sequence

Figure 5.9 shows a spin echo pulse sequence which provides the easiest way to get a spatially resolved NMR image.

The general concept of the spin echo pulse sequence was already outlined in Chapter 5.1.1. In contrast to this method, soft exciting 90° and refocusing 180° pulses are commonly used for slice selection here [Blu00, Cal91]. An echo is received at $t = t_e = 2\tau$. Thereby, τ is defined from the center of the 90° pulse to the center of the 180° pulse. Adding τ to the center of the 180° pulse leads to the center of the MRI signal. At this time, the spins have highest coherence.

During the application of the soft 90° and 180° pulses the slice selective field gradient G_s is applied. All MRI investigations presented in this work were performed with slice selection in z direction of the laboratory coordinate system as shown in

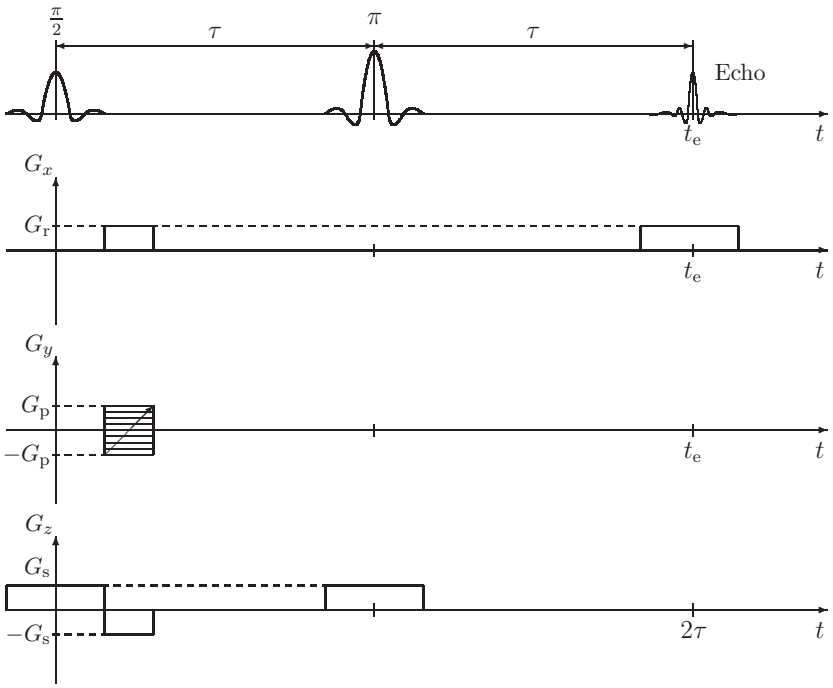

Figure 5.9: *Spin echo pulse sequence with imaging field gradients for read out (G_r, in this pulse sequence applied in x direction), phase-encoding (G_p, applied in y direction) and slice selection (G_s, applied in z direction). Instead of exciting the entire sample with hard pulses, soft* 90° *and* 180° *pulses are chosen for slice selective excitation.*

Figure 5.9. In general, it is also possible to apply the slice selection in x or y direction. The spins dephase already during G_s similar as in diffusion experiments. Thus, rephasing takes place right after the first slice selective field gradient. Since all spins of the selected slice are in the xy plane at the center of G_s and dephasing starts at this time, only half of the field gradient is necessary to rephase the spins. Strictly speaking, the area of the refocusing gradient (having rectangular shape) must be half of the area of the slice selective gradient. Due to the inversion effect of 180° pulses on field gradients as introduced in Chapter 5.1.2, the second slice selective field gradient does not have to be refocused. The rephasing already occurs during the 180° pulse application from the time center of the pulse until the end of the applied gradient.

So far, with the slice selective gradient in combination with the soft rf pulses it is possible to select one specific slice of the sample.

According to Chapter 4.2, there are two possibilities to spatially resolve a slice in an NMR experiment. One is frequency-encoding as drawn for x direction in Figure 5.9. The first read out field gradient in this pulse sequence is applied at the same time and with the same duration as the refocusing slice selective gradient after the exciting 90° pulse. During the NMR echo sampling this gradient is applied again and ensures spatial resolution of the NMR image in x direction. Next, the phase-encoding gradient is applied in y direction at the same time and with the same duration as the refocusing slice selective gradient and the read out gradient.

The recorded NMR signal is time dependent (Eq. (4.15)). k_x (Eq. (4.23a)) is called frequency-encoding and k_y (Eq. (4.23b)) is called phase-encoding. The final NMR image is the Fourier transform of the NMR signal following Eq. (4.21b).

5.3.2. Diffusion tensor imaging pulse sequence

As a major part of this work, the technique of diffusion tensor imaging (DTI) was transferred to the application on plant roots. DTI enables to obtain the entire root system structure of a plant without any gaps caused by imaging artifacts such as susceptibility effects. DTI is a well known technique in medical imaging [BML94]. In the presented thesis it is used for investigating water motion inside plant roots for the first time. Figure 5.10 shows the employed DTI pulse sequence.

The DTI pulse sequence is a combination of the spin echo imaging pulse sequence (Chapter 5.3.1) and PFGs (Chapter 5.1.2). The advantage of DTI is to spatially resolve the diffusion behavior and to distinguish isotropic regions from anisotropic regions in a sample. A common application is the reconstruction of preferred structures or path ways in case of continuously anisotropic diffusion over several pixels. The essence of DTI is the determination of the diffusion tensor for each single pixel.

Determining diffusion tensors means to record the NMR signal at different applied field gradients (Eq. (5.34)). Since the diffusion tensor is symmetric ($\mathbf{D}^{\mathrm{T}} = \mathbf{D}$), Eq. (5.34) can be written as

$$\begin{aligned} S(t) &= S(0) \exp\left\{ - \sum_{i=x,y,z} \sum_{j=x,y,z} b_{ij} D_{ij} \right\} \qquad (5.42) \\ &= S(0) \exp\left\{ -(b_{xx}D_{xx} + b_{yy}D_{yy} + b_{zz}D_{zz} + 2\,b_{xy}D_{xy} + 2\,b_{xz}D_{xz} + 2\,b_{yz}D_{yz}) \right\}. \end{aligned}$$

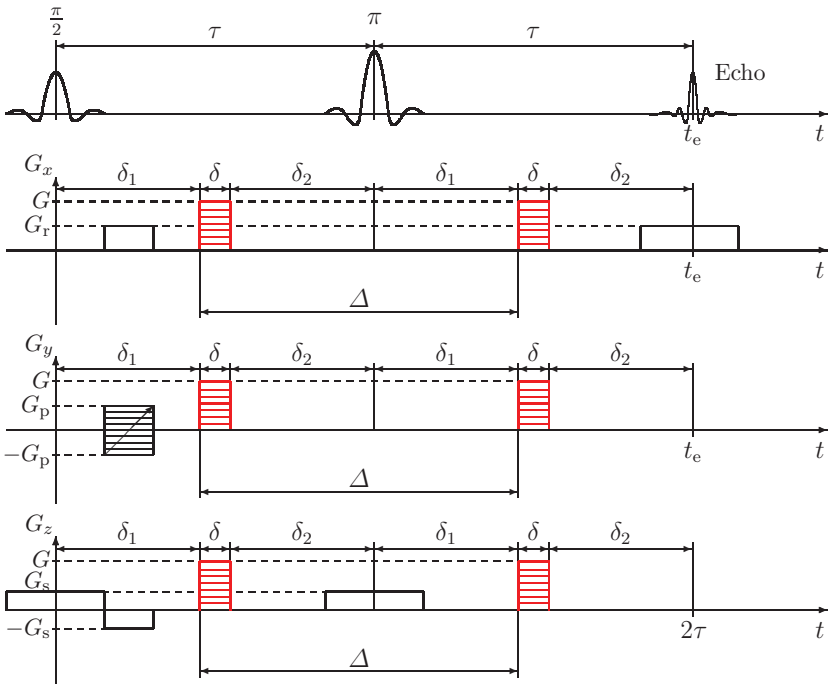

Figure 5.10: *Diffusion tensor imaging pulse sequence (DTI) with imaging field gradients read out in x direction, phase-encoding in y direction and slice-encoding in z direction. PFGs for diffusion-encoding can be applied both separately in each single direction as well as in each desired linear combination of the unit vectors of the laboratory coordinate system.*

In DTI experiments, PFGs applied to six different directions are required to obtain all six different entries of the diffusion tensor (D_{xx}, D_{yy}, D_{zz}, and D_{xy}, D_{xz}, D_{yz}) in six different experiments. The application of only one PFG direction, for example in x direction, results in one single term contributing to the signal loss depending on the PFG amplitude,

$$S(t) = S(0) \exp\{-b_{xx} D_{xx}\}. \tag{5.43}$$

Recording this NMR signal at different PFG amplitudes allows the determination of the diffusion coefficient D_{xx} for each single pixel. Equation (5.43) demonstrates that PFGs allow to investigate the diagonal elements of the diffusion tensor. To obtain also the off-diagonal elements, it is necessary to observe the off-diagonal directions

as linear combinations of the PFGs. If for instance PFGs in x and y direction are simultaneously applied, the NMR signal intensity is

$$S(t) = S(0) \exp\left\{-(b_{xx}D_{xx} + b_{yy}D_{yy} + 2\,b_{xy}D_{xy})\right\}. \tag{5.44}$$

The coupling of an off-diagonal element with diagonal elements in this equation prohibits the extraction of all three elements using the signal at different PFG magnitudes. Instead, six diffusion experiments at different PFG directions are required to solve the system of six coupled equations.

5.3.3. The stimulated echo pulse sequence combined with imaging

Beside MRI with spin echo multi slice imaging, it is also common to work with stimulated echo MRI, especially if T_2 is short. A typical spin echo MRI sequence is shown in Figure 5.11.

As outlined above in Chapter 5.1.4, the major advantage of the stimulated echo pulse sequence is the opportunity to store the magnetization in z direction during Δ' and avoid signal loss due to T_2 relaxation. Instead of exciting the entire sample with hard 90° pulses, one or two soft pulses are used in imaging for slice selective excitation. In practice it is sufficient, if the third 90° pulse is soft. This pulse sequence requires that the storage interval Δ' is much longer than T_2 relaxation. In that way, no spins remain in the xy plane from the first or second 90° pulse that would generate additional echoes during the recording of the NMR signal.

In the stimulated echo imaging pulse sequence presented in Figure 5.11 not only the third but also the first 90° pulse is a slice selective soft pulse. The second rf pulse is hard and excites the entire sample. This pulse sequence is only one possible combination of rf pulses following the previous discussion. Water in natural sand, as investigated in this thesis, has a much smaller T_2 relaxation time [SPB09] than Δ' and made this combination of hard and soft rf pulses acceptable. The slice selective field gradients, applied in the pulse sequence scheme in z direction, are similarly refocused as described by the spin echo imaging pulse sequence in Chapter 5.3.1. Spatial resolution in the selected slice is obtained by read out and phase-encoding field gradients applied in x and y direction, respectively. In this pulse sequence exemplary both gradients are implemented after the last 90° pulse.

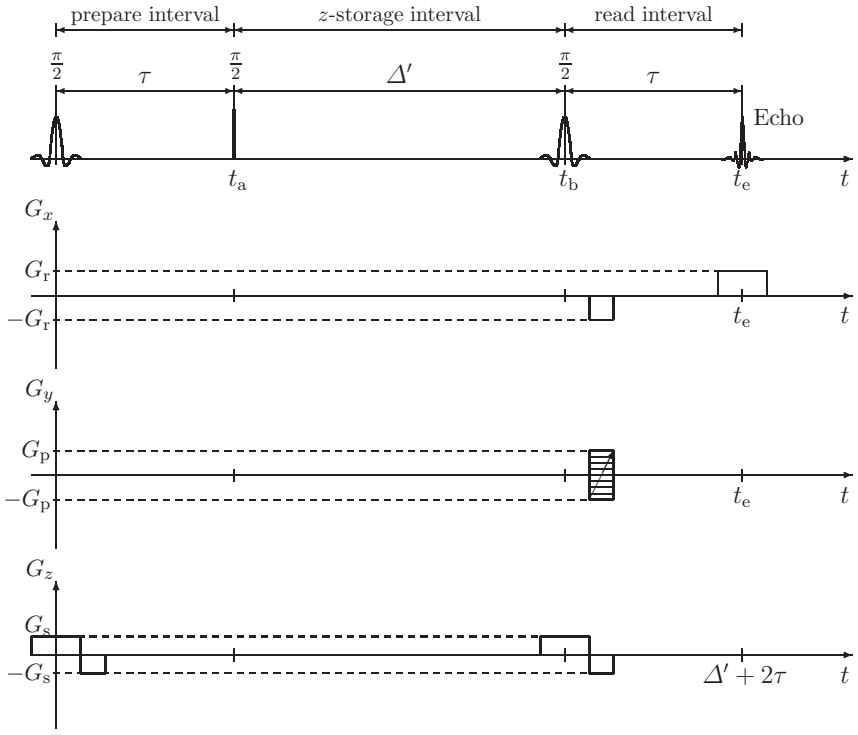

Figure 5.11: *Stimulated echo pulse sequence with a combination of hard and soft rf pulses for samples where T_2 is much shorter than the storage time Δ'. Imaging field gradients are applied for read out (G_r, applied in x direction), phase-encoding (G_p, applied in y direction) and slice selection (G_s, applied in z direction).*

Since no 180° pulse between the two read out gradients inverts the spin dephasing during the first gradient, the gradients have to have opposite signs.

5.3.4. NMR velocity imaging

A further topic of this thesis are flow measurements combined with imaging on natural porous media. Thereby, applied water flow through natural sand was investigated. Until now, NMR signals were only discussed on self-diffusing water molecules without externally forced water flow. This chapter takes the simultaneous influence of diffusion and flow on the NMR signal into account. Therefore, the Bloch-Torrey equations (Eq. (5.4)) have to be extended by the additional term $\nabla \boldsymbol{v}\boldsymbol{M}$, with $\boldsymbol{v}$

being the velocity of the observed molecules,

$$\frac{\partial \boldsymbol{M}(\boldsymbol{r},t)}{\partial t} = \gamma \boldsymbol{M} \times \boldsymbol{B} - \frac{M_x \boldsymbol{e}_x + M_y \boldsymbol{e}_y}{T_2} - \frac{M_z - M_0}{T_1}\,\boldsymbol{e}_z + \nabla \mathbf{D} \nabla \boldsymbol{M} + \nabla \boldsymbol{v} \boldsymbol{M}. \tag{5.45}$$

In the following, isotropic diffusion is assumed. Then Eq. (5.28) becomes

$$\frac{\partial \mathcal{M}(\boldsymbol{r},t)}{\partial t} = \left[\mathrm{i}\,\gamma B_z(\boldsymbol{r},t) - \frac{1}{T_2} + D\nabla^2 - \nabla \boldsymbol{v} \right] \mathcal{M}(\boldsymbol{r},t). \tag{5.46}$$

This equation can again be solved with the approach of Eq. (5.29),

$$\mathcal{M}(\boldsymbol{r},t) = S(t) \exp\left\{ -\frac{t}{T_2} - \mathrm{i}\,\gamma\,\boldsymbol{r} \int_0^t \mathrm{d}t' \left[\boldsymbol{G}^*(t') + \boldsymbol{g}^*(t') \right] \right\}, \tag{5.47}$$

with effective PFG $\boldsymbol{G}^*(t)$ and effective internal field gradients $\boldsymbol{g}^*(t)$. According to Eq. (5.10) by inserting Eq. (5.47) in Eq. (5.46) this leads to the differential equation for the detectable NMR signal,

$$\frac{\mathrm{d}S(t)}{\mathrm{d}t} = -S(t) D \left[\gamma \int_0^t \mathrm{d}t' \left[\boldsymbol{G}^*(t') + \boldsymbol{g}^*(t') \right] \right]^2 \tag{5.48}$$

with the solution

$$\begin{aligned} S(t) = S(0) \exp\left\{ -D\gamma^2 \int_0^t \mathrm{d}t' \left[\int_0^{t'} \mathrm{d}t'' \left[\boldsymbol{G}^*(t'') + \boldsymbol{g}^*(t'') \right] \right]^2 \right\} \\ \cdot \exp\left\{ \mathrm{i}\,\gamma\,\boldsymbol{v} \int_0^t \mathrm{d}t' \left[\int_0^{t'} \mathrm{d}t'' \left[\boldsymbol{G}^*(t'') + \boldsymbol{g}^*(t'') \right] \right] \right\}. \end{aligned} \tag{5.49}$$

Analog to Eq. (5.17), diffusion can be considered also for the velocity depending part in Eq. (5.49):

$$S(t) = S(0) \exp\left\{ -D\gamma^2 \left[A_\mathrm{p}(t) + A_\mathrm{c}(t) + A_\mathrm{i}(t) \right] \right\} \exp\left\{ \mathrm{i}\,\gamma\,\boldsymbol{v} \left[\boldsymbol{B}_\mathrm{p}(t) + \boldsymbol{B}_\mathrm{i}(t) \right] \right\}, \tag{5.50}$$

whereby

$$\boldsymbol{B}_{\mathrm{p}}(t) = \int_0^t \mathrm{d}t' \left[\int_0^{t'} \mathrm{d}t'' \, \boldsymbol{G}^*(t'') \right], \tag{5.50a}$$

$$\boldsymbol{B}_{\mathrm{i}}(t) = \int_0^t \mathrm{d}t' \left[\int_0^{t'} \mathrm{d}t'' \, \boldsymbol{g}^*(t'') \right]. \tag{5.50b}$$

$\boldsymbol{B}_{\mathrm{p}}(t)$ and $\boldsymbol{B}_{\mathrm{i}}(t)$ describe the influence of effective applied field gradients and the effective internal field gradients on the detectable NMR signal. There appears no cross term in the imaginary part of Eq. (5.50) in contrast to Eq. (5.17). In the case of anisotropic diffusion, the double integral of the diffusional part (first exponential function) of Eq. (5.49) has to be replaced by the general expression Eq. (5.30). Equation (5.50) shows that diffusion and flow act differently on the NMR signal. Water diffusion attenuates the signal exponentially. Instead, applied flow shifts the phase of the magnetization by

$$\phi(t) = \gamma \, \boldsymbol{v} \int_0^t \mathrm{d}t' \left[\int_0^{t'} \mathrm{d}t'' \, [\boldsymbol{G}^*(t'') + \boldsymbol{g}^*(t'')] \right] = \phi_{\boldsymbol{G}^*}(t) + \phi_{\boldsymbol{g}^*}(t). \tag{5.51}$$

Thereby, the phase shift can be split in one part $\phi_{\boldsymbol{G}^*}(t)$ influenced by PFGs, and a second part $\phi_{\boldsymbol{g}^*}(t)$ influenced by internal field gradients. Velocity NMR is based on different applied PFGs, varying $\boldsymbol{G}(t)$ in amplitude or duration, while the influence of $\boldsymbol{g}^*(t)$ stays constant. Applying two PFGs at different amplitudes $\boldsymbol{G}_1(t)$ and $\boldsymbol{G}_2(t)$ results in a net phase shift of

$$\begin{aligned} \Delta\phi(t) &= \phi_2(t) - \phi_1(t) \\ &= [\phi_{\boldsymbol{G}_2^*}(t) + \phi_{\boldsymbol{g}^*}(t)] - [\phi_{\boldsymbol{G}_1^*}(t) + \phi_{\boldsymbol{g}^*}(t)] = \phi_{\boldsymbol{G}_2^*}(t) - \phi_{\boldsymbol{G}_1^*}(t). \end{aligned} \tag{5.52}$$

Equation (5.52) shows that the influence of constant internal field gradients vanishes.

The phase shift of the NMR signal under applied flow is only governed by well known PFGs. This allows the determination of velocities by analyzing the phase shift $\Delta\phi(t)$ depending on the PFG difference $\Delta\boldsymbol{G}(t)$:

$$\Delta\phi(t) = \gamma\,\boldsymbol{v}\int_0^t \mathrm{d}t'\left[\int_0^{t'}\mathrm{d}t''\Delta\boldsymbol{G}^*(t'')\right]. \tag{5.53}$$

This is the basic equation for flow velocity NMR.

As shown in Eq. (5.52) internal field gradients do not influence the net phase shift of the NMR signal. However, they still influence the signal amplitude due to their diffusive effect. Chapter 6.2 discusses how to reduce the influence of internal field gradients.

A stimulated echo imaging pulse sequence used for flow velocity imaging is shown in Figure 5.12.

Basis of this sequence is the stimulated echo imaging pulse sequence of Figure 5.11. Slice selection is applied in z direction, the read out gradients are applied in x direction, and phase-encoding is applied in y direction. PFGs (red in Figure 5.12) for flow-encoding are commonly applied in one single direction. Without loss of generality, x direction was exemplarily chosen in Figure 5.12.

Flow-encoding measurements are based on the phase shift $\Delta\phi(t)$ of the detected NMR signal. According to Eq. (5.53), for $\boldsymbol{G}$ as in Figure 5.12 the phase shift becomes

$$\Delta\phi(t_\mathrm{e}) = \gamma\delta\Delta\boldsymbol{v}\cdot\Delta\boldsymbol{G} \tag{5.54}$$

at $t_\mathrm{e} = \Delta' + 2\tau$. Note that $\boldsymbol{v}$ is constant in the entire discussion. For each pixel in the image, the velocity of the molecules can be calculated as:

$$\boldsymbol{v} = \frac{\Delta\phi(t_\mathrm{e})}{\gamma\delta\Delta|\Delta\boldsymbol{G}|}\cdot\frac{\Delta\boldsymbol{G}}{|\Delta\boldsymbol{G}|}. \tag{5.55}$$

This allows to plot two-dimensional maps of the spatially resolved velocity distribution depending on the direction of the applied field gradient $\boldsymbol{G}$. Thus, performing three experiments with varying $\boldsymbol{G}$ pointing to x, y and z allow to construct the full velocity vector $\boldsymbol{v}$ in each pixel of the sample image.

For velocity imaging with a pulse sequence such as shown in Figure 5.12, the imaging field gradients are applied independently of flow-encoding PFGs. Thus,

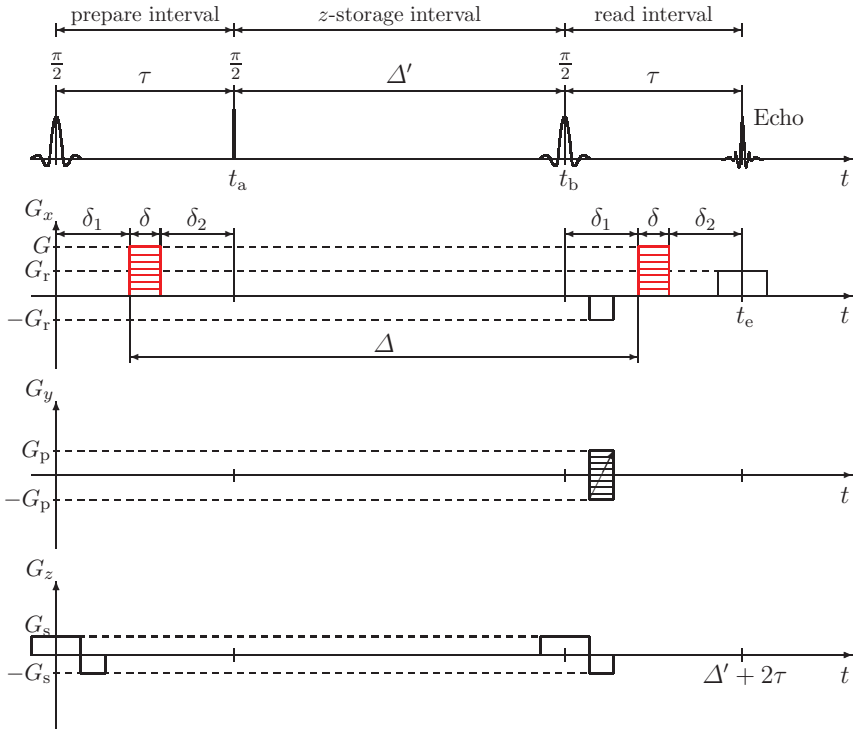

Figure 5.12: *Principle of velocity imaging based on a stimulated echo pulse sequence (Chapter 5.3.3). PFGs for flow-encoding (red color) can also be applied in y and z direction of the laboratory coordinate system.*

the entire $\boldsymbol{k}$-space is mapped, while the flow-encoding PFGs stay constant. After recording the images, the PFGs are changed according to flow-encoding, and again the entire $\boldsymbol{k}$-space is mapped.

6. Pulse sequences – further developments

One outcome of this thesis are developments and improvements of NMR pulse sequences for the application to natural porous media. Especially for NMR measurements on natural soil and sand the problem of short T_2 relaxation times as well as influences of internal field gradients were faced by pulse sequence improvements. For diffusion diffusion correlation spectroscopy a new way of determining maps of diffusion coefficient distributions was found. Major advances have been achieved in the reduction of the influence of internal field gradients on the NMR signal in velocity mapping.

6.1. Improvements of DDCOSY

The DDCOSY pulse sequence introduced in Chapter 5.2 allows to investigate the anisotropy of samples both on the macroscopic and on the microscopic scale. However, natural porous media often have short T_2 relaxation times and are influenced by internal field gradients. In this work the common DDCOSY pulse sequence was optimized for the investigation of natural porous media by shortening the timing and suppressing the cross term.

6.1.1. Shortening of DDCOSY to sDDCOSY

With the pulse sequence DDCOSY [CF04, CGR03], T_2 relaxation can occur in a total time interval of 4τ with typically $\tau \approx 2\,\mathrm{ms}$. Another shortcoming of the DDCOSY pulse sequence is the possibility of diffusion in internal field gradients. Both problems are addressed in the following.

First, the time duration given to the spins to relax according to the T_2 process was reduced. Thereby, the common pulse sequence DDCOSY had to be shortened,

while still revealing the same information about isotropy. Starting point was DDCOSY including two independent pairs of PFGs. The amplitude of the gradients $\boldsymbol{q}_1$ and $\boldsymbol{q}_2$ have q_1 and q_2 steps, respectively. Figure 6.1 shows the scheme of the shortened DDCOSY pulse sequence, which is called sDDCOSY (short DDCOSY) in the following.

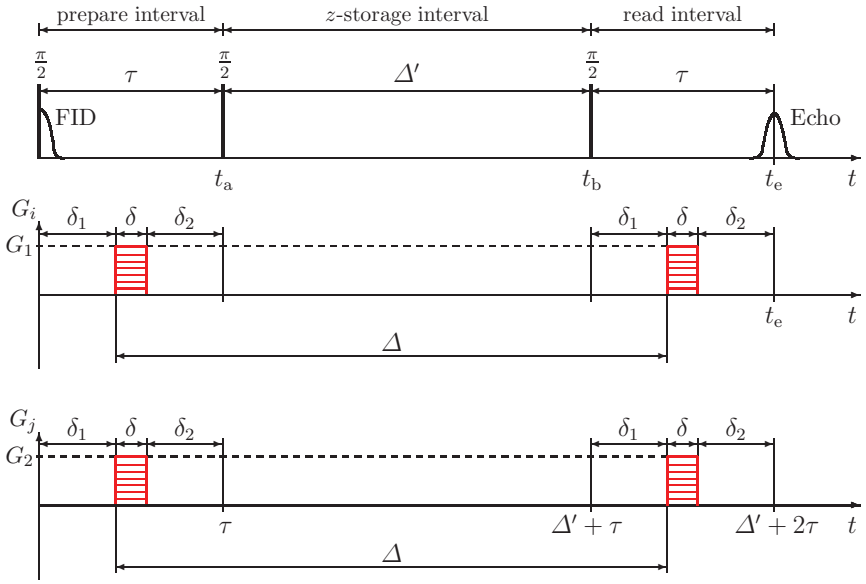

Figure 6.1: *Shortened diffusion diffusion correlation spectroscopy pulse sequence (sDDCOSY) based on the stimulated echo pulse sequence. In contrast to the common DDCOSY pulse sequence, here the PFG pairs in different observation directions are applied simultaneously. Thereby, the signal can be recorded after half the time compared to DDCOSY. There is less influence of T_2 relaxation on the NMR signal, so this pulse sequence is suited for samples with short T_2 relaxation time. G_i and G_j represent any perturbation of x, y and z in the laboratory coordinate system.*

In contrast to DDCOSY, the PFG pairs are now not applied subsequently, separated by some time interval. Instead, the PFG pairs are applied simultaneously in different, perpendicular directions. The amplitude of the first PFG pair in direction $\boldsymbol{q}_1$ is increased stepwise in q_1 steps while the amplitude of the second PFG pair $\boldsymbol{q}_2$ stays constant. As all q_1 steps have been finished, the amplitude of $\boldsymbol{q}_2$ is increased. This process is iterated until all q_2 steps are finished.

Note that this pulse sequence is identically to a two-dimensional PFG stimulated echo pulse sequence, where PFGs are applied simultaneously in two different directions [Blu05, MHS99, ST65]. The distribution of mean displacements at self-diffusion is symmetric around zero. Thus, negative PFGs result in the same displacement than positive PFGs, despite the different sign. It is therefore sufficient to apply only positive PFGs. This reduces the measurement time by a factor of two.

The expected NMR signal can be calculated similar to Eq. (5.40). Since in the sDDCOSY pulse sequence both PFGs $\boldsymbol{q}_1$ and $\boldsymbol{q}_2$ are applied at the same time, the resulting operating PFG $\boldsymbol{q}$ is the sum of both vectors,

$$\boldsymbol{q} = \boldsymbol{q}_1 + \boldsymbol{q}_2. \tag{6.1}$$

Therefore, Eq. (5.40) becomes for the sDDCOSY pulse sequence

$$\begin{aligned} S(t_\mathrm{e}) &= S(0) \exp\left\{-4\pi\Delta\, \boldsymbol{q}^\mathrm{T}\, \mathbf{D}\, \boldsymbol{q}\right\} = S(0) \exp\left\{-4\pi\Delta\, [\boldsymbol{q}_1^\mathrm{T} + \boldsymbol{q}_2^\mathrm{T}]\, \mathbf{D}\, [\boldsymbol{q}_1 + \boldsymbol{q}_2]\right\} = \\ &= S(0) \exp\left\{-4\pi\Delta \left(\boldsymbol{q}_1^\mathrm{T}\, \mathbf{D}\, \boldsymbol{q}_1 + \boldsymbol{q}_2^\mathrm{T}\, \mathbf{D}\, \boldsymbol{q}_2 + \boldsymbol{q}_1^\mathrm{T}\, \mathbf{D}\, \boldsymbol{q}_2 + \boldsymbol{q}_2^\mathrm{T}\, \mathbf{D}\, \boldsymbol{q}_1\right)\right\}. \end{aligned} \tag{6.2}$$

The first two terms of the second line in Eq. (6.2) are identical with Eq. (5.40). These products with identical vectors $\boldsymbol{q}_i^\mathrm{T}\, \mathbf{D}\, \boldsymbol{q}_i$ contain the influence of a diagonal diffusion coefficient D_{ii} on the NMR signal. However, the mixing terms $\boldsymbol{q}_1^\mathrm{T}\, \mathbf{D}\, \boldsymbol{q}_2$ and $\boldsymbol{q}_2^\mathrm{T}\, \mathbf{D}\, \boldsymbol{q}_1$ in Eq. (6.2) give additional information about the diffusion behavior of the sample. The mixing terms select the off-diagonal diffusion coefficient D_{ij}, $i \neq j$. In general, the detectable NMR signal is influenced by both diagonal and off-diagonal coefficients of the diffusion tensor. Note that for isotropic samples with vanishing off-diagonal coefficients, the mixing terms are zero.

The timing of this sDDCOSY pulse sequence in Figure 6.1 is equal to the 1D PFG stimulated echo pulse sequence presented in Chapter 5.1.5 and Figure 5.5. Therefore, the duration of sDDCOSY is reduced to half the duration of the common DDCOSY pulse sequence. This results in a significant increase of signal intensity. Both the time intervals for T_1 and T_2 relaxation are reduced by half. Especially for samples such as natural soil and sand with short T_2 relaxation times the improvement is remarkable, since the time affects in the exponent of the exponential function in Eq. (4.11). For a typical value of $\tau \approx 2\,\mathrm{ms}$, the T_2 relaxation period is reduced from 8 ms to 4 ms. With $T_2 = 20\,\mathrm{ms}$ as found by Stingaciu et al. [SPB09], the NMR signal increases by $\approx 25\,\%$ using sDDCOSY.

With the PFGs shown in Figure 6.1 as effective gradients, the signal attenuation resulting from the pulse sequence timing according to Eq. (5.31) is given by

$$A'_{\mathrm{p}} = \delta^2 \left(\Delta - \tfrac{1}{3}\delta\right), \tag{6.3a}$$

$$A'_{\mathrm{c}} = \delta \left[2\tau(\Delta' + \tau) - \tfrac{2}{3}\delta^2 - (\delta_1^2 + \delta_2^2) - \delta(\delta_1 + \delta_2)\right], \tag{6.3b}$$

$$A'_{\mathrm{i}} = \tau^2(\Delta' + \tfrac{2}{3}\tau). \tag{6.3c}$$

Compared to Eq. (5.41), the simultaneous application of the PFG pairs in sDDCOSY reduces the influence of internal field gradients by a factor of 2. This is the second effect how sDDCOSY improves the NMR signal. Overall, sDDCOSY results in a significant gain of signal intensity.

With Eq. (6.2) the sDDCOSY pulse sequence becomes similar to the concept of diffusion tensor imaging (DTI), except the missing imaging part in sDDCOSY. With the sDDCOSY pulse sequence it is not possible to obtain a two-dimensional data set with two pairs of PFGs applied in the same direction, $\boldsymbol{q}_i = \boldsymbol{q}_j$. This choice of PFG direction only results in a one-dimensional data set showing the signal decay according to D_{ii} with increasing PFG amplitudes. Therefore, PFGs are most usefully applied in the three perpendicular directions D_x and D_y, D_x and D_z, as well as D_y and D_z. One-dimensional measurements are necessary for determining the diagonal diffusion coefficients. The 2D maps obtained with sDDCOSY show both the influence of the diagonal as well as of the off-diagonal diffusion coefficients. A macroscopic and isotropic sample shows only diagonal peaks in the 2D map, resulting from the diagonal diffusion tensor elements. Therefore, the first test of sDDCOSY in this work took place on an isotropic sample of natural sand.

In further experimental and theoretical studies on sDDCOSY it is necessary to investigate the influence of off-diagonal diffusion tensor elements on the 2D diffusion correlation maps. These maps enable to determine full diffusion tensors for different systems. Diagonalization of the tensors gives the preferred diffusion directions similar to DTI. In contrast, the common DDCOSY pulse sequence considers only diffusion along axes in the laboratory coordinate system. If diffusion in an anisotropic sample points in an arbitrary direction, DDCOSY only detects the projection of the diffusion tensor on the axes of the laboratory coordinate system. The actual diffusion behavior is not obtained reliably. Therefore, sDDCOSY is a powerful and promising pulse sequence not only for samples showing short T_2 relaxation time.

6.1.2. sDDCOSY with cross term suppression

The shortening of the DDCOSY to the sDDCOSY pulse sequence reduced the influence of T_2 relaxation on the NMR signal. Therefore, the pulse sequence sDDCOSY allows to investigate diffusion correlations between different spatial directions. However, sDDCOSY measurements on natural porous media such as soil and sand will still show influences from internal field gradients. This results in the cross term A'_{c}, which combines PFGs and internal gradients, and the term A'_{i} coming from internal gradients, both described in Eq. (6.3). Reducing these influences leads to the idea of combining sDDCOSY with the 13-interval concept of Cotts et al. [CHS89] as presented in Chapter 5.1.6. Together with an appropriate timing of the pulse sequence, this allows the suppression of the cross term. The combined pulse sequence is named 13-interval sDDCOSY and a possible scheme of this pulse sequence shows Figure 6.2.

In total two additional 180° pulses are applied compared to sDDCOSY: the first one between the first and second 90° pulse, and the second one between the third 90° pulse and the recorded NMR echo.

The signal attenuation resulting from the pulse sequence timing according to Eq. (5.31) for the 13-interval sDDCOSY pulse sequence is determined by

$$A'_{\mathrm{p}} = \delta^2 \left[4(\Delta' + \tau) + 2\tau - \tfrac{2}{3}\delta\right], \tag{6.4a}$$

$$A'_{\mathrm{c}} = 2\delta\tau(\delta_1 - \delta_2), \tag{6.4b}$$

$$A'_{\mathrm{i}} = \tfrac{4}{3}\tau^3. \tag{6.4c}$$

The reduction or even suppression of cross term influences on the NMR signal with 13-interval sDDCOSY allows now to map diffusion coefficient correlations of samples strongly influenced by internal field gradients. Choosing $\delta_1 = \delta_2$ leads to a full suppression of the cross term A'_{c} in Eq. (6.4). Therefore, the NMR signal is further improved even beyond the effect sDDCOSY had shown.

13-interval sDDCOSY opens an entire new research field. In this thesis, measurements on an isotropic sample of natural sand are presented. Similar to sDDCOSY, further investigations as well as mathematical work are needed. Also with 13-interval sDDCOSY it might be possible to obtain entire diffusion tensors as described above for sDDCOSY.

In summary, the 13-interval sDDCOSY pulse sequence allows correlation mea-

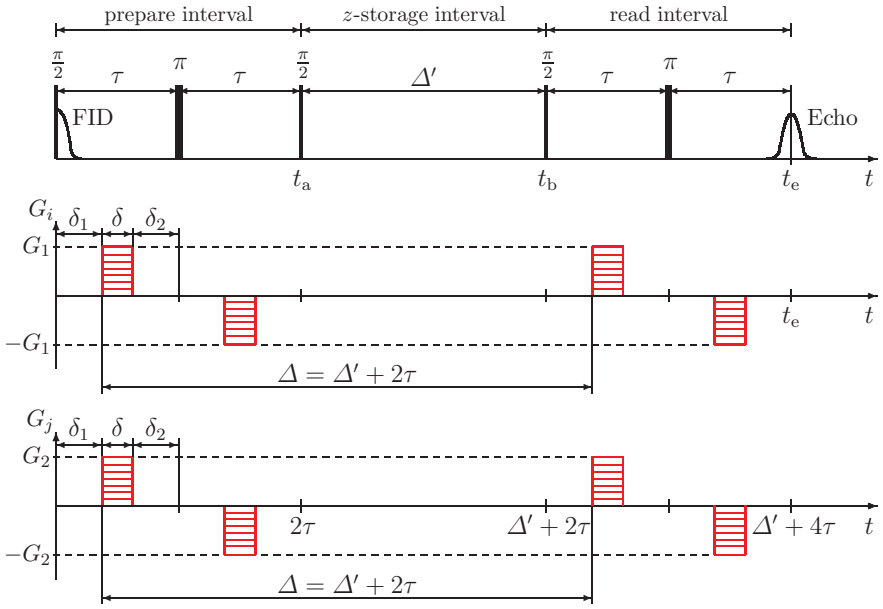

Figure 6.2: *Shortened diffusion diffusion correlation spectroscopy pulse sequence combined with the 13-interval concept of Cotts et al. [CHS89], which is called 13-interval sDDCOSY. With the implemented 13-interval pulse sequence it is possible to reduce or even to suppress the cross term of pulsed and internal field gradients. G_i and G_j represent any perturbation of x, y and z in the laboratory coordinate system.*

surements of different diffusion coefficients on samples with both short T_2 relaxation time and strong influences of internal field gradients on the NMR signal.

6.2. 13-interval STEMSI for flow in natural porous media

As already discussed in Chapter 5.3.4, the determination of velocities with NMR relays on a phase shift $\Delta\phi$(t) of the NMR signal instead of signal attenuation. The phase shift depends on the velocity of the molecules and on field gradients according to Eq. (5.50). In contrast to the diffusive part (Eq. (5.11)) there is no quadratic time integral over the sum of pulsed and internal field gradients. This means that the phase shift is not influenced by a cross term $A_c(t_e)$ (Eq. (5.17b)). In Chapter 5.3.4

it was already discussed (Eq. (5.52)) that internal field gradients have no influence on the flow velocity determination. The only influence of internal field gradients on the NMR signal results from the terms $A_c(t_e)$ and $A_i(t_e)$ according to the first exponential part of Eq. (5.50). Therefore, in low signal to noise environments, it is recommended to use a 13-interval pulse sequence as introduced by Cotts et al. [CHS89] to suppress the cross term $A_c(t_e)$.

For measurement of low flow velocities in natural porous media presented in this thesis, flow-encoding imaging was combined with the 13-interval pulse sequence (Chapter 5.1.6) acting as a filter. In the following, the combined pulse sequence is named 13-interval stimulated echo multi slice imaging (13-interval STEMSI) and is shown in Figure 6.3.

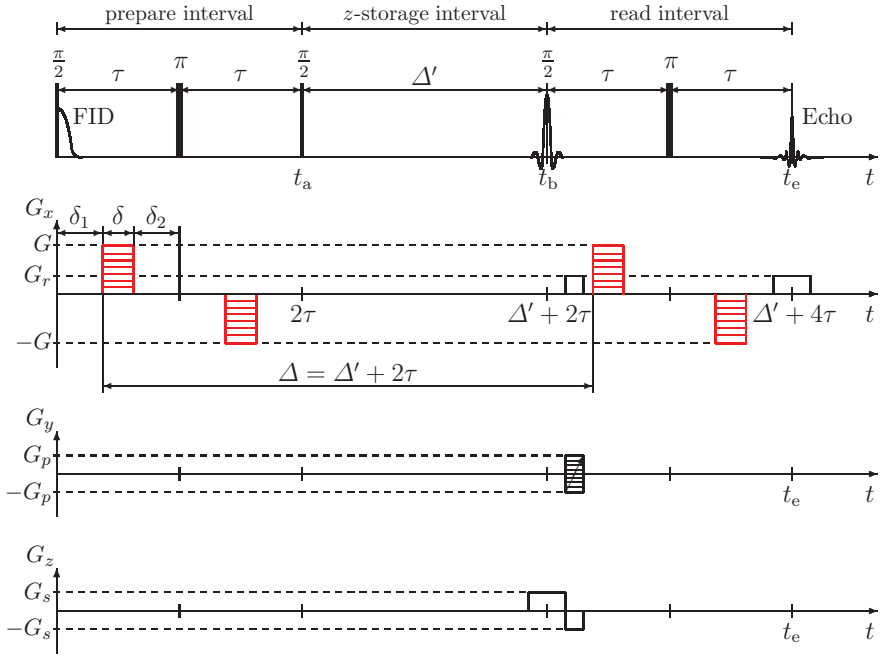

Figure 6.3: *Combined 13-interval pulse sequence with multi slice imaging, 13-interval STEMSI, for velocity imaging. Imaging field gradients are applied for read out (G_r, in this scheme of the pulse sequence applied in x direction), phase-encoding (G_p, applied in y direction) and slice selection (G_s, applied in z direction). Note that the PFGs (red color) can also be applied in y and z direction.*

The parts of the combined pulse sequence are color coded in the figure. Stimulated

echo multi slice velocity imaging contains the black gradient pulses (Chapter 5.3.4) and the 13-interval PFG pulse sequence contains the red gradient pulses (Chapter 5.1.6). The imaging part of this pulse sequence is similar to stimulated echo imaging (Chapter 5.3.3). An improvement in 13-interval STEMSI is an initial hard 90° pulse for excitation instead of a soft pulse. This allows shortened time intervals τ in the range of $\tau \approx 2\,\mathrm{ms}$, which are not possible with soft pulses with typical pulse durations of already around 1 ms. As discussed in Chapter 5.3.3 there is no difference whether a hard or soft (slice selective) initial 90° pulse is applied since the storage time Δ' was chosen much longer than T_2 relaxation. It was checked in several experiments while developing this pulse sequence that no additional NMR signal results from the first three rf pulses. The 90° pulse after the storage interval is still a soft pulse for slice selective imaging. This pulse is combined with a slice selective gradient pulse applied in z direction in Figure 6.3. The phase-encoding and read out imaging field gradients were applied in x and y direction, respectively.

The 13-interval STEMSI pulse sequence contains two pairs of bipolar PFGs $\boldsymbol{G}$ with amplitude $G = |\boldsymbol{G}|$ and duration δ. The observation time Δ is defined from the beginning of the first gradient pulse in the prepare interval at $t = \delta_1$ to the beginning of the first gradient pulse in the read interval at $t = \Delta' + 2\delta_1$. Note that the flow-encoding by PFGs can also be applied in y and z direction. This was used to identify the velocity detection limit of this pulse sequence.

To suppress cross term influences on the NMR signal, all four PFGs are centered between 90° and 180° pulses such that $\delta_1 = \delta_2$. Under this condition the cross term becomes zero (Eq. (5.26b)).

During the storage time interval Δ' the magnetization is stored in the longitudinal direction, only influenced by T_1 relaxation. Internal field gradients and T_2 relaxation can only affect the NMR signal during the τ intervals in the prepare and the read intervals.

7. Techniques of NMR data evaluation

The NMR data analysis of the experiments presented in this thesis are based on conventional methods as well as on new developments. The two-dimensional experiments, pure NMR imaging, and velocity imaging were analyzed with common evaluation methods. However, for DTI measurements despite the common method another way of data evaluation is described in this chapter and validated by model calculations.

7.1. Methods currently known

In this chapter the commonly used methods for data analysis of NMR measurements as performed in this work are described.

7.1.1. DDCOSY: Inverse Laplace transformation

Inferring diffusion coefficient distributions from DDCOSY measurements is based on the inverse Laplace transform [SVH02],

$$\mathbf{M}(\tau_1, \tau_2) = \int \mathrm{d}x\, \mathrm{d}y\, k_1(x, \tau_1)\, k_2(y, \tau_2)\, \mathcal{F}(x, y) + \mathbf{E}(\tau_1, \tau_2), \tag{7.1}$$

of the two-dimensional NMR signal array $\mathbf{M}(\tau_1, \tau_2)$. The integrand $k_1(x, \tau_1)\, k_2(y, \tau_2)$ relates the desired parameters x, y with the measurement parameters τ_1, τ_2. The function $\mathcal{F}(x, y)$ represents the probability density of x and y, therefore $\mathcal{F}(x, y) \geq 0$. $\mathbf{E}(\tau_1, \tau_2)$ represents the experimental noise.

The inverse Laplace transformation is applied on DDCOSY results by means of the **b**-matrix (Eq. (5.34)). Thus, $\boldsymbol{q}_1$ and $\boldsymbol{q}_2$ are represented in $b_{ij,\,1}$ and $b_{ij,\,2}$ of the **b**-matrix, respectively. With that, the inverse Laplace transformation of Eq. (7.1)

applied to DDCOSY becomes

$$\mathbf{S}(b_{ij,1}, b_{ij,2}) = \int \mathrm{d}D_{ij,1}\,\mathrm{d}D_{ij,2}\exp\Big\{-\sum_{i,j=x,y,z}[b_{ij,1}D_{ij,1} + b_{ij,2}D_{ij,2}]\Big\}\mathcal{F}(D_{ij,1}, D_{ij,2}) + \mathbf{E}(b_{ij,1}, b_{ij,2}) \tag{7.2}$$

The distribution of the diffusion coefficients $\mathcal{F}(D_{ij,1}, D_{ij,2})$ measured with DDCOSY can now be determined from Eq. (7.2) as described by Song et al. [SVH02] using Tychonoff's theorem. The two-dimensional plots of the distribution give information about isotropy or anisotropic behavior.

7.1.2. MRI and velocity imaging: Fourier transformation

The application of Fourier transformation to determine spatially resolved images from the temporal NMR signal was introduced in Chapter 4.2.3.

The general definition of the Fourier transform is

$$f(y) = \int_{-\infty}^{+\infty} \mathrm{d}x f(x)\exp\{2\pi\,\mathrm{i}\,xy\}. \tag{7.3}$$

Also in velocity imaging a Fourier transformation was used to obtain the displacement of the molecules and with that the velocity of each pixel. The signal is obtained from the Fourier transformation of the propagator $P(\boldsymbol{R}, \Delta)$ (Eq. (3.6)) describing the molecular displacement. Furthermore, the signal depends on the PFG parameters $\boldsymbol{q}$. For simplification in the following the molecular displacement is named $\boldsymbol{R} = \boldsymbol{r} - \boldsymbol{r}_0$. Thus, the Fourier transform becomes

$$S(\boldsymbol{q}) = \int \mathrm{d}\boldsymbol{R}\,P(\boldsymbol{R}, \Delta)\exp\{\mathrm{i}\,2\pi\boldsymbol{q}\cdot\boldsymbol{R}\}. \tag{7.4}$$

The velocity is calculated by dividing the mean displacement by the observation time, $\boldsymbol{v} = \boldsymbol{R}/\Delta$, representing the phase shift of the signal as expressed in Eq. (5.54). In the end, two-dimensional maps of the sample with the propagator $P(\boldsymbol{R}, \Delta)$ are obtained.

7.1.3. DTI: Moore-Penrose pseudoinverse matrix for tensor determination

As derived in Chapter 5.3.2, measurements in different PFG directions are necessary to determine the diffusion tensor of each pixel. Each detected MRI slice was Fourier transformed. Noise disturbing the NMR signal was suppressed by creating a mask from the NMR measurements without PFGs. These masks were overlayed creating the total mask. According to Eq. (5.42) at least six independent NMR imaging experiments with diffusion-encoding have to be performed. Due to the symmetry of the diffusion tensor (see Chapter 3.2) PFGs have to be applied only in the following six instead of nine directions:

$$\boldsymbol{G_{xx}} \equiv (G,0,0)^{\mathrm{T}}, \tag{7.5a}$$
$$\boldsymbol{G_{yy}} \equiv (0,G,0)^{\mathrm{T}}, \tag{7.5b}$$
$$\boldsymbol{G_{zz}} \equiv (0,0,G)^{\mathrm{T}}, \tag{7.5c}$$
$$\boldsymbol{G_{xy}} \equiv \boldsymbol{G_{xx}} + \boldsymbol{G_{yy}} = (G,G,0)^{\mathrm{T}}, \tag{7.5d}$$
$$\boldsymbol{G_{xz}} \equiv \boldsymbol{G_{xx}} + \boldsymbol{G_{zz}} = (G,0,G)^{\mathrm{T}}, \tag{7.5e}$$
$$\boldsymbol{G_{yz}} \equiv \boldsymbol{G_{yy}} + \boldsymbol{G_{zz}} = (0,G,G)^{\mathrm{T}}. \tag{7.5f}$$

Applying all of the PFG pairs defined in Eq. (7.5) leads to six equations for the NMR signal:

$$\boldsymbol{G_{xx}}: \quad \ln\tfrac{S(t_e)}{S(0)} = -\left[b_{xx}D_{xx}\right], \tag{7.6a}$$
$$\boldsymbol{G_{yy}}: \quad \ln\tfrac{S(t_e)}{S(0)} = -\left[b_{yy}D_{yy}\right], \tag{7.6b}$$
$$\boldsymbol{G_{zz}}: \quad \ln\tfrac{S(t_e)}{S(0)} = -\left[b_{zz}D_{zz}\right], \tag{7.6c}$$
$$\boldsymbol{G_{xy}}: \quad \ln\tfrac{S(t_e)}{S(0)} = -\left[b_{xx}D_{xx} + b_{yy}D_{yy} + 2\,b_{xy}D_{xy}\right], \tag{7.6d}$$
$$\boldsymbol{G_{xz}}: \quad \ln\tfrac{S(t_e)}{S(0)} = -\left[b_{xx}D_{xx} + b_{zz}D_{zz} + 2\,b_{xz}D_{xz}\right], \tag{7.6e}$$
$$\boldsymbol{G_{yz}}: \quad \ln\tfrac{S(t_e)}{S(0)} = -\left[b_{yy}D_{yy} + b_{zz}D_{zz} + 2\,b_{yz}D_{yz}\right]. \tag{7.6f}$$

The NMR signal resulting from $\boldsymbol{G_{xx}}$ is named $s(b_{xx}) \equiv \frac{S(t_e)}{S(0)}$ in the following. The other five directions are abbreviated accordingly. Since the off-diagonal elements of a diffusion tensor do not vanish in general, the signal attenuation depends also on the mixed terms. For instance, $b_{ij}D_{ij}$ with $i \neq j$ appears together with $b_{ii}D_{ii}$ and $b_{jj}D_{jj}$ [LMP01]. To improve fitting in the presence of noise, diffusion encoded MRI

measurements are performed at d different PFG amplitudes. The amplitudes are succeedingly increased up to a maximum gradient strength of $G_{\max}$. The recorded NMR signals can be combined in a d-dimensional vector. In a general notation for all six gradient directions, this is

$$\boldsymbol{s_{ij}}(b_{ij}) = (s_1(b_{ij}),\, s_2(b_{ij}), \ldots,\, s_d(b_{ij}))^{\mathrm{T}} \quad \text{with} \quad i,j = x,y,z, \tag{7.7}$$

where $s_1(b_{ij})$, $s_2(b_{ij}), \ldots,$ $s_d(b_{ij})$ are the d different NMR signals. The d different PFG amplitudes result also in different **b**-matrices. For easier treatment, these different **b**-matrices can be combined to a single matrix $\mathbf{b_{ij}}$, depending of the gradient pulse directions. In $\mathbf{b_{ij}}$, the six elements of the symmetric **b**-matrices are arranged as row vectors $(b_{xx}, b_{yy}, b_{zz}, b_{xy}, b_{xz}, b_{yz})$. The rows are sorted by the respective gradient amplitude. This leads to the $(6 \times d)$-dimensional $\mathbf{b_{ij}}$-matrix,

$$\mathbf{b_{ij}} = \underbrace{\left.\begin{pmatrix} b_{xx,1} & b_{yy,1} & b_{zz,1} & b_{xy,1} & b_{xz,1} & b_{yz,1} \\ b_{xx,2} & b_{yy,2} & b_{zz,2} & b_{xy,2} & b_{xz,2} & b_{yz,2} \\ \cdots & \cdots & \cdots & \cdots & \cdots & \cdots \\ b_{xx,d} & b_{yy,d} & b_{zz,d} & b_{xy,d} & b_{xz,d} & b_{yz,d} \end{pmatrix}\right\} d\,\text{PFG steps}}_{6\ \text{tensor elements}} \tag{7.8}$$

If for example a measurement is performed in x direction, only the first column of the $\mathbf{b_{xx}}$-matrix will be different from zero.

For convenient programming all six measurements of the different PFG directions $\boldsymbol{G_{xx}}$, $\boldsymbol{G_{yy}}$, $\boldsymbol{G_{zz}}$, $\boldsymbol{G_{xy}}$, $\boldsymbol{G_{xz}}$, and $\boldsymbol{G_{yz}}$ are further combined. Therefore, the $6 \times d$-dimensional vector $\boldsymbol{s}$ contains one by one the NMR signal of the vectors $\boldsymbol{S_{ij}}$,

$$\boldsymbol{s} = (\boldsymbol{s_{xx}}(b_{xx}),\, \boldsymbol{s_{yy}}(b_{yy}),\, \boldsymbol{s_{zz}}(b_{zz}),\, \boldsymbol{s_{xy}}(b_{xy}),\, \boldsymbol{s_{xz}}(b_{xz}),\, \boldsymbol{s_{yz}}(b_{yz}))^{\mathrm{T}}\,. \tag{7.9}$$

Also a new **b**-matrix has to be defined, which contains all six $\mathbf{b_{ij}}$-matrices. This matrix will be named $\mathbf{b}_{6d}$-matrix, and the $\mathbf{b_{ij}}$-matrices will be aligned one below each other,

$$\mathbf{b}_{6d} = (\mathbf{b_{xx}},\, \mathbf{b_{yy}},\, \mathbf{b_{zz}},\, \mathbf{b_{xy}},\, \mathbf{b_{xz}},\, \mathbf{b_{yz}})^{\mathrm{T}}\,. \tag{7.10}$$

The $\mathbf{b}_{6d}$-matrix consists of six column vectors and $6 \times d$ raw vectors.

The typical way in medical DTI investigations for calculating the diffusion coef-

ficients D_{ij} is via the pseudoinverse $\left(\mathbf{b}_{6d}\,\mathbf{b}_{6d}^{\mathrm{T}}\right)^{-1}$ of the $\mathbf{b}_{6d}$-matrix [BML94],

$$\boldsymbol{\alpha}^{\mathrm{T}} = \left(\mathbf{b}_{6d}\,\mathbf{b}_{6d}^{\mathrm{T}}\right)^{-1}\mathbf{b}_{6d}\,\boldsymbol{s}^{\mathrm{T}}, \tag{7.11}$$

whereby $\boldsymbol{\alpha}$ contains the diffusion coefficients,

$$\boldsymbol{\alpha} = \left(D_{xx},\, D_{yy},\, D_{zz},\, D_{xy},\, D_{xz},\, D_{yz}\right)^{\mathrm{T}}. \tag{7.12}$$

The pseudoinverse is commonly calculated using the Moore-Penrose definition [Moo20, Pen55].

Since the PFGs have been applied in the directions of the laboratory coordinate system, $\mathbf{D}$ describes diffusion referring to the laboratory coordinates. In case of anisotropic diffusion from internal structures or other spatial confinements, the diffusion tensor has to be rotated into the sample coordinate system. This is done by determining the eigenvalues λ_i and eigenvectors $\boldsymbol{a}_i$, $i = 1, 2, 3$ by

$$\left(\mathbf{D} - \lambda_i \mathbf{I}\right)\boldsymbol{a}_i = 0. \tag{7.13}$$

$\mathbf{I}$ denotes the identity matrix. The normalized eigenvectors $\boldsymbol{a}_i$ form a basis of the diffusion tensor, thus describe its orientation in the laboratory coordinate system. The eigenvalues λ_i give the intensity of diffusion along $\boldsymbol{a}_i$. In case of isotropic diffusion, $\lambda_1 = \lambda_2 = \lambda_3$, while for anisotropic diffusion the eigenvalues differ. For example, xylem cells in plants are prolonged along the stem orientation. Here, one eigenvalue will have a larger value, the other two will have lower but equal values $\lambda_1 > \lambda_2 = \lambda_3$. The eigenvector belonging to the large eigenvalue will point into the prolonged direction of the plant cell.

The determination of the eigenvalues and eigenvectors is done for all pixels of the entire measured DTI data set.

It is a challenge to visualize three eigenvalues per pixel in two-dimensional maps including many pixels. In medical DTI applications it is common to reduce the eigenvalues to indices, which describe the anisotropy in each pixel. In this thesis the so called fractional anisotropy FA is presented, defined as [LMP01]

$$FA = \sqrt{\frac{3\Big[\left(\lambda_1 - \langle\lambda\rangle\right)^2 + \left(\lambda_2 - \langle\lambda\rangle\right)^2 + \left(\lambda_3 - \langle\lambda\rangle\right)^2\Big]}{2\Big(\lambda_1^2 + \lambda_2^2 + \lambda_3^2\Big)}}. \tag{7.14}$$

$\langle\lambda\rangle$ denotes the mean of the three eigenvalues of a pixel, $\langle\lambda\rangle = \frac{1}{3}(\lambda_1 + \lambda_2 + \lambda_3)$. *FA* varies between 0 for isotropic diffusion and 1 for anisotropic diffusion.

Another way of presenting the eigenvalues and eigenvectors of each diffusion tensor in the MRI data set is a three-dimensional visualization of the tensors. This common medical method was altered for the application on the root. Here, each normalized eigenvector is multiplied with its associated eigenvalue. This results in one coordinate system per pixel. The axes are related to diffusion in the respective direction. Now, all the coordinate systems serve as main axes of ellipsoids representing the shape of the diffusion tensor. In case of isotropic diffusion, the ellipsoids degenerate to spheres. In xylem cells, the ellipsoids show a cigar-shaped diffusion tensor.

7.2. New approach of determining diffusion tensors

Since the $\mathbf{b}_{6d}$-matrix as introduced in Chapter 7.1.3 has only a few entries from the applied PFG directions, the rank of this matrix is low. However, the Moore-Penrose method is optimized for high ranked matrices. Furthermore, the DTI measurements on maize roots discussed in Chapter 8.1.3 show a non-vanishing offset from zero signal for high PFG amplitudes. Such an offset cannot be taken into account with the previously presented method (Eq. (7.11)), since for this procedure the signal has to show a pure exponential decay (see Eq. (7.6)). Therefore, Eq. (5.42) has to be modified to account for an offset C:

$$S(t) = S(0) \exp\left\{ - \sum_{i=x,y,z} \sum_{j=x,y,z} b_{ij} D_{ij} \right\} + C. \tag{7.15}$$

Thus, Eq. (7.5) and with this Eq. (7.11) are no longer valid for calculating the diffusion coefficients. Instead, another method has to be used.

7.2.1. The concept of least squares fitting

One possible way for solving the coupled system of six equations (Eq. (7.15)) and fitting the diffusion coefficients is a Levenberg-Marquardt least squares fit [Mar63]. The best model fit in the least squares sense minimizes the sum of squared residuals,

a residual being the difference between an observed value and the fitted value.

Applied to fitting diffusion coefficients, the following minimization has to be solved for $\boldsymbol{\alpha}$:

$$\min_{\boldsymbol{\alpha}} \sum_{i=1}^{6d} \left(f(\mathbf{b}_{6d,\,[0-5,i]}, \boldsymbol{\alpha}) - \boldsymbol{s}_{\,[i]} \right)^2 . \tag{7.16}$$

Since all $6 \times d$ measurements are taken into account, in Eq. (7.16) the definitions of $\boldsymbol{s}$, $\mathbf{b}_{6d}$, and $\boldsymbol{\alpha}$ are used (see Eq. (7.9), Eq. (7.10), and Eq. (7.12), respectively). The term $\mathbf{b}_{6d,\,[0-5,i]}$ denotes the ith row of the $\mathbf{b}_{6d}$-matrix, containing the six values of the corresponding $\mathbf{b}$-matrix, b_{xx}, b_{yy}, b_{zz}, b_{xy}, b_{xz} and b_{yz}. In the same way, $\boldsymbol{s}_{\,[i]}$ describes the ith measured NMR signal. Again, the vector $\boldsymbol{\alpha}$ contains the fitted diffusion coefficients. Since now also C can be taken into account, $\boldsymbol{\alpha}$ is expanded to

$$\boldsymbol{\alpha}_C = (D_{xx},\, D_{yy},\, D_{zz},\, D_{xy},\, D_{xz},\, D_{yz},\, C)^{\mathrm{T}} . \tag{7.17}$$

After all diffusion tensors have been determined, the eigenvalues and eigenvectors are calculated as described from Eq. (7.13) on and again two and three-dimensional visualizations of the tensors are produced.

Note that both presented methods are able to fit also the NMR signal $S(0)$ at zero gradient amplitude. The method using the pseudoinverse matrix has to be modified by simple redefinitions. The least squares method allows directly the fit of $S(0)$ by an additional extension of the vector $\boldsymbol{\alpha}_C$.

7.2.2. Demonstration on model data

To validate the least squares method, the Moore-Penrose method and Levenberg-Marquardt least squares approach are tested on model data in this section. Starting point is a diffusion tensor $\mathbf{D}_{\mathrm{model}}$ with given coefficients. In addition, the signal $S(0)$ and the offset C were given. The aim was to recalculate the diffusion tensor and its eigenvalues and to compare the results of the two methods.

Assuming isotropic diffusion, the following initial values were chosen:

$$S_{\mathrm{model}}(0) = 0.9, \quad C_{\mathrm{model}} = 0.009,$$
$$\mathbf{D}_{\mathrm{model}} = 3.0 \times 10^{-9} \times \begin{pmatrix} 1 & 0 & 0 \\ 0 & 1 & 0 \\ 0 & 0 & 1 \end{pmatrix} \mathrm{m^2\,s^{-1}}. \tag{7.18}$$

C_{model} was set to the low rate of 1 % of $S_{\mathrm{model}}(0)$ to look at the effect of already such a small disturbance. In actual DTI measurements performed on maize roots, the offset was around 5 % of $S(0)$. With the parameters given in Eq. (7.18) an expected NMR signal for PFGs applied in different directions can be calculated by Eq. (7.15).

Moore-Penrose pseudoinverse

Processing the model data with the Moore-Penrose method leads to the following signal amplitude $S_{\mathrm{MP}}(0)$ and diffusion tensor $\mathbf{D}_{\mathrm{MP}}$:

$$S_{\mathrm{MP}}(0) = 0.26, \quad \mathbf{D}_{\mathrm{MP}} = \begin{pmatrix} 3.0 \times 10^{-9} & -1.6 \times 10^{-10} & -1.6 \times 10^{-10} \\ -1.6 \times 10^{-10} & 3.0 \times 10^{-9} & -1.6 \times 10^{-10} \\ -1.6 \times 10^{-10} & -1.6 \times 10^{-10} & 3.0 \times 10^{-9} \end{pmatrix} \mathrm{m^2\,s^{-1}}. \tag{7.19}$$

The diagonal elements of $\mathbf{D}_{\mathrm{MP}}$ are equal to the given values $\mathbf{D}_{\mathrm{model}}$. However, the off-diagonal elements are only one order of magnitude smaller than the diagonal elements although isotropic diffusion was assumed. The reconstructed signal $S_{\mathrm{MP}}(0)$ is about a factor of three lower than the given signal $S_{\mathrm{model}}(0)$. These deviations result from the assumed offset C_{model}.

The reconstructed eigenvalues

$$\begin{aligned} \lambda_{1,\,\mathrm{MP}} &= 2.7 \times 10^{-9}\,\mathrm{m^2\,s^{-1}}, \\ \lambda_{2,\,\mathrm{MP}} &= 2.7 \times 10^{-9}\,\mathrm{m^2\,s^{-1}}, \\ \lambda_{3,\,\mathrm{MP}} &= 2.2 \times 10^{-9}\,\mathrm{m^2\,s^{-1}}, \end{aligned} \tag{7.20}$$

describe anisotropic behavior despite the given isotropy of the model data.

This model calculation shows that the Moore-Penrose pseudoinverse method is not suited to produce reliable diffusion coefficients in the presence of data offsets.

This statement applies therefore especially on maize root DTI measurements.

Levenberg-Marquardt least squares fit

Applying a Levenberg-Marquardt least squares fit on the model data results in the following signal amplitude $S_{\mathrm{LM}}(0)$, signal offset C_{LM} and diffusion tensor $\mathbf{D}_{\mathrm{LM}}$:

$$\begin{aligned} S_{\mathrm{LM}}(0) &= 0.9, \quad C_{\mathrm{LM}} = 0.009, \\ \mathbf{D}_{\mathrm{LM}} &= \begin{pmatrix} 3.0 \times 10^{-9} & 1.8 \times 10^{-17} & 1.8 \times 10^{-17} \\ 1.8 \times 10^{-17} & 3.0 \times 10^{-9} & 1.8 \times 10^{-17} \\ 1.8 \times 10^{-17} & 1.8 \times 10^{-17} & 3.0 \times 10^{-9} \end{pmatrix} \mathrm{m^2\,s^{-1}}. \end{aligned} \tag{7.21}$$

In this case the criteria for isotropic diffusion are fulfilled. The off-diagonal elements of the diffusion tensor $\mathbf{D}_{\mathrm{LM}}$ are negligible compared to the diagonal elements. Also the initial signal $S_{\mathrm{LM}}(0)$ and the offset C_{LM} reproduce well the given model data. Thus, the eigenvalues calculated from $\mathbf{D}_{\mathrm{LM}}$ are all the same,

$$\begin{aligned} \lambda_{1,\,\mathrm{MP}} &= 3.0 \times 10^{-9}\,\mathrm{m^2\,s^{-1}}, \\ \lambda_{2,\,\mathrm{MP}} &= 3.0 \times 10^{-9}\,\mathrm{m^2\,s^{-1}}, \\ \lambda_{3,\,\mathrm{MP}} &= 3.0 \times 10^{-9}\,\mathrm{m^2\,s^{-1}}. \end{aligned} \tag{7.22}$$

This shows that the Levenberg-Marquardt least squares method is suited for the determination of diffusion tensors from real DTI measurements on plant roots.

8. Results and discussion

8.1. Diffusion tensor imaging on plant roots

For understanding water motion in plant roots, in this chapter the first application of diffusion tensor imaging on plant roots is presented.

8.1.1. Experimental setup for high resolution MRI and DTI measurements

To investigate the root structure of a plant both high resolution MRI as well as DTI measurements were performed on a maize plant. Figure 8.1 shows schematically the experimental setup for these measurements.

The maize plant is centered and fixed in the 7 T Scanner in the Forschungszentrum Jülich. For inducing the water flow inside the plant and with that also in the roots, the plant was illuminated to ensure transpiration via its leaves. For all NMR measurements on the plant roots in multi slice experiments slices in the xy plane along z direction were selected. The coordinate system in Figure 8.1 indicates the directions in the laboratory coordinate system.

8.1.2. High resolution NMR imaging on plant roots

To identify the areas of anisotropic diffusion in the maize roots, first anatomical magnetic resonance images were taken and compared to optical microscopic images. Figure 8.2 shows an optical microscopic image of a maize root.

The slice depicted in this figure was taken from the upper part of the single root at a region close to the spear. The root diameter at this position is large, $\phi = 1.5\,\mathrm{mm}$, compared to the diameter at the tip of the root ($\phi < 0.7\,\mathrm{mm}$). According to Hochholdinger [Hoc09] the ground tissue of the root is built by single epidermis (a) and exodermis (b) cell layers, multiple layers of cortex (c) and a single

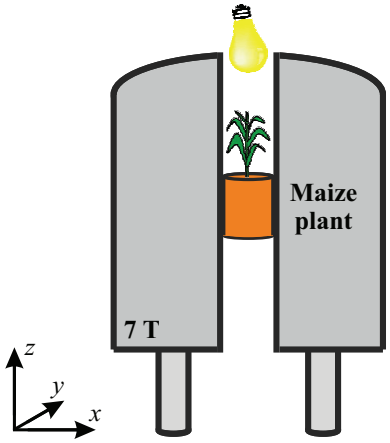

Figure 8.1: *Experimental setup for high resolution MRI and DTI measurements on plant roots. The maize plant is centered in the magnet system, the illumination ensures transpiration of the plant via its leaves. The coordinate system indicates the imaging directions in the laboratory coordinate system.*

endodermis layer (d). The central cylinder is composed of phloem (e), xylem elements (f) and the pith (g). In plant roots the main pathway of water is through the vascular bundles of the xylem system, which transports the water from the roots via the spear to the leaves. The driving force is transpiration through the leaves.

The two squares in Figure 8.2 indicate the spatial resolution of different types of NMR experiments undertaken on a maize plant. The small square with an edge length of 62.5 μm represents the size of a single pixel in high resolution NMR imaging, over which the NMR signal is averaged. In contrast, the large square with an edge length of 281 μm shows the resolution of the diffusion tensor imaging (DTI) measurements. The resolution of anatomical MRI investigations is significantly higher than the resolution of DTI measurements. This mainly results from an improved signal to noise ratio in case of anatomical MRI and an appropriate measurement time. The lower resolution of DTI indicates that the NMR signal of the pixels is averaged from water molecules in the vascular bundles and the smaller spherical cells around the xylem (see Figure 8.2). However, the pixel size is still small enough

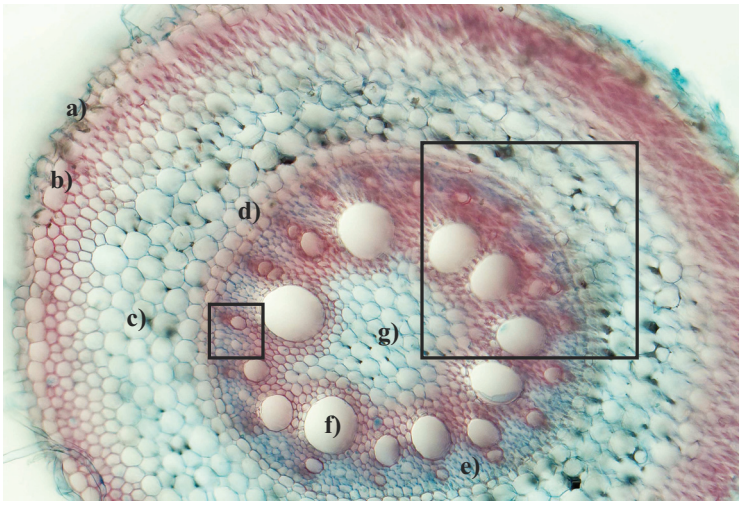

Figure 8.2: *Optical microscopic slice of a maize root. Lignified cell walls are colored in red from dyeing with safranin red. Cellulose walls appear blue due to the dyeing with astra blue. The squares indicate the resolution of anatomical MRI investigations (small, length:* $62.5\,\mu$m*) and DTI investigations (large, length:* $281\,\mu$m*), respectively. Labeled are five different functional parts of the root: a) epidermis, b) exodermis, c) cortex, d) endodermis, e) phloem, f) xylem, g) pith.*

so that more than one pixel fit in the root. Therefore, the NMR signal resulting from water molecules inside roots can be distinguished from the surrounding soil. Thus, DTI is suited for investigating diffusion dynamics in plant roots.

In addition, cross-sectional images of the upper part of the root system were taken where roots branch off from the spear. A typical optical microscopic image is shown on the left hand side of Figure 8.3. The right hand side of this figure presents an anatomical high resolution NMR image, measured at the same position in the root system.

In Figure 8.3 the color bar below the right image represents the MRI signal intensity in arbitrary units. In both images of Figure 8.3 the inner structure of the spear (a) is clearly visible despite the complex anatomical structure. Also the beginning of the vascular bundles of the xylem (b) branching off the spear can be found. Since the NMR image shows a cross-section of the root, on the top right part of the picture two bright regions of the xylem (c) can be distinguished. The inner and outer surrounding part of the root appear darker in the NMR signal intensity map.

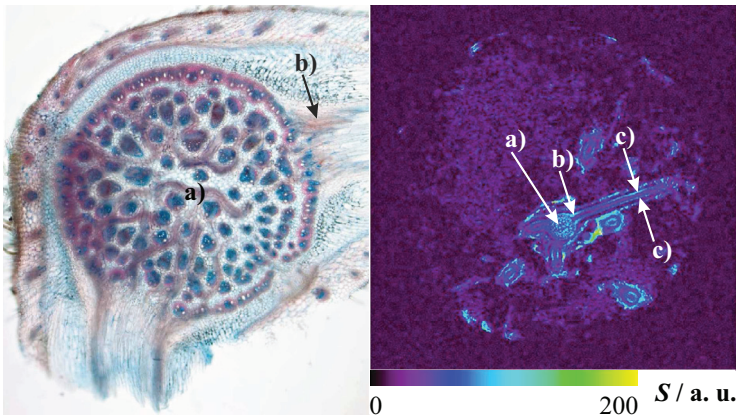

Figure 8.3: *Comparison of an optical microscopic slice (left) with a high resolution anatomical NMR image (right) of the maize spear in the area, where roots branch off. In both pictures a) denotes the spear of the maize plant and b) and c) indicate vascular bundles of the xylem. In the optical microscopic slice lignified cell walls are colored in red while cellulose walls are visible in blue due to the dyeing with safranin red and astra blue. The color bar below the right image represents the MRI signal intensity in arbitrary units. TR = 1500.0 ms, τ = 6.5 ms, FOV: 32.0×32.0 mm², matrix size: 512×512 pixels resulting in a resolution of 62.5 µm pixel⁻¹, number of scans: 8, number of slices: 10, slice thickness: 0.6 mm, measurement time: 1 h 42 min 24 s.*

The high resolution NMR image in Figure 8.3 was taken to identify the anatomy of the root. The MRI measurement was performed on a maize plant grown in a tube filled with natural sand. The entire plant was inserted in the 7 T system for imaging as sketched in Figure 8.1. Thus, an entire cross-sectional slice of the tube containing the maize plant was mapped. The circular shape of the NMR image is the projection of the cylindrical tube on the cross-sectional slice. The image shows not only the maize spear and off-branching roots. Also other roots, passing through the selected slice, can be identified in the intensity map. There is even signal from water in pores of the natural sand in which the maize plant was growing. However, the echo time $t_e = \tau = 13.0$ ms was much longer than the short T_2 relaxation time of water in the sand (only a few ms). Thus, the NMR signal from the sand is already dephased and results only in noise. In contrast, due to a longer T_2 relaxation time of the roots ($T_2 \approx 50$ ms), the NMR signal from roots is much higher and can be differentiated from the noisy sand signal.

After the measurement of in total 80 cross-sectional MRI slices, it was possible to reconstruct the three-dimensional surface structure of the maize roots. One side view of the root structure shows Figure 8.4.

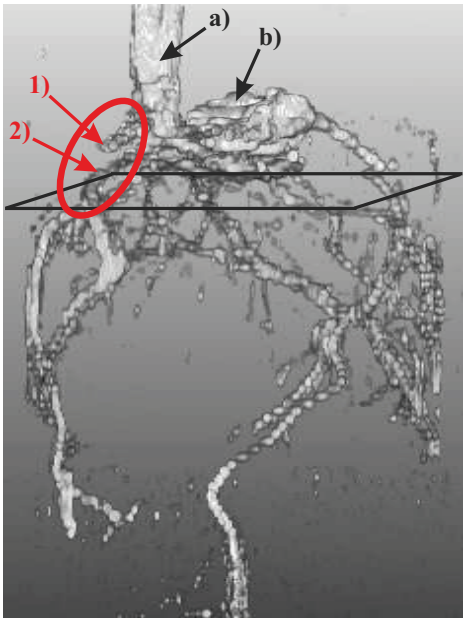

Figure 8.4: *Side view of three-dimensional reconstructed root system of a maize plant resulting from MRI measurements. a) marks the spear of the plant and b) the maize seed. The black rectangle indicates the region recorded with DTI. The results are presented in the following exemplary on one single cross-sectional slice with the position indicated here. The red arrows and 1) and 2) mark an inconsistency in the reconstruction as discussed in the text. TR = 1500.0 ms, τ = 20.0 ms, FOV: 36.0×36.0 mm^2, matrix size: 256×256 pixels resulting in a resolution of 141 μm pixel^{-1}, number of scans: 4, number of slices: 20, slice thickness: 1.0 mm, measurement time: 1 h 42 min 24 s.*

The three-dimensional surface reconstruction contains not only plant roots, but also the lower part of the maize spear (a). The spear grew out from the maize seed (b) which resulted after sprouting in a complex structure with both off-branching roots and the spear. The reconstructed maize root system of Figure 8.4 already looks close to an anatomical root system as shown in the right picture of Figure 2.2. However, due to image disturbances such as susceptibility effects, information about roots is lost. This manifests in interruptions with zero NMR signal amplitude in

the course of single root, while the physical root continues without any gaps. Such an interruption in the reconstructed root structure is marked with a red ellipse in Figure 8.4. A gap can be clearly seen between the part of the root connected to the spear-seed-system (1) and the ongoing root (2). Visibly it is evident that these two root parts belong to the same root. However, it is not evident from the NMR imaging experiment and is therefore hard to implement into an automated root tracking algorithm. Since anatomical MRI measurements give only information about the spin density of water molecules, these experiments give no reason for combining two root fragments. Things are different, if the motion direction of the water molecules in each pixel is known, described by vectors. Then, interpolating between two spatially separated pixels and constructing an undisturbed root structure might be possible by means of the motion vectors. With either direct measurement of flow or indirect observation by water diffusion measurements, two techniques exist to determine the motion direction. Since in the vascular bundles of the xylem, anisotropic diffusion is expected, diffusion tensor imaging seemed to be promising. Furthermore, it was the first time that DTI was applied on plant roots. A three-dimensional reconstruction technique, using for instance fiber tracking methods, has to be determined in future work originating on the results discussed in the following.

8.1.3. Diffusion tensor imaging on plant roots

For DTI measurements twelve axial slices were acquired directly below the maize seed corn. In the following discussion only one exemplary slice is considered for sake of simplicity. Besides roots the slice contains also a part of the seed. The exact position of the slice is marked with a black frame within the 3D root system reconstruction in Figure 8.4.

Before the measured DTI data can be analyzed, it is necessary to identify root structures. Therefore, an additional high resolution MRI measurement was performed on the DTI slice position. A high resolution NMR image of the selected slice is depicted in Figure 8.5. It is possible to identify roots in that image.

This image was taken exactly at the same position where also the DTI measurements were performed. In contrast to common NMR images such as shown on the right hand side of Figure 8.3, in Figure 8.5 the color bar is inverted. This improves the visible contrast inside the picture to differentiate root signal from signal resulting from water in the sand pores or from the sample surrounding noise. The laboratory

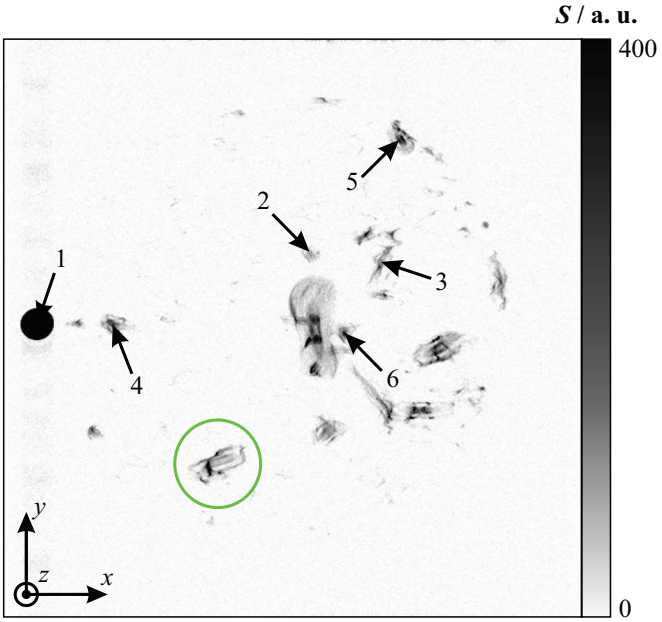

Figure 8.5: *High resolution NMR image of the selected slice to identify regions containing roots. The color bar is inverted to improve the visibility of root structures. The NMR signal from sand and the noise signal are white. The black circular spot on the left side of the intensity map (1) is the reference capillary filled with an aqueous solution of 5 mmol L^{-1} $NiCl_2$. One root is exemplary circled in green. The numbers (2 to 5) mark single pixels in the roots. The DTI results of these pixels will be discussed further on. The coordinate system drawn in the bottom left indicates the directions of the laboratory coordinate system. TR = 2000.0 ms, τ = 6.5 ms, FOV: 36.0×36.0 mm^2, matrix size: 512×512 pixels resulting in a resolution of 70.0 μm $pixel^{-1}$, number of scans: 8, number of slices: 32, slice thickness: 1.0 mm, measurement time: 2 h 16 min 32 s.*

coordinate system given in the lower left helps identifying the growth direction of the roots.

The highest NMR signal intensity results from the reference capillary, seen on the middle left in Figure 8.5 as a black circular spot (1). The capillary is filled with an aqueous solution of 5 mmol L^{-1} $NiCl_2$. The large structure right in the center of the intensity map with a prolongation in y direction belongs to the maize seed. Since the inner structure of the seed is quite complex and preferred water motion directions cannot be determined easily in this heterogeneous structure, DTI results are only discussed on roots. The maize spear growing out of the seed is not a part of

the high resolution NMR image, it has left the seed at a higher z position. Different growing directions of the roots are identified. In first approximation the roots are expected to grow in z direction, perpendicular to the slice shown in Figure 8.5. This would result in small restricted spherical structures with a high NMR signal intensity showing the roots in contrast to low signal from the soil. Instead, most of the roots found in the intensity map are spatially extended. For the root marked with a green circle in Figure 8.5 it can be assumed that the growing direction is dominant in x direction with some fraction of y direction and a minor fraction in z direction. Therefore, the water motion inside this root cannot be expected only in z direction.

In the following section is discussed diffusion in several roots grown in different directions. Single pixels are selected from these roots, numbered from 2 to 5 in Figure 8.5 and indicated by arrows. Pixel 1 in the center of the capillary serves as reference. This pixel should show isotropic diffusion. Pixel 2 is positioned in a root growing in z direction. For this pixel restricted diffusion in x and y direction is expected. Instead, the diffusion in x direction in Pixel 4 will be less restricted according to the growing direction of the root. However, the two-dimensional intensity map does not provide any information about the growing directions. Thus, the information given here about the growing directions in the selected pixels were obtained from analyzing the above and below laying MRI slices. Therefore, it is necessary to study the diffusion tensors of the selected six pixels for getting information about the actual preferred water motion directions within one MRI slice.

The intensity map shown in Figure 8.6 results from DTI measurement at zero PFG amplitudes. Therefore, this measurement is similar to the high resolution image of Figure 8.5, measured with a spin echo multi slice imaging pulse sequence. Compared to the high resolution image, the spatial resolution of Figure 8.6 is reduced; and due to the additional observation time Δ in DTI the echo time was increased.

Even the lower spatial resolution of DTI measurements compared to the high resolution image of Figure 8.5 is sufficient to clearly distinguish the roots from the surrounding sand. The six pixels selected in Figure 8.5 are again marked in Figure 8.6. Due to the lower spatial resolution in DTI experiments the selected pixels were chosen from inside the root. This avoids partial volume effects which result, if the NMR signal in a pixel is averaged over both the root and the surrounding soil. Since the vascular bundles of the root xylem system is closer to the root center than to the surface, it is ensured that the selected pixels represent the diffusion behavior

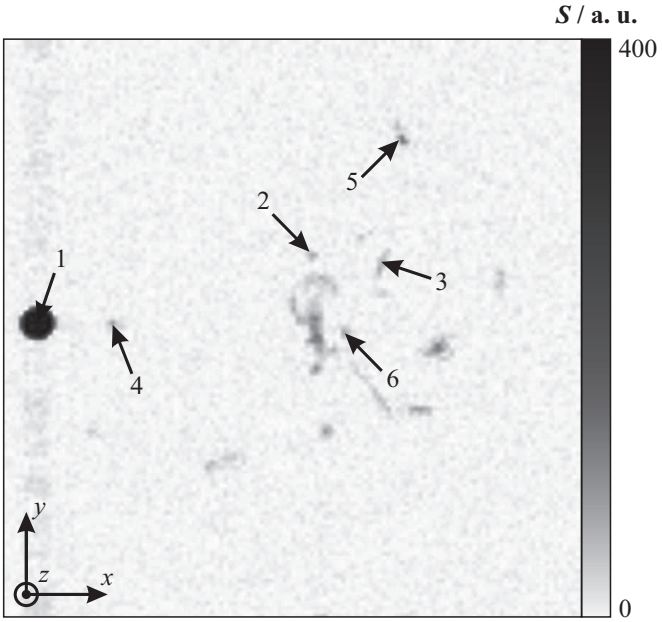

Figure 8.6: *Intensity map from DTI measurement with zero PFG amplitudes. The numbers indicate the same pixels as introduced in Figure 8.5; the laboratory coordinate system is inserted. TR = 3000.0 ms, τ = 22.5 ms, FOV: 36.0×36.0 mm^2, matrix size: 128×128 pixels resulting in a resolution of 281 μm pixel^{-1}, number of scans: 1, number of slices: 12, slice thickness: 1.0 mm, $G_{max} = 0.220$ T m^{-1}, number of PFG steps: 11, δ = 3.0 ms, Δ = 40.0 ms, measurement time: 7 h 2 min 24 s.*

of water moving in the vascular bundles.

In Figure 8.6 the pixels can be selected even easier than in the intensity map of the high resolution image, because the NMR signal of the surrounding sand was already at the noise level due to T_2 relaxation. Because of the long DTI observation time Δ, signal from water molecules in sand pores has already declined before the 180° pulse would have been able to rephase the magnetization of the molecular spins.

To focus on the root DTI signal, the pure sand and the surrounding were faded out by a mask. The mask was constructed from DTI measurements at zero PFG amplitudes by defining an NMR signal threshold. Signal from the roots lies above the threshold and is kept, while the noisy signal is set to zero. Each diffusion experiment in x, y, and z direction as well as in the combined directions xy, xz, and yz was started with zero PFG amplitude. After this measurement, the amplitude

was stepwise increased. The masks obtained from all six measurement directions were overlayed to construct the total mask. A pixel in the total mask was set to zero, if at least the pixel in one of the six individual masks was set to zero.

Entirely 66 DTI measurements (six directions each with eleven gradient steps) were performed. The diffusion tensors for all pixels were determined by fitting the experimental data with the Levenberg-Marquardt least squares fit method as introduced in Chapter 7.2.1. Therefore, in the following section the diffusion in single selected pixels as first depicted in Figure 8.5 is discussed. The NMR signal intensity plots in Figure 8.7 depending on the PFGs correspond to the arrow-labeled root locations in Figure 8.5. The horizontal axes of Figure 8.7 show the absolute value b of the **b**-matrix, which can be calculated according to Eq. (5.36) with

$$b = (\gamma G \delta)^2 \left(\Delta - \tfrac{1}{3}\delta\right). \tag{8.1}$$

In Figure 8.7 the colored symbols refer to different measurement directions (black squares: x direction, red spheres: y direction, and green triangles: z direction). The lines are the fitted curves resulting from Levenberg-Marquardt least squares fits as introduced in Chapter 7.2.1. To discuss the plots of Figure 8.7 the fitted diffusion coefficients shown in Table 8.1 are helpful. The errors of the diffusion coefficients denote the 1σ tolerance of the fitting result.

Table 8.1: *Diagonal diffusion coefficients of the diffusion tensors from pixels marked in Figure 8.5 determined by least squares fits to the NMR data shown in Figure 8.7.*

Pixel	D_{xx} / 10^{-9} m^2 s^{-1}	D_{yy} / 10^{-9} m^2 s^{-1}	D_{zz} / 10^{-9} m^2 s^{-1}
1	2.7 ± 0.1	2.5 ± 0.0	2.5 ± 0.1
2	0.6 ± 0.2	0.6 ± 0.2	1.6 ± 0.7
3	0.8 ± 0.1	1.8 ± 0.5	2.1 ± 0.4
4	2.2 ± 0.7	1.2 ± 0.3	3.1 ± 1.2
5	1.0 ± 0.1	1.1 ± 0.2	2.8 ± 0.4
6	0.6 ± 0.0	1.7 ± 0.2	2.5 ± 0.1

The NMR signal in the reference capillary represented by Pixel 1 decreases with increasing b-value with the same slope in all three diagonal directions (see Figure 8.7A). This proves that the diffusion in the reference tube is isotropic. The diagonal diffusion coefficients inside the capillary resemble well the diffusion coefficient of free water of $D_{\mathrm{H_2O}} = 2.5 \times 10^{-9}\,\mathrm{m^2\,s^{-1}}$. Inserting also the observation time of

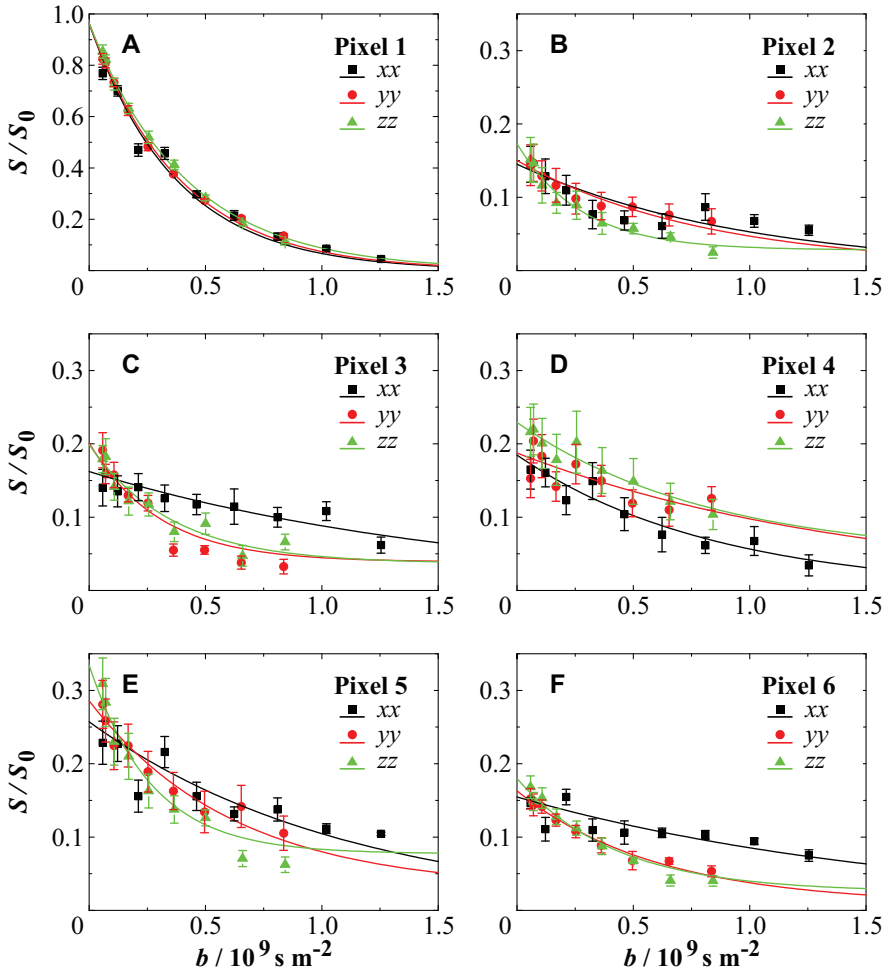

Figure 8.7: *Decay of NMR signal with increasing b-value of selected pixels in the reference capillary (pixel 1, (A)) and roots (pixel 2 - 6, (B) - (F)) at positions according to Figure 8.5. Each graph shows the measured NMR signal with PFGs applied in x, y, and z direction (symbols) and a fit according to Eq. (7.15) (solid lines). The doubled notification of the directions inside the plots labeling the colors used in the plots indicate the according diffusion coefficients on the diagonal of the diffusion tensor. Note that the signal intensity S of all plots is normalized by the signal intensity S_0 measured at zero applied PFGs in the reference capillary.*

$\Delta = 40\,\text{ms}$ in the Einstein equation (Eq. (3.7)), the mean displacement is calculated to $|\boldsymbol{R}| = 24\,\mu\text{m}$. This path length is small compared to the diameter of the reference

tube of 1 mm and thus unrestricted water self-diffusion in the reference capillary is confirmed.

In the following, the results from Pixel 2 up to Pixel 6 inside roots are discussed. The plots of all these five pixels show a signal offset different from zero for high b-values resulting from noise. The curve fits have to take the offset into account. This was the reason why the method of Levenberg-Marquardt least squares fits for the determination of the diffusion tensors was chosen (Chapter 7.2).

Pixel 2 is located inside a vertically growing root. Therefore, the root and its vascular bundles are perpendicular to the slice. It is expected that water moves mainly along z direction, with lower contributions in the lateral directions. Indeed, the comparison of the NMR signal decay in x, y, and z direction (Figure 8.7B) confirms this expectation. The apparent vertical diffusion coefficient D_{zz} outranges the perpendicular coefficients D_{xx} and D_{yy} by a factor of 3.

In contrast, Pixel 3 represents a root which is mainly orientated in the yz plane. Thus, the root does not penetrate the selected slice perpendicularly. This is confirmed in the high resolution image (Figure 8.5), showing an elliptically distorted cross section of the cylindrical root. Since the root grows preferentially lateral in y direction, diffusion in both y and z direction is expected. Figure 8.7C shows the corresponding NMR signal in Pixel 3. As expected, the x component of the fitted diffusion coefficient is lower than the components in y and z direction.

An according result is found for the root represented by Pixel 4 (Figure 8.7D). This root is primarily orientated in z direction with also an x component in the growth path. This root does not extend into the y direction. Thus, D_{xx} and D_{zz} are high while D_{yy} is low in Pixel 4.

Both Pixel 5 (Figure 8.7E) and Pixel 6 (Figure 8.7F) indicate again roots with a growth path following mainly the z direction with some tilt into the y direction. As in Pixel 3, the diffusion coefficients are high in the according directions (D_{yy} and D_{zz}).

In summary, in all selected six pixels the diffusion coefficients are higher in the direction of the root axis than perpendicular to the root. This confirms that diffusion measurements fully reproduce the expected diffusion behavior inside the vascular bundles.

Since most roots are not growing along one of the main axes of the laboratory coordinate system, the system coordinates were found by means of the tensors' eigenvalues and eigenvectors (Chapter 7.1.3). After that, the actual diffusion behavior of the water molecules in their pixel is drawn in maps. Figure 8.8 shows the map of the highest eigenvalues of each pixel.

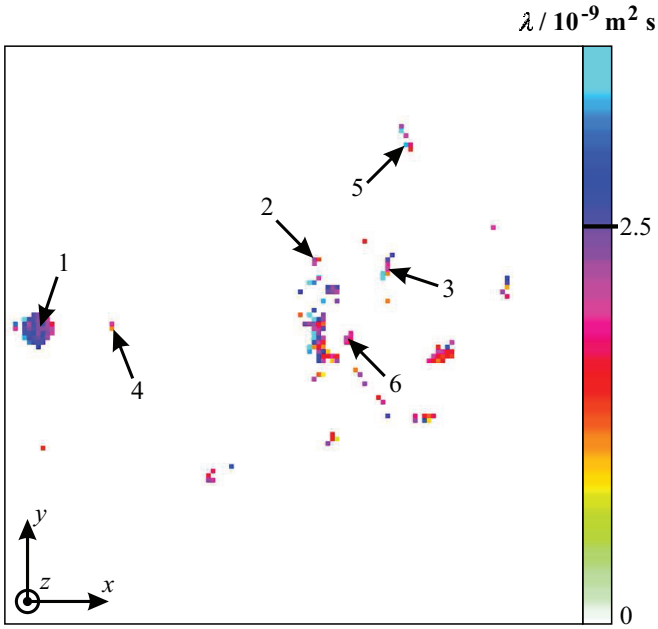

Figure 8.8: *Map of the highest eigenvalues of the diffusion tensors, determined from transforming the fitted diffusion tensors. The map is overlayed by a mask leaving only the signal from the roots, the maize seed and the reference capillary. The eigenvalues of the masked pixels are set to zero. The color bar quantifies the eigenvalues. The numbers indicate the same pixels as in Figure 8.5.*

In the figure, noise is faded out by the total mask. Only pixels from roots, the seed and the reference capillary remain in the map. The signal from pixels at the root surface is also canceled due to partial volume effects. Only internal pixels are left that include the vascular bundles of the xylem system. The eigenvalues of the suppressed pixels are set to zero, since molecular self-diffusion suppresses this value in praxis.

Most of the pixels shown in Figure 8.8 have a highest eigenvalue smaller than the self-diffusion coefficient of water ($D_{H_2O} = 2.5 \times 10^{-9}\,m^2\,s^{-1}$, marked in the color bar

of Figure 8.8 with a black bar). Note that the map of the highest eigenvalues does not provide the direction of the eigenvectors. Therefore, Figure 8.8 only gives the strength of diffusion.

Diffusion in the reference capillary in Figure 8.8 is in the range of the self-diffusion in pure water. This is expected since there are no diffusion limiting boundaries such as cell walls in the capillary. Since the capillary served as a reference, the obtained diffusion coefficient proves that least squares fits are appropriate. The roots show on average lower diffusion than the reference capillary. Since the diameter of the xylem vascular bundles is much smaller than the diameter of the reference capillary, convection enhanced diffusion is very unlikely.

The fractional anisotropy *FA* is a useful measure to identify anisotropic diffusion (Chapter 7.1.3). A map of fractional anisotropy is shown in Figure 8.9 for the previously considered NMR slice.

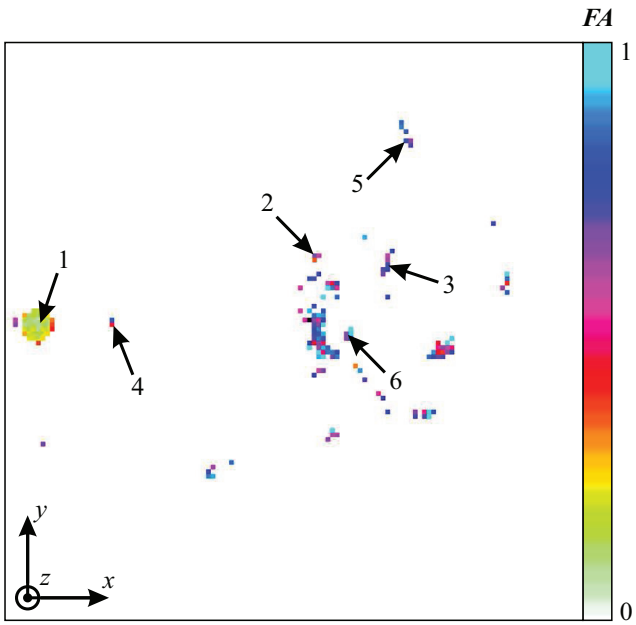

Figure 8.9: *Map of the fractional anisotropy FA of each pixel in the previously considered NMR slice. The map is overlayed by a mask leaving only the signal from the roots, the maize seed and the reference capillary. The FA-values of the masked pixels is set to zero. The color bar indicates the range of FA from 0 to 1. The numbers indicate the same pixels as in Figure 8.5.*

Again, the *FA* map is overlayed by the total mask. Thus, only pixels from roots, the seed and the reference capillary remain in the map. The *FA*-values of the masked pixels are set to zero without assuming totally isotropic diffusion behavior.

The *FA* map gives information about isotropic or anisotropic regions or at least different pixels. However, similar to the map of the highest eigenvalues, *FA* does not provide information about the origin of the diffusion anisotropies such as restrictions in one or two directions in space.

In Figure 8.9 clearly low *FA* is seen for pixels inside the reference capillary. The value is about the same, with negligible fluctuations. Thus, the water diffusion inside the reference capillary is not restricted in any dimension. Instead, the water underlies only isotropic self-diffusion. In contrast, *FA* in root pixels is significantly higher, indicating anisotropic diffusion. Since water inside the roots is transported in the tubular vascular bundles [Hoc09], restricted diffusion is expected. This is proved by the high *FA*-values in all root pixels in Figure 8.9. To estimate the anisotropy, the mean displacement inside roots can be calculated from the diffusion coefficients in Table 8.1. This leads to a value of $|\boldsymbol{R}| \approx 25\,\mu$m for the mean free pathway of water molecules inside the selected root pixels and would imply that the diameter of the tubular vascular bundles is almost in the range of $|\boldsymbol{R}|$. In contrast, in the microscopic image of Figure 8.2 an actual diameter of $\approx 70\,\mu$m of the xylem vessels can be found. The difference between the mean displacement found by DTI and the actual diameter of the vascular bundles results from the low resolution of the DTI measurements. The large square in Figure 8.2 shows that such a pixel mainly contains small cells, which are known to have a spherical shape [Hoc09]. Diffusion in such cells is strongly restricted without being anisotropic. Thus, the diffusion value resulting from the vascular bundle is reduced by the value of the small spherical cells. However, due to the reduction in all spatial directions the direction depending diffusion is not affected. Therefore, the reduced diffusion tensors still describe preferred diffusion directions.

In Chapter 7.1.3 another way of visualizing diffusion tensors was introduced. With this method colored ellipsoids produce a three-dimensional image of the eigenvalues and eigenvectors of each diffusion tensor. The shape of the ellipsoid shows the preferred diffusion direction and diffusion restrictions in the case of anisotropy. The color of each ellipsoid represents the direction of the highest eigenvalue in the laboratory coordinate system. Diffusion tensors visualized that way are shown in Figure 8.10 for different parts of the maize DTI image.

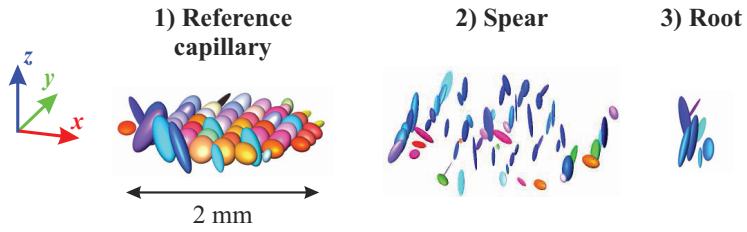

Figure 8.10: *Three-dimensional tensor visualization of eigenvalues and eigenvectors determined from the diffusion tensor of each pixel. Presented are single horizontal slice visualizations of the reference capillary (1), the maize spear (2) and a single root (3). The coordinate frame indicates the three directions of the laboratory coordinate system x, y, and z; the color of each ellipsoid represents the eigenvector of the highest eigenvalue.*

Color is coded according to the coordinate system in Figure 8.10. If for instance the eigenvector of the highest eigenvalue points in z direction, the ellipsoid will be blue. If the eigenvector points in between the y and the z direction, the ellipsoid will have a color mixed from green and blue.

Figure 8.10 contains a reconstructed cross section of the reference capillary (left, 1), a lateral cut through the spear of the maize plant (middle, 2), and a root penetrating the slice almost perpendicularly (right, 3).

Most of the diffusion tensor ellipsoids within the reference capillary are nearly spheres with a random color assigned. This indicates isotropic diffusion without preferred diffusion direction. Some non-spherical ellipsoids are found in the vicinity of the reference capillary surface. Their shape result from partial volume effects and limited diffusion properties on the inner capillary surface. This anisotropy can also be observed by a few increased *FA*-values on the right side of the reference capillary inFigure 8.9. One possibility for the anisotropy in this region is coarseness in the surface of the reference capillary.

In contrast, in both the spear and the root, preferred diffusion in z direction is indicated by the dominating blue color. Both in the spear and in the root D_{zz} is much larger than D_{xx} and D_{yy}, indicating highly anisotropic diffusion.

Finally, Figure 8.11 shows a tensor reconstruction of a single maize root over the full length of the root. For this image, twelve DTI slices were taken into account. Again, the coordinate system represents the directions in the laboratory coordinate system.

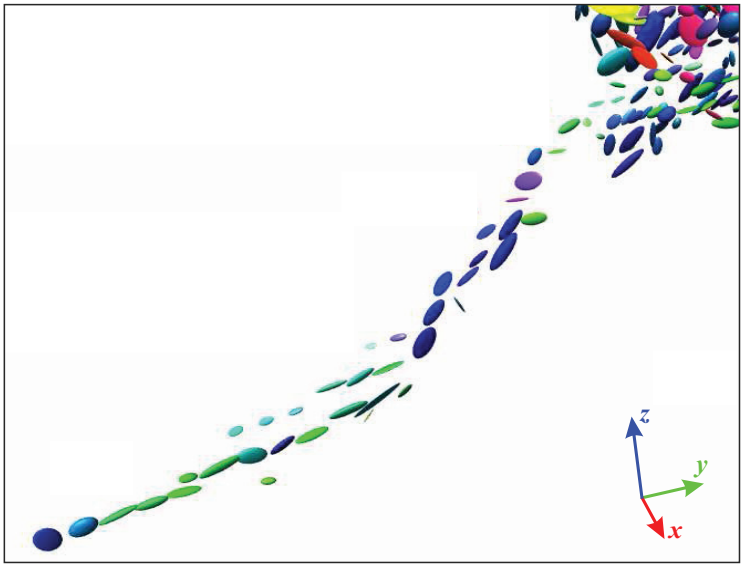

Figure 8.11: *Three-dimensional tensor visualization of a single root followed over twelve DTI measured slices. The coordinate system indicates the directions in the laboratory. The color of each ellipsoid represents the eigenvector of the highest eigenvalue.*

The diffusion path in the root can be followed very well. The preferred directions in y and z correspond to the growth path of the root. Originating in the spear, the root first grows almost vertically downwards until it bends towards the y direction and follows a straight line. The change in the diffusion behavior from the vertical part of the root to the lateral part is very well resolved in this diffusion tensor visualization. This results show that it is possible to identify water motion in roots using diffusion tensor imaging.

In this section the common medical technique DTI was applied to water pathway tracking inside plant roots for the first time. With DTI it was possible o visualize the diffusion tensor of each pixel and to follow the water pathway in maize roots. As expected, diffusion in direction of the vascular bundles of the roots is much higher than in the perpendicular directions. Due to a low signal to noise ratio the common data processing was replaced by the method of Levenberg-Marquardt least squares fit.

A challenge faced in these DTI measurements is that the spin dynamics is strongly influenced by T_2 relaxation. The reason is a long observation time of $\Delta = 40\,\mathrm{ms}$ between the two diffusion-encoding PFGs. The relaxation leads to a reduced signal to noise ratio and is the primary reason for the deviation of the measured NMR signal from a perfect exponential decay. Especially for investigations on natural soil with short T_2 relaxation times, the influence of relaxation on the NMR signal can be improved by minimizing the echo time and using a stimulated echo pulse sequence in future DTI studies.

8.2. One- and two-dimensional diffusion measurements in natural sand

In the previous chapter, water motion within the root system was determined. Since for a thorough understanding of the water uptake process of roots also the surrounding soil plays an important role, this chapter deals with water dynamics in soil. The methods used in this context are 1D and 2D NMR diffusion methods without spatial resolution.

8.2.1. Experimental setup for 1D and 2D diffusion measurements

One- and two-dimensional diffusion experiments were performed on a natural sand column saturated with water. Figure 8.12 shows the experimental setup for diffusion measurements on the sand column.

The sand column was completely saturated with water with 0.1 wt-% $CuSO_4$. The reservoir drawn in Figure 8.12 was filled with water with 0.1 wt-% $CuSO_4$ to ensure water saturation throughout the NMR experiments. The coordinate system in Figure 8.1 indicates the PFG directions.

8.2.2. The influence of internal field gradients on the 1D diffusion determination

Understanding general water motion in natural porous media is essential for the investigation of water motion in natural soil. Therefore, investigations of both diffusion/dispersion and flow were done in well known model soil such as natural sand.

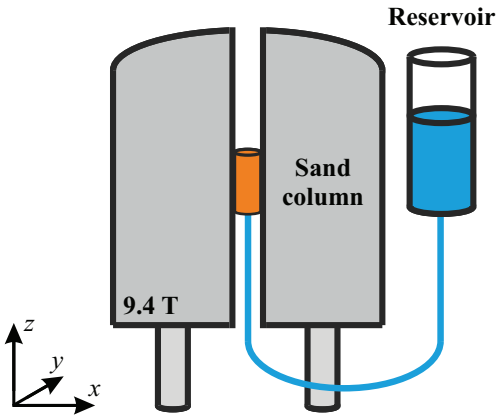

Figure 8.12: *Experimental setup for one- and two-dimensional diffusion measurements on natural sand. A reservoir ensures the water saturation of the entire sand column.*

Stingaciu et al. [SPB09] indicated that internal field gradients influence the NMR signal when determining pore size distributions of natural sand. Therefore, common stimulated echo is directly compared with the 13-interval pulse sequence in the following. Figure 8.13 shows the NMR signal attenuation of a natural sand column entirely saturated with water containing 0.1 wt-% $CuSO_4$ for the determination of the diffusion coefficient. This salt was added to avoid growth of bacteria and algae, as well as to reduce the measurement time. The measurement time strongly depends on the relaxation time T_1, which is reduced by a factor of five compared to T_1 relaxation of pure water resulting from the added paramagnetic ions (T_1 of water with 0.1 wt-% $CuSO_4$ without sand: (0.30 ± 0.02) s). Due to the reduced T_1 relaxation time, also T_2 of water containing 0.1 wt-% $CuSO_4$ without sand was decreased to a value of $T_2 = (0.20 \pm 0.03)$ s.

Figure 8.13 presents the NMR signal intensity in diffusion measurements in x direction (black filled symbols) as well as in y direction (red framed symbols). Squares indicate the common PFG pulse sequence, while triangles represents the 13-interval PFG pulse sequence. The data for the two directions match very well. This indicates isotropic diffusion of water in the sand column.

All one-dimensional diffusion measurements were performed with an observation time of $\Delta = 100$ ms. Due to a long phase cycle of the 13-interval pulse sequence, 32 repetitions of the 13-interval pulse sequence were acquired. To match this with the

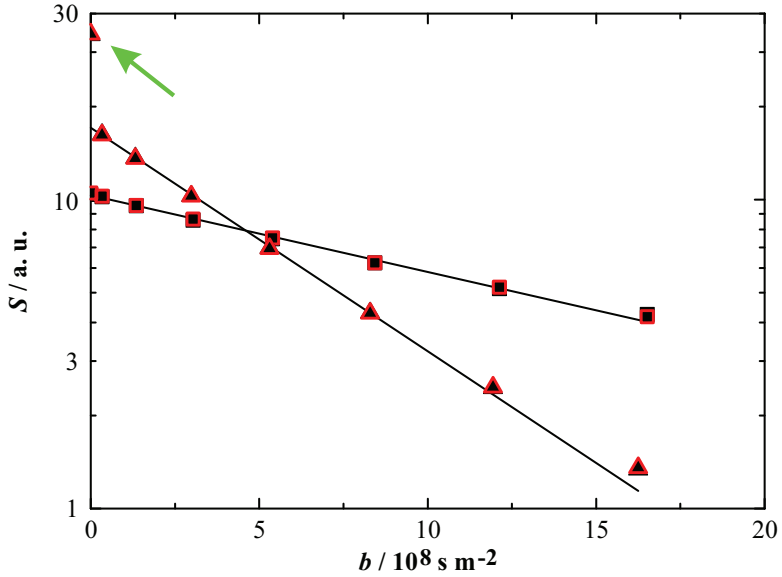

Figure 8.13: *Comparison of common stimulated echo pulse sequence (squares) with the 13-interval pulse sequence (triangles) on a water saturated sand column. Presented are diffusion measurements for both pulse sequences in x direction (black filled symbols) as well as in y direction (red framed symbols). The measurements in x direction are fitted with a mono-exponential decay for both pulse sequences (black lines). Stimulated echo: $TR = 1500.0\,ms$, $\tau = 2.4\,ms$, number of scans: 4, PFG steps: 8, $G_{max} = 0.401\,T\,m^{-1}$, $\delta = 1.0\,ms$, $\Delta = 100.0\,ms$, measurement time: 48 s. 13-interval stimulated echo: $TR = 1500.0\,ms$, $\tau = 3.4\,ms$, number of scans: 32, PFG steps: 8, $G_{max} = 0.201\,T\,m^{-1}$, $\delta = 1.0\,ms$, $\Delta = 100.0\,ms$, measurement time: 6 min 24 s.*

common PFG pulse sequence where only four repetitions were required, the signal amplitude of the 13-interval sequence was divided by eight. The intervals τ of both sequences are different with a higher value for the 13-interval PFG pulse sequence. Thus, T_2 relaxation had a stronger effect on the signal in the 13-interval sequence. However, the signal improvement from suppression of the cross term $A_c(t_e)$ is still remarkable.

At $b = 0$ in the 13-interval PFG pulse sequence, the desired echo overlaps with additional echoes resulting from the "spin echo" pulse sequence (zero PFGs amplitudes) in the reading interval. This interference artificially enhances the initial signal (green arrow in Figure 8.13), thus this data point is not considered for determining the diffusion coefficient.

The suppression of the cross term $A_c(t_e)$ between applied PFGs and internal gradients has two effects. First, the signal amplitude is increased. Second, the decay of the signal with increasing b-value is stronger. In logarithmic scale the decay is a straight line, if diffusion underlies only one diffusive process. The data can be fitted with a mono-exponential function described by Eq. (5.34). Since the respective signal decays in x and y direction of both pulse sequences are identical, Figure 8.13 only presents the fit in x direction (black lines for both pulse sequences) with the fitted diffusion coefficients given in Table 8.2.

Table 8.2: *Diffusion coefficients resulting from fitted 1D NMR diffusion experiments.*

Pulse sequence	$D_x \,/\, 10^{-9}\ \mathrm{m^2\,s^{-1}}$	$D_y \,/\, 10^{-9}\ \mathrm{m^2\,s^{-1}}$
PFG stimulated echo	(0.57 ± 0.04)	(0.58 ± 0.04)
13-interval PFG stimulated echo	(1.67 ± 0.07)	(1.66 ± 0.07)

The values for x and y direction match very well. Since the mono-exponential decay fits to the measurement data, in first approximation the water diffusion in the sand column can be assumed isotropic at least in these two directions. The diffusion coefficients determined with the 13-interval pulse sequence are around three times higher than those from the common PFG stimulated echo pulse sequence. This is attributed to the cross term suppression. Thereby, the diffusion coefficients determined by the 13-interval pulse sequence are almost in the range of free diffusion in water. From the observation time $\Delta = 100\,\mathrm{ms}$ and the diffusion coefficient of pure water, the mean displacement can be calculated to $|\boldsymbol{R}| = 37\,\mu\mathrm{m}$ (Eq. (3.8)). The mean displacement compares well to the average pore radius of around $40\,\mu\mathrm{m}$ in this type of natural sand. It can therefore be assumed that the movement of the molecules is restricted by the grains of sand. This explains the observed reduced diffusion coefficient with the 13-interval pulse sequence.

The one-dimensional experiments presented in this section show that the influence of internal field gradients on the NMR signal is not negligible. From these results it is recommended to use a 13-interval pulse sequence as a basis for any PFG investigations on natural porous media.

8.2.3. 2D investigations of diffusion behavior in natural sand

The comparison of the two pulse sequences can only prove macroscopic isotropy of the sand. To identify potential microscopic anisotropy, correlation measurements are required (Chapter 5.2). Since the T_2 relaxation time of natural sand is very short, the pulse sequence sDDCOSY (Chapter 6.1.1), based on the common PFG stimulated echo pulse sequence (see Figure 6.1), is more convenient for investigating diffusion correlations. Instead of applying the diffusion-encoding PFGs in different directions successively, they were applied simultaneously. This leads to a shortening of the pulse sequence by a factor of two, which especially reduces the influence of T_2 relaxation.

Even knowing that the common PFG stimulated echo pulse sequence underestimates diffusion coefficients (Chapter 8.2.2), both measurements can be used to compare the diffusion coefficients. Therefore, the following considerations are done to validate the pulse sequence sDDCOSY. The criterion for successful validation is that the diffusion coefficients from sDDCOSY are in the same range as those resulted from one-dimensional measurements.

Since the sand column is macroscopically isotropic, sDDCOSY delivers the same diffusion coefficient distribution with any pair of investigated directions (x and y, x and z, or y and z). Therefore, only the pair x and y is considered in the following. Figure 8.14 shows the map of the distribution obtained from the NMR data after an inverse Laplace transformation (Chapter 7.1.1).

The intensity in the map is a measure for the probability to find this diffusion coefficient in the sample. The map contains one main peak on the diagonal with high intensity. Another peak on the diagonal with low intensity and very low diffusion coefficient (white arrow) results from the noise of the NMR measurement and can therefore be neglected. Thus, most of the water molecules inside the sand column have the same diffusion tensor corresponding to the strong peak, independent of the observation direction.

For a more quantitative analysis, in the following the diffusion coefficients obtained from the diffusion correlation map are compared to the results from 1D PFG measurements presented in Chapter 8.2.2. Thereby, one has to consider that the results from this pulse sequences are significantly influenced by internal field gradients. Thus, the diffusion coefficients presented here only serve to show the similarity to 1D PFG measurements. This still proves the suitability of sDDCOSY to determine

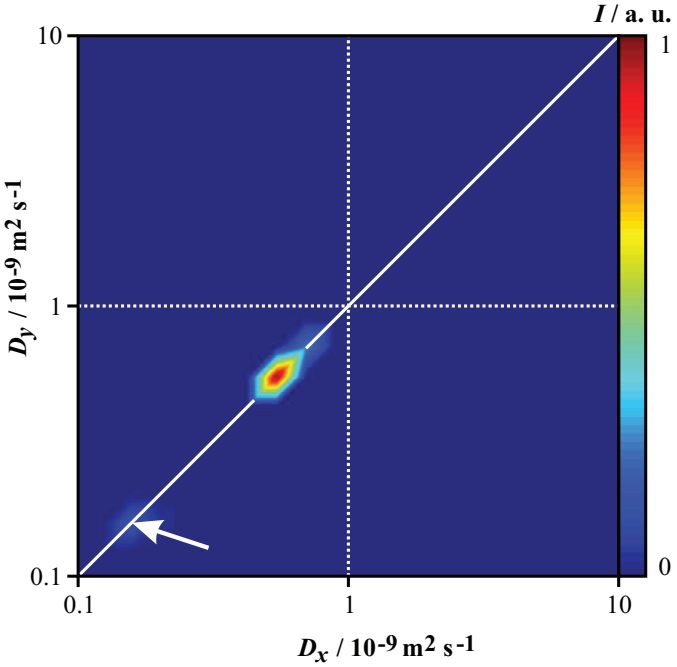

Figure 8.14: *Map of the diffusion coefficient distribution of water in natural sand measured with sDDCOSY (Chapter 6.1.1). The map shows the correlated diffusion coefficients of the x and y direction. The white diagonal represents equal diffusion in both investigated directions. The magnitude I of diffusion correlations is given in arbitrary units. $TR = 1500.0\,ms$, $\tau = 3.0\,ms$, number of scans: 4, PFG steps: 20×20, $G_{max} = 0.883\,T\,m^{-1}$, $\delta = 1.8\,ms$, $\Delta = 70.0\,ms$, measurement time: 40 min.*

diffusion correlations, independent on the accuracy.

From Figure 8.14 the following diffusion coefficients are read:

$$D_x = (0.57 \pm 0.07)\,10^{-9}\,\mathrm{m^2\,s^{-1}},$$
$$D_y = (0.57 \pm 0.07)\,10^{-9}\,\mathrm{m^2\,s^{-1}}.$$

The absolute values of these diffusion coefficients are not correct but influenced by internal field gradients. However, the values match very well with the diffusion coefficients obtained with 1D PFG measurements (Table 8.2). This proves that sDDCOSY is capable to measure diffusion coefficients and their correlation.

As already shown with one-dimensional diffusion measurements, the NMR signal of water molecules in natural sand is significantly influenced by internal field gradi-

ents. Therefore, the sDDCOSY pulse sequence was combined with the 13-interval pulse sequence (Chapter 6.1.2) to suppress the cross term $A_c(t_e)$. Thus, Figure 8.15 shows the diffusion correlation map measured by this newly 13-interval sDDCOSY pulse sequence in x and y direction.

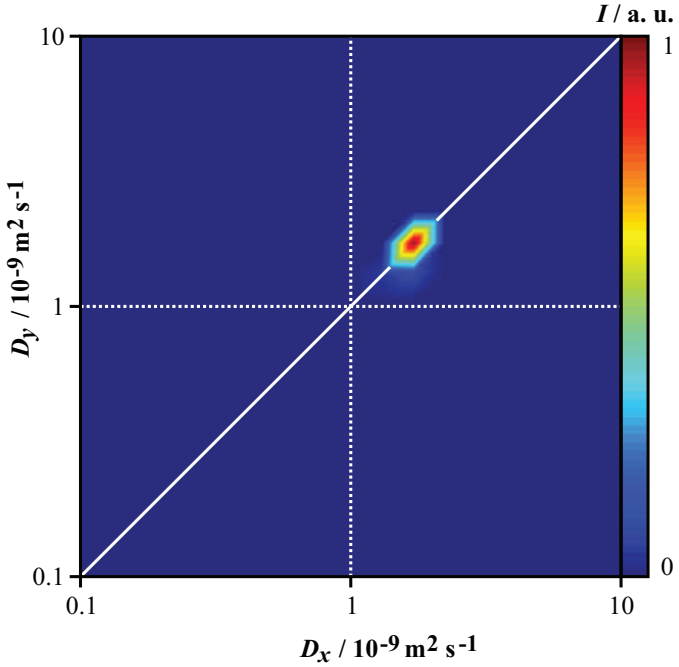

Figure 8.15: *Map of water diffusion coefficients in natural sand measured with 13-interval sDDCOSY (Chapter 6.1.2), which reduces influences of internal field gradients on the NMR signal. Plotted are the correlated diffusion coefficients of the x and y direction. The white continuous line indicates the diagonal. The color bar gives the magnitude I of diffusion correlations in arbitrary units. $TR = 1500.0\,ms$, $\tau = 3.2\,ms$, number of scans: 32, PFG steps: 20×20, $G_{max} = 0.312\,T\,m^{-1}$, $\delta = 1.0\,ms$, $\Delta = 70.0\,ms$, measurement time: 5 h 20 min.*

Figure 8.15 contains only one strong signal peak on the diagonal, whereas no noise peak at small diffusion coefficients exists. The observation time was the same during 13-interval sDDCOSY and sDDCOSY measurements. According to the diffusion

correlation map, D_x and D_y are equal:

$$D_x = (1.68 \pm 0.12)\, 10^{-9}\, \mathrm{m^2\, s^{-1}},$$
$$D_y = (1.68 \pm 0.12)\, 10^{-9}\, \mathrm{m^2\, s^{-1}}.$$

Furthermore, these values match almost perfectly with the diffusion coefficients determined by the 1D 13-interval PFG pulse sequence. The smaller diffusion coefficients compared to free diffusion result from restricted diffusion in the pores as already discussed in Chapter 8.2.2. These results show that even with 13-interval sDDCOSY it is possible to reduce influences of internal field gradients on the NMR signal. Therefore, this newly developed pulse sequence allows studying diffusion correlations under both short T_2 relaxation times and influences of internal field gradients. Since the influence of internal field gradients is reduced, diffusion correlation experiments can now also be discussed quantitatively.

8.3. Velocity imaging in natural sand

8.3.1. Experimental setup for flow investigations on natural sand

For flow investigations water with 0.1 wt-% $CuSO_4$ was pumped through a sand column. In Figure 8.16 a sketch of the experimental setup for flow investigations is shown.

Similar to Chapter 8.2.1, Reservoir 1 ensures saturation of the sand column with water with 0.1 wt-% $CuSO_4$. A peristaltic pump with variable applied volume flow allowed to induce different pore flow velocities to the sand column. The main flow direction inside the sand was vertical (z direction, see Figure 8.16), antiparallel to the static field. An additional reservoir was included in the setup right after the peristaltic pump to compensate flow fluctuations from the pump (Reservoir 2). Without rearranging the whole setup or repacking of the sand inside the column the experiments started at high applied pore flow velocities. Then, the flow was reduced stepwise until the detection limit of the flow imaging signal was reached.

To determine the applied pore flow velocities v_{appl} the volume flow J_{appl} was measured gravimetrically at each adjustment of the peristaltic pump, independent of NMR velocity mapping. From the measured volume flows the pore flow velocities

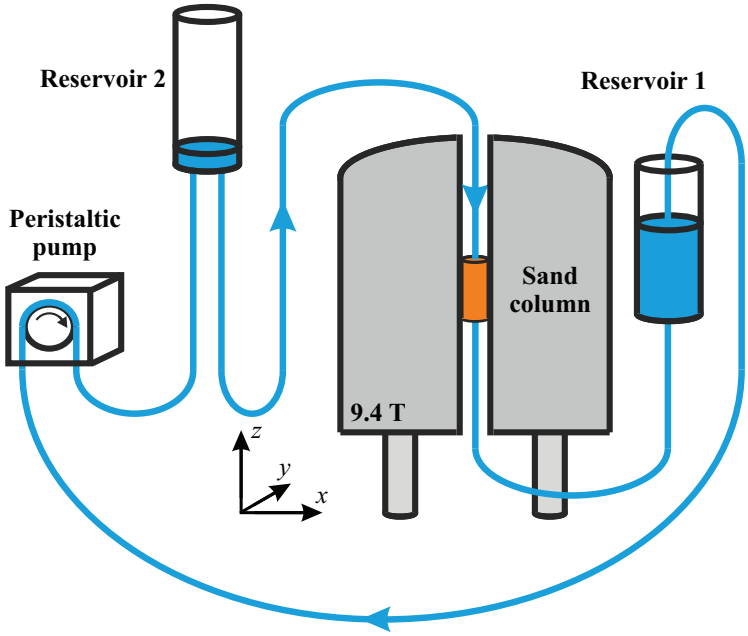

Figure 8.16: *Experimental setup for velocity mapping of water flow through natural sand. Variable volume flow in z direction is induced by the peristaltic pump. Reservoir 1 ensures water saturation of the sand column, Reservoir 2 compensates flow fluctuations from the pump.*

were calculated using the cross-sectional area $A = \pi\,(d_\mathrm{i}/2)^2$ of the sand column and the water content θ according to

$$v_\mathrm{appl} = \frac{J_\mathrm{appl}}{\theta\, A}. \tag{8.2}$$

The applied pore flow velocities ranged from a maximum of $v_\mathrm{appl,max} = 1.35\,\mathrm{mm\,s^{-1}}$ down to the minimum detectable flow velocity of $v_\mathrm{appl,min} = 0.06\,\mathrm{mm\,s^{-1}}$. The lowest applied pore flow velocity was $v_\mathrm{appl,0} = 0.02\,\mathrm{mm\,s^{-1}}$.

Two different types of experiments were performed to investigate flow through the sand column. In first experiments the limit of detectable velocities with the 13-interval STEMSI pulse sequence was investigated. Therefore, the volume flow of the peristaltic pump was reduced stepwise.

In further experiments, the applied pore flow velocity given by the pump was kept constant. Instead, the observation time Δ in the 13-interval STEMSI pulse sequence

was varied.

Imaging was orientated perpendicular to the axis of the sand column to get cross-sectional velocity maps. Thus, the slice was selected in z direction with the gradients for spatial resolution applied in x and y direction.

8.3.2. Velocity mapping on flow in natural sand

Firstly, flow encoded MR images were recorded with the highest applied pore flow velocity of $v_{\mathrm{appl,max}} = 1.35\,\mathrm{mm\,s^{-1}}$. These measurements served for checking the operational capability of the 13-interval STEMSI pulse sequence for velocity mapping in natural porous media, which contain internal field gradients influencing the NMR signal. In each direction perpendicular (x and y direction) and parallel (z direction) to the induced water flow direction, flow encoded NMR images were measured. Since the flow was applied in z direction it was expected that the average velocity under parallel flow-encoding deviates from zero. However, the average velocity under perpendicular flow-encoding should be zero with a non-vanishing standard deviation. According to this assumption, these fluctuations around zero velocity result from the motion of water molecules around the sand grains which act as barriers against the applied flow. For a more analytical description, the velocity maps and 1D mean velocity profiles are shown in Figure 8.17 for parallel (z direction) and perpendicular (x direction) flow-encoding. Note that for the 1D velocity profiles the velocities in one image direction (y direction) have been averaged while the spatial resolution was still kept in the other image direction (x direction).

The left column of Figure 8.17 shows the velocity map of flow-encoding in z direction (top) and the according 1D mean velocity profile spatially resolved in x direction (bottom). The velocity map (Figure 8.17 top left) is very homogeneous over the cross-sectional slice of the sand column with a clearly visible offset from zero velocity. The velocity increases sharply at the rim of the sand tube with respect to outside the tube. The 1D mean velocity profile (Figure 8.17 bottom left) supports this observation and averages out some of the fluctuations of the single pixels at least in one imaging direction. Despite remaining fluctuations, which are much smaller than the offset from zero velocity, the mean velocity profile clearly takes positive values.

The right hand side of Figure 8.17 shows the velocity map (top) and the 1D mean velocity profile (bottom) of flow-encoding perpendicular to the induced water flow.

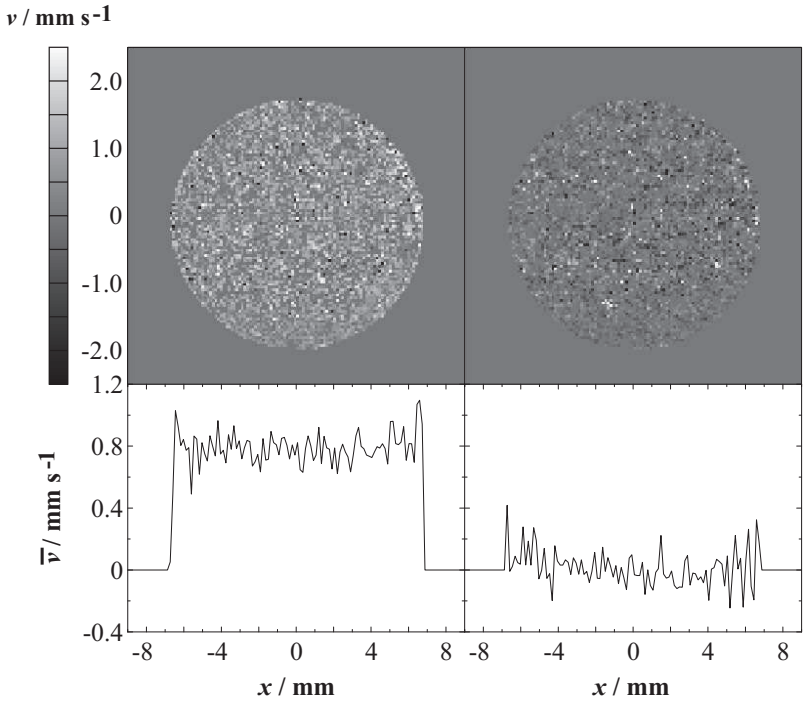

Figure 8.17: *Velocity maps (top) and 1D mean velocity profiles averaged along y direction (bottom) at the highest applied pore velocity of* $v_{\mathrm{appl,max}} = 1.35\ mm\ s^{-1}$ *using the pulse sequence 13-interval STEMSI. Shown are the results of flow-encoding parallel (z direction, left) and perpendicular (x direction, right) to the induced water flow direction in z direction (into the sheet plane). TR =* $2000.0\,ms$*, τ =* $2.3\,ms$*, FOV:* $18.0{\times}18.0\,mm^2$*, matrix size:* $128{\times}128$ *pixels resulting in a resolution of* $140\,\mu m\,pixel^{-1}$*, number of scans: 32, number of slices: 4, slice thickness:* $1.0\,mm$*,* $G = 0.345\,T\,m^{-1}$*,* $\delta = 0.3\,ms$*,* $\Delta = 17.0\,ms$*, measurement time for one velocity map: 4 h 33 min 4 s. After each decrease of the applied flow velocity, the experiment was interrupted for 24 h to ensure the lower water flow was in equilibrium.*

In contrast to velocity mapping parallel to the induced water flow (Figure 8.17 top left), no significant trend of positive or negative velocities is seen (Figure 8.17 top right). Also the 1D mean velocity profile (Figure 8.17 bottom right) fluctuates both positively and negatively around zero, with an average of zero. This confirms the above stated assumption of a net zero velocity perpendicular to the induced water flow. The measuring accuracy in each pixel was 5 % of the velocity. However, the mean velocities in both profiles show higher fluctuations. Especially in the range of

$x = [-4; 4]$, where the mean value calculation is done over a representative amount of pixels, the fluctuations around the mean value are the same both for parallel and perpendicular flow-encoding measurements (around 15 %). Since the variations are independent of the observation direction it is likely that the origin is water molecule motion around the randomly oriented sand grains. The observations at both parallel and perpendicular flow-encoding measurements prove the reliability of the 13-interval STEMSI pulse sequence in natural porous media influenced by internal field gradients.

Now, the applied pore flow velocity was reduced in five steps down to a lowest value of $v_{\mathrm{appl},0} = 0.02\,\mathrm{mm\,s^{-1}}$. At this low velocity, differences between the velocity maps of parallel and perpendicular flow-encoding were no longer observable (data not shown). The lowest applied flow velocity where still differences between the observation directions were detected was $v_{\mathrm{appl,min}} = 0.06\,\mathrm{mm\,s^{-1}}$. The velocity maps and the 1D velocity profiles of this experiment are shown in Figure 8.18.

Compared to Figure 8.17 the maximum detected velocity is reduced according to the lower applied pore flow velocity. Therefore, note the different scales of the velocity axes. Still, there is an obvious mean positive velocity parallel to the induced water flow (Figure 8.18 top left). The velocity distribution of the cross-sectional slice of the sand column is still homogeneous. In the 1D mean velocity profile (Figure 8.18 bottom left) the fluctuations are again small compared to the mean velocity values. Thus, also at this low applied velocity detection of flow was possible. Similar to Figure 8.17 right, the flow encoded perpendicular to the induced water scatters both in the velocity map (Figure 8.18 top right) and the 1D mean velocity profile (Figure 8.18 bottom right) around zero due to water molecule motions around the sand grains. This also results in a net zero velocity flow averaged over the entire selected cross-sectional slice. Again the fluctuations in the mean velocity profiles are independent of the direction of flow-encoding. The fluctuations are again about 15 % of the mean velocity, independent of the direction. The linear dependence of the velocity fluctuations on the applied pore flow velocity indicates that the water movement around barriers such as sand grains depends on the applied pore flow velocity.

For a quantitative analysis, in Figure 8.19 is shown the velocity distribution at the highest applied pore flow velocity $v_{\mathrm{appl,max}} = 1.35\,\mathrm{mm\,s^{-1}}$, given as a histogram (black rectangles) taking all pixels of the the sand column slide into account.

A Gaussian function with a mean velocity of $v_{\mathrm{Gauss}} = (0.81 \pm 0.01)\,\mathrm{mm\,s^{-1}}$ and

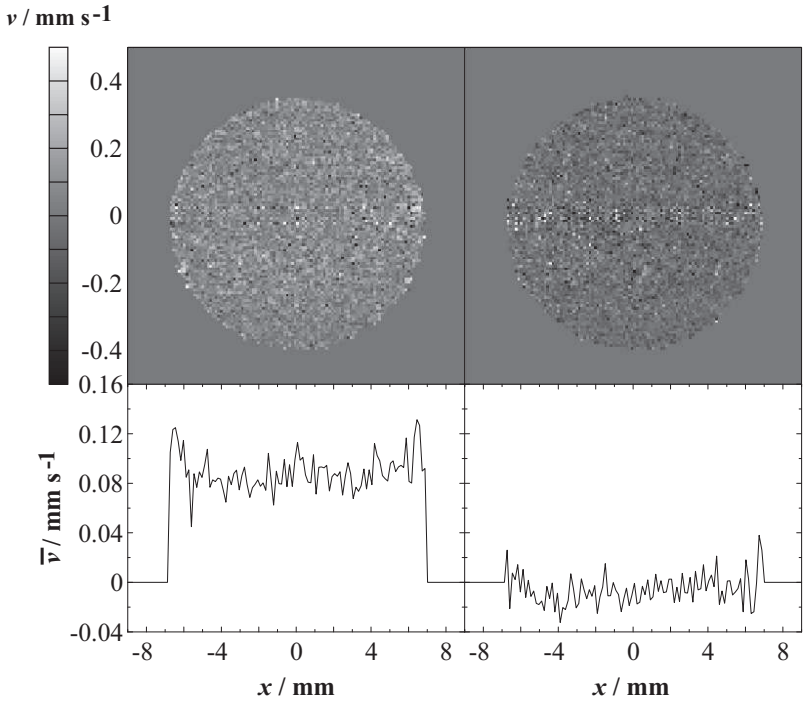

Figure 8.18: *Velocity maps (top) and 1D mean velocity profiles averaged along y direction (bottom) of the lowest applied pore velocity of* $v_{\mathrm{appl,min}} = 0.06\ mm\ s^{-1}$*, where flow was still detectable, using the pulse sequence 13-interval STEMSI. Shown are the results of flow-encoding parallel (z direction, left) and perpendicular (x direction, right) to the induced water flow direction in z direction (into the sheet plane). Note the different ranges in the velocity scales compared to Figure 8.17.* $TR = 2000.0\,ms$*,* $\tau = 2.3\,ms$*, FOV:* $18.0{\times}18.0\,mm^2$*, matrix size:* $128{\times}128$ *pixels resulting in a resolution of* $140\,\mu m\,pixel^{-1}$*, number of scans: 32, number of slices: 4, slice thickness:* $1.0\,mm$*,* $G = 0.921\,T\,m^{-1}$*,* $\delta = 0.3\,ms$*,* $\Delta = 17.0\,ms$*, measurement time for one velocity map: 4 h 33 min 4 s.*

a standard deviation of $\sigma_{\mathrm{Gauss}} = (0.47 \pm 0.01)\,\mathrm{mm\,s^{-1}}$ fits well to the experimental data. The mean MRI velocity in this slide is $v_{\mathrm{MRI}} = (0.78 \pm 0.05)\,\mathrm{mm\,s^{-1}}$. This is within its uncertainty in good accordance with the fitted Gaussian mean velocity. The distribution of the experimental data is symmetric around its mean value, with a clear positive offset from zero. Since the standard deviation of the velocity distribution is larger than the offset, also negative velocities have been measured. This is reasonable since water flows locally around barriers such as sand grains.

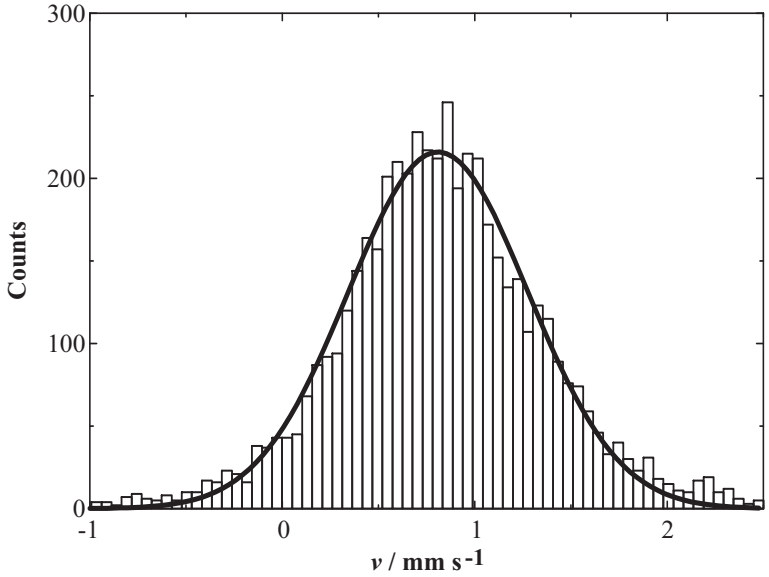

Figure 8.19: *Histogram of the NMR detected pore flow velocity distribution in the velocity map of the highest applied pore flow velocity of* $v_{\mathrm{appl,max}} = 1.35\ mm\ s^{-1}$ *(rectangles). A Gaussian function is fitted to the data (line).*

The distribution of measured velocities can be fitted for all applied velocities with Gaussian functions such as shown in Figure 8.19. In each measurement, the velocities are distributed symmetrically around the mean value even at the tails. The standard deviation σ of the Gaussian fits increases with the applied pore flow velocity. Figure 8.20 shows this dependence (triangles) and a linear fit to the data (black line).

The fitted line is described by $\sigma = (0.27 \pm 0.01) \times v_{\mathrm{appl}} + (0.07 \pm 0.01)\,\mathrm{mm\,s^{-1}}$. The data and the linear relation in Figure 8.20 were found for the flow-encoding measurements parallel to the applied flow direction (z direction). Interestingly, also perpendicular to the flow-encoding directions (x and y direction) the standard deviation grows with the applied pore flow velocity and the linear fit is the same. The only difference between the measurements is that in the perpendicular case, the velocity distribution has a mean value of zero, while in the parallel case the mean velocity is positive.

In order to assess the mean pore flow velocity values obtained from NMR flow imaging, also water with 0.1 wt-% $CuSO_4$ flowing through a reference tube was mea-

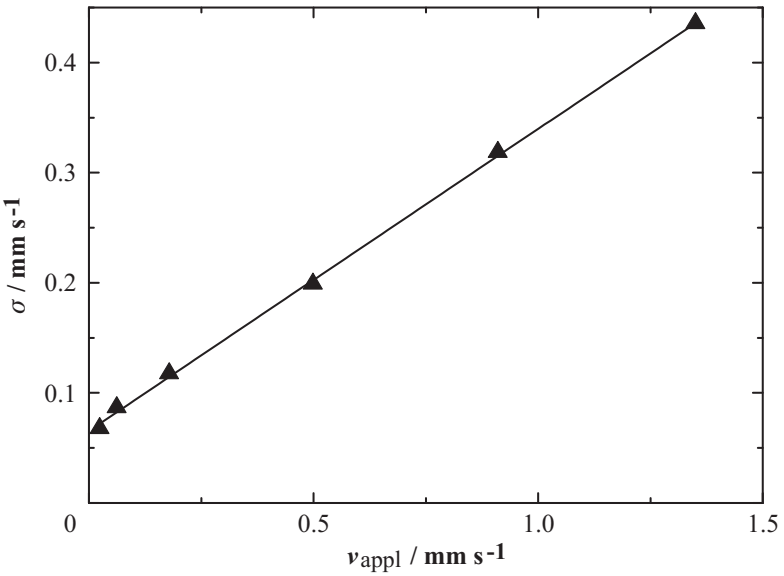

Figure 8.20: *Plot of dependency of the width of velocity distribution fitted with Gaussian function from the applied pore flow velocity (triangles). A linear relationship is fitted to the data (line).*

sured. At each applied pore flow velocity, the detected velocities were averaged over all pixels to obtain the mean velocity of the slice. If detected and applied velocity are proportional, no additional linear effects take place. Ideally the proportional constant is unity so that no additional correction has to be applied. This would also prove a constant pressure in the experimental setup. The result of these measurements is plotted as the black dots in Figure 8.21.

As seen from the figure, the relationship between the NMR calibration data and the applied velocities is indeed linear with a fit equation of $v = (1.01 \pm 0.01) \times v_{\mathrm{appl}}$ No additional scaling factor between the measured and applied velocity is needed. This holds even for very high applied velocities. Note that the relationship is different, if water flows through the sand column (black triangles in Figure 8.21). At low applied pore flow velocities the detected mean pore flow velocity matches with the applied value. However, with higher applied pore flow velocities an increasing underestimation of the applied values is observed.

Currently, there is a lack of thorough understanding this effect, but there are several hints to an explanation of this phenomenon.

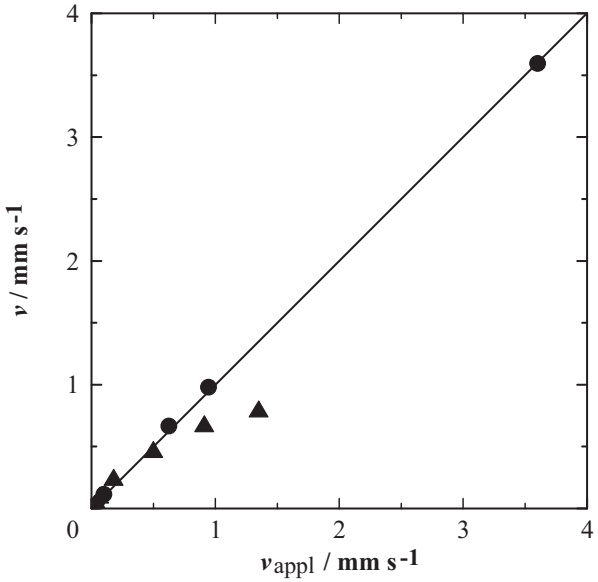

Figure 8.21: *Comparison of the applied pore flow velocity and the experimental determined mean pore flow velocity, averaged over the entire velocity map detected with the pulse sequence 13-interval STEMSI. Shown are measurements of the flow of water with 0.1 wt-% $CuSO_4$ through a simple tube (dots) for calibration and through the sand column (triangles). The black line is a linear fit to the mean velocities of the calibration measurement through the tube.*

First, since the experimental setup was completely closed and not exposed to evaporation, water loss through leakage or evaporation can be excluded. This assumption is proved by the calibration measurement, which was done at the same conditions as velocity mapping of the sand column. Only the sample itself has changed.

Second, it cannot be seen that the reduction only affects high velocities in the velocity distributions. If this would be the case, the velocity distribution shown in the histogram (Figure 8.19) would tend to be asymmetric at the tails of the distribution. Rather, the entire velocity distribution is shifted to a lower mean pore flow velocity.

Third, phase shifts of $\Delta\phi > 2\pi$ caused by too strong gradient pulses according to the appearing velocities in the sand column can be excluded, since again the velocity distribution would not be symmetric but much more pixels would have a smaller

velocity than the mean value. In consequence, a cut off would appear in the velocity distribution at higher pore flow velocities. Nevertheless, especially at low applied velocities the determined and the applied mean pore flow velocities match very well.

To understand the deviation of detected and applied pore flow velocities at high flows, the signal intensity maps and the according 1D mean intensity profiles of the 13-interval STEMSI measurements are discussed using Figure 8.22. Note that for the 1D profiles the signal intensity in one image direction (y direction) has been averaged, keeping the spatial resolution in the other image direction (x direction).

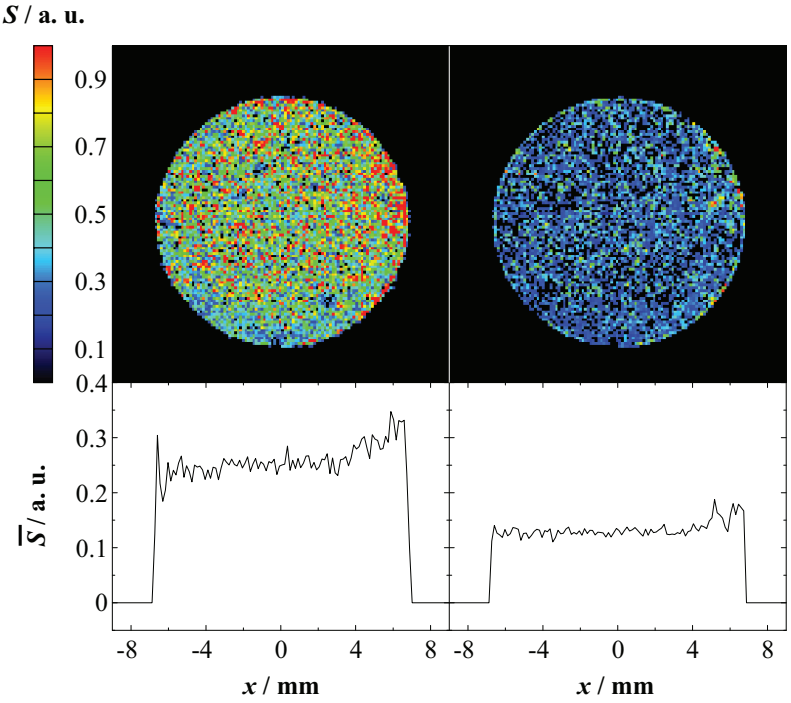

Figure 8.22: *Intensity maps (top) and 1D mean intensity profiles averaged along y direction (bottom) of the lowest NMR detectable applied pore flow velocity of* $v_{\mathrm{appl,min}} = 0.06\,\mathrm{mm\,s^{-1}}$ *(left), and the highest applied pore velocity* $v_{\mathrm{appl,max}} = 1.35\,\mathrm{mm\,s^{-1}}$ *(right) using the pulse sequence 13-interval STEMSI.*

The intensity map measured with the lowest detectable applied pore flow velocity of $v_{\mathrm{appl,min}} = 0.06\,\mathrm{mm\,s^{-1}}$ (Figure 8.22 top left) is homogeneous with a slight signal increase on the right boundary of the sand column. This is also seen in the intensity profile (Figure 8.22 bottom left), where the fluctuations around the mean signal

intensity are small compared to the offset from zero. The intensity map measured with the highest applied pore flow velocity of $v_{\mathrm{appl,max}} = 1.35\,\mathrm{mm\,s^{-1}}$ (Figure 8.22 top right) shows sharply decreased values. The signal loss is also seen in the intensity profile (Figure 8.22 bottom right). The map is still homogeneous and shows again slightly higher signal on the right boundary of the sand column. Still the fluctuations are small compared to the offset from zero. The signal fluctuations are independent of the applied pore flow velocity since their relative size of around 10 % stays constant. However, the mean signal intensity of the highest applied pore flow velocity decreased by half compared to the lowest NMR detectable applied pore flow velocity.

For a more quantitative analysis of the signal dependence from the applied pore flow velocity Figure 8.23 shows all mean signal intensities detected with NMR velocity mapping versus the applied pore flow velocity.

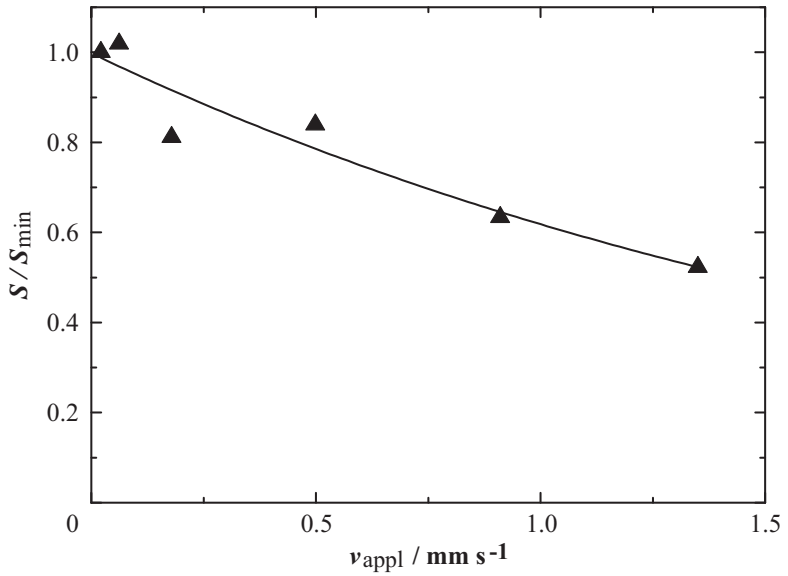

Figure 8.23: *Plot of the dependency of signal intensity integrated over the entire selected slice from the applied pore flow velocity (triangles). The intensity is normalized to the integrated intensity of the lowest applied pore flow velocity of* $v_{\mathrm{appl},0} = 0.02\ mm\ s^{-1}$. *The data are fitted with an exponential decay (line).*

The data points were calculated by integrating the signal intensity of all pixels in the selected slice for each flow-encoding measurement, followed by normaliza-

tion with the integrated signal intensity of the lowest applied pore flow velocity of $v_{\mathrm{appl},0} = 0.02\,\mathrm{mm\,s^{-1}}$. A decay of the integrated signal intensity with increasing applied flow velocity can be clearly seen. An exponential decay (line in Figure 8.23) was fitted to the presented data points.

Thus, even with the pulse sequence 13-interval STEMSI, which reduces influences of internal field gradients to the NMR signal, there is still a loss of intensity with increasing applied pore flow velocity detectable. Therefore, in the following possible reasons following Eq. (5.50) for the NMR signal decay are discussed, which also might be reasons for deviations of the detected mean pore flow velocities from their expected value at high applied flow velocities. Equation (5.50) describes the measured intensity, taking into account the influences of diffusion and flow effects.

T_2 relaxation impacts on the signal during the four time intervals τ shown in the pulse sequence, Figure 6.3. During the long storage time Δ', when the magnetization is stored along the z direction, no T_2 relaxation occurs. The magnetization is only influenced by T_1 relaxation. Since the time τ between the 90° and 180° pulses was always kept at the same value and assuming velocity independent T_2 relaxation, the influence of pure T_2 relaxation on the detected signal was the same, independent of the applied pore flow velocity. Note that this statement was not experimentally verified.

The discussed intensity maps (Figure 8.22) and values of the integrated intensities at different applied pore flow velocities (Figure 8.23) were taken from experiments without external flow-encoding gradients ($\boldsymbol{G}(t) = 0$). That means, according to Eq. (5.50) there is only a diffusive contribution from internal gradients $\boldsymbol{g}(t)$ expressed in the term $A_i(t_\mathrm{e})$. Furthermore, it was assumed that the internal gradients do not depend on the applied pore flow velocity.

Since integrative measurements of T_1 relaxation time and the diffusion coefficient before and after flow experiments result in the same values, changes in the grain packaging in the sand column at different applied pore flow velocities can be excluded. With starting the measurements at high applied pore flow velocities, the sand packaging should not change in subsequent measurements at lower velocities.

Another reason for signal loss can be relaxation behaving such as T_1 relaxation. Since faster water molecules travel a longer distance during the observation time Δ, they have more collisions with sand grains. In consequence, relaxation to the equilibrium state with zero excitated magnetization is more probable for molecules with higher velocities.

In order to prove this assumption additional flow investigations had been undertaken. In these measurements the applied pore flow velocity was kept constant at the highest value of $v_{\mathrm{appl,max}} = 1.35\,\mathrm{mm\,s^{-1}}$. Instead, the observation time was varied in the range from $\Delta_{\mathrm{min}} = 9\,\mathrm{ms}$ up to $\Delta_{\mathrm{max}} = 50\,\mathrm{ms}$. Note that τ was also kept constant in these measurements. Therefore, there was only a constant influence of T_2 relaxation, independent of the observation time Δ. The only time interval in which relaxation different from T_2 can occur is during the storage time Δ', when the magnetization is stored along the z direction. The only kinds of relaxation that actually can occur in this case are T_1 relaxation and effects showing similar behavior as T_1 relaxation.

The dependence of the mean pore flow velocity on the observation time Δ is plotted as black triangles in Figure 8.24.

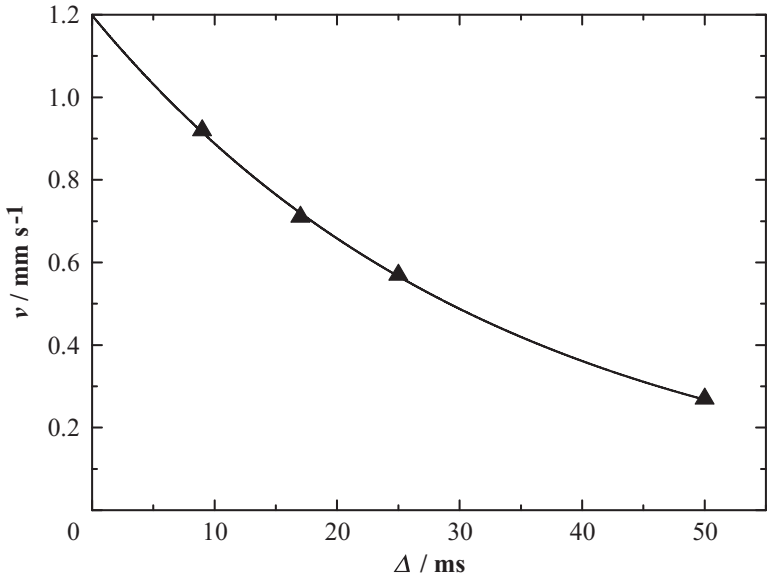

Figure 8.24: *Dependence of the velocity detected with flow-encoding on the observation time Δ at the applied pore flow velocity of $v_{\mathrm{appl,max}} = 1.35\ mm\ s^{-1}$ with 13-interval STEMSI pulse sequence (triangles). An exponential decay is fitted to the data (line). TR = 2000.0 ms, τ = 2.3 ms, FOV: 16.0×16.0 mm², matrix size: 128×8 pixels, number of scans: 32, number of slices: 1, slice thickness: 1.0 mm, $G_{\mathrm{min}} = 0.117\,T\,m^{-1}$ up to $G_{\mathrm{max}} = 0.652\,T\,m^{-1}$, δ = 0.3 ms, Δ_{min} = 9.0 ms up to Δ_{max} = 50.0 ms, measurement time for one velocity map: 17 min 4 s.*

Flow-encoding was done with PFG amplitudes ranging from $G_{\mathrm{min}} = 0.117\,\mathrm{T\,m^{-1}}$

up to $G_{max} = 0.652\,\mathrm{T\,m^{-1}}$ with a pulse duration of $\delta = 0.3\,\mathrm{ms}$. The observation time was varied in the range from $\Delta_{min} = 9\,\mathrm{ms}$ up to $\Delta_{max} = 50\,\mathrm{ms}$.

The mean pore flow velocities, calculated from the experimental data, seem to be influenced by relaxation similar to T_1, since the NMR detected velocities decrease with increasing observation time. The data can be fitted with an exponential decay (black line in Figure 8.24) with a relaxation time of $T' = (33 \pm 3)\,\mathrm{ms}$. Since the T_1 relaxation time of water with 0.1 wt-% $CuSO_4$ in the sand column was $T_1 = (0.23 \pm 0.01)\,\mathrm{s}$, the smaller value of the fitted relaxation time T' has to be explained with additional relaxation effects. Assuming that the velocity at $\Delta = 0\,\mathrm{ms}$ represents the actual mean pore flow velocity in the sample at the applied pore flow velocity, the exponential function was extrapolated to $\Delta = 0\,\mathrm{ms}$. The resulting mean pore flow velocity is $v_{fit} = (1.2 \pm 0.1)\,\mathrm{mm\,s^{-1}}$. This matches satisfactorily with the applied pore flow velocity of $v_{appl,max} = 1.35\,\mathrm{mm\,s^{-1}}$.

With this observed relation between the observation time and the detected mean pore flow velocity it is now possible to correct the velocity map of the highest applied pore flow velocity of $v_{appl,max} = 1.35\,\mathrm{mm\,s^{-1}}$ shown in Figure 8.17. Therefore, each pixel in the velocity map was corrected with the relaxation factor T' resulting from the exponential fit (Figure 8.24 black line). The result of the T' relaxation corrected velocity map at the applied pore flow velocity of $v_{appl,max} = 1.35\,\mathrm{mm\,s^{-1}}$ shows Figure 8.25.

Calculating the mean pore flow velocity of the whole slice results in a mean pore flow velocity of $v_{act,slice} = (1.2 \pm 0.2)\,\mathrm{mm\,s^{-1}}$. This detected mean velocity is close to the applied velocity. Therefore, this confirms the assumption that relaxation similar to T_1 relaxation occurs. However, this relaxation effect decreases with decreasing applied velocity. At low applied pore flow velocities, which are mainly interesting for investigating root water uptake, the effect is very small. Therefore, these investigations showed that NMR using the pulse sequence 13-interval STEMSI is a powerful NMR technique to investigate flow in natural porous media, where the NMR signal is influenced by internal field gradients.

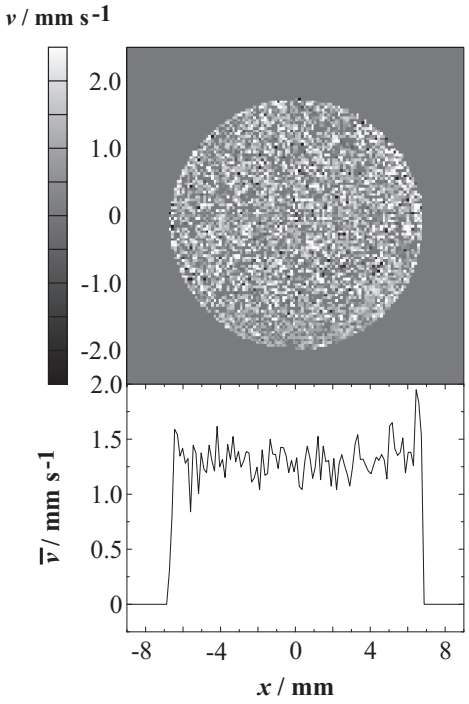

Figure 8.25: *Corrected velocity map of the recorded experimental data with the applied pore flow velocity of* $v_{\mathrm{appl,max}} = 1.35\ mm\ s^{-1}$.

9. Conclusion and outlook

An essential part in understanding root water uptake processes is knowledge about pathways in and hydraulic properties of both soil and plant. This knowledge can be acquired by the detection of water motion in soil and plant roots.

In this thesis two different methods to investigate water motion in natural porous media were presented, both using techniques of nuclear magnetic resonance and magnetic resonance imaging.

On the one hand water motion was investigated indirectly by diffusion measurements. For the reconstruction of a continuous root skeleton diffusion tensor imaging was performed. Root system reconstruction is necessary for model calculations of root water uptake processes. Limits of pure anatomical NMR imaging of reconstructing an entire root skeleton were evaluated. DTI improves these limits by measuring a three-dimensional diffusion tensor in each pixel of a sample. For the determination of diffusion tensors from the NMR data a new approach of data processing was necessary due to the low signal to noise ratio of the NMR signal. The diffusion tensors can be intuitively visualized as colored ellipses pointing into the major diffusion direction. In the end of this process, the reconstruction of an entire single root was possible.

Diffusion measurements were served to assess isotropy of soil. The macroscopic isotropy of a water saturated model soil was tested on natural sand. In one-dimensional diffusion experiments significant influence of internal field gradients on the NMR signal was found. This leads to a loss of signal intensity and therefore to an underestimation of the actual diffusion coefficient. The implementation of a 13-interval pulse sequence worked well in reducing these influences. Internal field gradients had also to be taken into account investigating the microscopic isotropy of the natural sand. Here, diffusion diffusion correlation spectroscopy experiments were performed. To account for internal field gradients, the according NMR pulse sequence was modified in two steps. First, the duration of the pulse sequence was reduced by half for shortening T_2 relaxation effects on the NMR signal, resulting

in the pulse sequence sDDCOSY. Second, sDDCOSY was combined with the 13-interval pulse sequence reducing the influences of internal field gradients. With this new pulse sequence, named 13-interval sDDCOSY, it was possible to prove the microscopic isotropy of the natural sand.

On the other hand, beside the indirect detection of water motion in natural porous media, flow was also observed directly by measuring pore flow velocities of water molecules flowing through natural sand. The internal field gradients do not influence the way to analyze velocity. However, they lead to loss of signal intensity. To avoid this signal loss, in this work an NMR velocity imaging pulse sequence was combined with the concept of the 13-interval pulse sequence. It was possible to detect pore flow velocities as low as $60\,\mu\mathrm{m\,s^{-1}}$ with this new 13-interval stimulated echo multi slice imaging (13-interval STEMSI) pulse sequence. This is a velocity expectable in natural soil. It was the first time that such low velocities were detected directly with NMR. For higher pore flow velocities a deviation of the velocity obtained by NMR from the actual applied velocities was found. Experiments aimed on investigating this deviation showed influences of processes behaving as T_1 relaxation on the detected velocities. Therefore, it was possible to analytically correct the MRI measured pore flow velocities according to this effect.

Outlook

The results presented in this thesis are small but important steps on understanding the root water uptake process. Further investigations can continue in future based on the results in this work. The application of direct velocity imaging with the 13-interval STEMSI pulse sequence on soil surrounding roots will inform about water velocities as well as flow directions. In combination with DTI this opens the possibility to directly observe of water motion directions in close vicinity to plant roots. This will provide parameters of the hydraulic conductivity between soil and roots, important for model calculations of root water uptake processes.

Furthermore, both techniques allow the non-invasive study of flow through layers of different soils or even in heterogeneous soil mixtures. For characterizing the pore distributions in such samples the 13-interval sDDCOSY pulse sequence will provide information about the level of isotropy of the sample and about restricted diffusion in different pore sizes.

Bibliography

[ALS05] L. D. Anadon, H. M. Lim, A. J. Sederman, L. F. Gladden, Hydrodynamics in two-phase flow within porous media, Magn. Reson. Imaging 23 (2005) 291-294.

[BKC90] J. M. Brown, P. J. Kramer, G. P. Cofer, G. A. Johnson, Use of nuclear magnetic resonance microscopy for noninvasive observations of root-soil water relations, Theor. Appl. Climatol. 42 (1990) 229-236.

[BLE01] S. Boujraf, R. Luypaert, H. Eisendrath, M. Osteaux, Echo planar magnetic resonance imaging of anisotropic diffusion in asparagus stems, Magn. Reson. Mater. Phy. 13 (2001) 82-90.

[Blo46] F. Bloch, Nuclear Induction, Phys. Rev. 70 (7-8) (1946) 460-474.

[Blu00] B. Blümich, NMR imaging of materials, Oxford University Press, Oxford, 2000.

[Blu05] B. Blümich, Essential NMR, Springer, Berlin, 2005.

[BML94] P. J. Basser, J. Mattiello, D. Le Bihan, Estimation of the effective self-diffusion tensor from the NMR spin echo, J. Magn. Reson. Ser. B. 103 (1994) 247-254.

[Cal91] P. T. Callaghan, Principles of Nuclear Magnetic Resonance Microscopy, Clarendon Press, Oxford, 1991.

[CBP90] T. L. Chenevert, J. A. Brunberg, J. G. Pipe, Anisotropic diffusion within human white matter: Demonstration with NMR techniques in vivo, Radiology 177 (1990) 401-205.

[CCS99] P. T. Callaghan, S. L. Codd, J. D. Seymour, Spatial coherence phenomena arising from translational spin motion in gradient spin echo experiments, Concepts Magnetic Res 11 (1999) 181-202.

[CF04] P. T. Callaghan, I. Furó, Diffusion-diffusion correlation and exchange as a signature for local order and dynamics, J. Chem. Phys. 120 (2004) 4032-4038.

[CGR03] P. T. Callaghan, S. Godefroy, B. N. Ryland, Use of the second dimension in PGSE NMR studies of porous media, Magn. Reson. Imaging 21 (2003) 243-238.

[CHS89] R. M. Cotts, M. J. R. Hoch, T. Sun, J. T. Markert, Pulsed field gradient stimulated echo method for improved NMR diffusion measurements in heterogeneous system, J. Magn. Reson. 83 (1989) 252-266.

[CP54] H. Y. Carr, E. M. Purcell, Effects of diffusion on free precession in nuclear magnetic resonance experiments, Phys. Rev. 94 (1954) 630-638.

[Cra75] J. Crank, The mathematics of diffusion, Oxford University Press, Oxford, 1975.

[CW99] C. Chang, A. Watson, NMR imaging of flow velocity in porous media, AIChE 45 (1999) 437-440.

[DPG06] C. Doussan, A. Pierret, E. Garrigues, L. Pagès, Water uptake by plant roots: II – Modelling of water transfer in the soil root-system with explicit account of flow within the root system - Comparison with experiments, Plant Soil 283 (2006) 99-117.

[FMH85] J. Frahm, K. D. Merboldt, W. Hänicke, A. Haase, Stimulated echo imaging, J. Magn. Reson. 64 (1985) 81-83.

[GC06] P. Galvosas, P. T. Callaghan, Fast magnetic resonance imaging and velocimetry for liquids under high flow rates, J. Magn. Reson. 181 (2006) 119-125.

[GDP06] E. Garrigues, C. Doussan, A. Pierret, Water uptake by plant roots: I – Formation and propagation of a water extraction front in mature root systems as evidenced by 2D light transmission imaging, Plant Soil 283 (2006) 83-98.

[Gil07] Manual Liquid Handling, Gilson Inc., Middleton, WI USA, 2007. (www.pretech.nu/public/Gilson/MLH/MLH_Cat.pdf)

[GMP69] D. Guilfoyle, P. Mansfield, K. Packer, Fluid flow measurements in porous media by echo-planar imaging, J. Magn. Reson. 97 (1969) 342-358.

[Gre06] P. J. Gregory, Plant roots: Growth, activity and interactions with the soil, Blackwell, Oxford, 2006.

[GSK04] P. Galvosas, F. Stallmach, J. Kärger, Background gradient suppression in stimulated echo NMR diffusion studies using magic pulsed field gradient ratios, J. Magn. Reson. 166 (2004) 164-173.

[Hah50] E. L. Hahn, Spin echoes, Phys. Rev. 80 (4) 580-504.

[HMG01] S.-I. Han, O. Marseille, C. Gehlen, B. Blümich, Rheology of blood by NMR, J. Magn. Reson. 152 (2001) 87-94.

[Hoc09] F. Hochholdinger, The maize root system: morphology, anatomy, and genetics, in Handbook of maize: its biology, edited by J. L. Bennetzen, S. C. Hake, SpringerLink, 2009, DOI: 10.1007/978-0-387-79418-1_8.

[HPG02] K. H. Herrmann, A. Pohlmeier, D. Gembris, H. Vereecken, Three-dimensional imaging of pore water velocities in porous media by using magnetic resonance imaging (MRI), J. Hydrol. 267 (2002) 244-257.

[HVV10] N. M. Homan, B. Venne, H. VanAs, Flow characteristics and exchange in complex biological systems as observed by pulsed-field-gradient magnetic-resonance imaging, Phys. Rev. E 82 (2010) 026310.

[HWV07] N. M. Homan, C. W. Windt, F. J. Vergeldt, E. Gerkema, H. Van As, 0.7 and 3 T MRI and sap flow in intact trees: Xylem and phloem in action, Appl. Magn. Reson. 32 (2007) 157-170.

[JRM03] M. W. Jennette, T. W. Rufty, J. S. MacFall, Magnetic resonance image visualization of plant roots in situ: A tool for characterizing root morphology, in Digital imaging and spectral techniques: Application to precision agriculture, edited, ASA Special Publications, Madison, 2003, 65-72.

[JTV08] M. Javaux, T. Schröder, J. Vanderborght, H. Vereecken, Use of a three-dimensional detailed modeling approach for predicting root water uptake, Vadose Zone J. 7 (2008) 1079-1088.

[JV03] M. Javaux, M. Vanclooster, Scale- and rate-dependent solute transport within an unsaturated sandy aquifer, Soil. Sci. Soc. Am. J. 67 (2003) 1334-1343.

[KH83] J. Kärger, W. Heink, The propagator representation of molecular transport in microporous crystallites, J. Magn. Reson. 51 (1983) 1-7.

[Kin06-1] P. B. Kingsley, Introduction to diffusion tensor imaging mathematics: Part I. Tensors, rotations, and eigenvectors, Concepts Magn. Reso. A 28A (2006) 101-122.

[Kin06-2] P. B. Kingsley, Introduction to diffusion tensor imaging mathematics: Part II. Anisotropy, diffusion-weighting factors, and gradient echo encoding schemes, Concepts Magn. Reso. A 28A (2006) 123-154.

[Kin06-3] P. B. Kingsley, Introduction to diffusion tensor imaging mathematics: Part III. Tensor calculations, noise, simulations, and optimization, Concepts Magn. Reso. A 28A (2006) 155-179.

[KKT98] E. Kuchenbrod, E. Kahler, F. Thurmer, R. Deichmann, U. Zimmermann, A. Haase, Functional magnetic resonance imaging in intact plants – Quantitative observation of flow in plant vessels, Magn. Reson. Imaging 16 (1998) 331-338.

[KL80] R. F. Karlicek, I. J. Lowe, A modified pulsed gradient technique for measuring diffusion in the presence of large background gradients, J. Magn. Reson. 37 (1980) 75-91.

[Koe01] W. Köckenberger, Functional imaging of plants by magnetic resonance experiments, Trends Plant Sci. 6 (2001) 286-292.

[KPS04] W. Köckenberger, C. De Panfilis, D. Santoro, P. Dahiya, S. Rawsthorne, High resolution NMR microscopy of plants and fungi, J. Microsc.-Oxford 214 (2004) 182-189.

[Lau73] P. C. Lauterbur, Image formation by induced local interactions: Examples employing nuclear magnetic resonance, Nature 242 (1973) 190-191.

[LCM09] L. Li, Q. Chen, A. E. Marble, L. Romero-Zerón, B. Newling, B. J. Balcom, Flow imaging of fluids in porous media by magnetization prepared centric-scan SPRITE, J. Magn. Reson. 197 (2009) 1-8.

[LMP01] D. Le Bihan, J.-F. Mangin, C. Poupon, C. A. Clark, S. Pappata, N. Molko, H. Chabriat, Diffusion tensor imaging: Concepts and applications, J. Magn. Reson. Imaging 13 (2001) 534-546.

[Mar63] D. W. Marquardt, An algorithm for least-squares estimation of nonlinear parameters, J. Soc. Ind. Appl. Math. 11 (1963) 431-441.

[MCM90] M. E. Moseley, Y. Cohen, J. Mintorovitch, L. Chileuitt, H. Shimizu, J. Kucharczyk, M. F. Wendland, P. R. Weinstein, Early detection of regional cerebral ischemic injury in cats: Comparison of diffusion- and T_2-weighted MRI and spectroscopy, Magn. Reson. Med. 14 (1990) 330-346.

[MG73] P. Mansfield, P. K. Grannell, NMR 'diffraction' in solids?, J. Phys. C Solid State 6 (1973) L422-L426.

[MGW99] B. Manz, L. F. Gladden, P. B. Warren, Flow and dispersion in porous media: Lattice-Boltzmann and NMR studies, Aiche J. 45 (1999) 1845-1854.

[MHF85] K. D. Merboldt, W. Hanicke, J. Frahm, Self-diffusion NMR imaging using stimulated echoes, J. Magn. Reson. 64 (1985) 479-486.

[MHS99] M. I. Menzel, S.-I. Han, S. Stapf, B. Blümich, NMR characterization of the pore structure and anisotropic self-diffusion in salt water ice, J. Magn. Reson. 143 (1999) 376-381.

[Moo20] E. H. Moore, On the reciprocal of the general algebraic matrix, B. Am. Math. Soc. 26 (1920) 394-395.

[MOP07] M. I. Menzel, A. M. Oros-Peusquens, A. Pohlmeier, N. J. Shah, U. Schurr, H. U. Schneider, Comparing ^{1}H-NMR imaging and relax-

ation mapping of German white asparagus from five different cultivation sites, J. Plant Nutr. Soil Sci. 170 (2007) 24-38.

[MP78] P. Mansfield, I. L. Pykett, Biological and medical imaging by NMR, J. Magn. Reson. 29 (1978) 355-373.

[NBN02] N. Nestle, T. Baumann, R. Niessner, Magnetic resonance imaging in environmental science, Environ. Sci. Technol. 36 (2002) 154A-160A.

[PDW09] A. Pohlmeier, D. van Dusschoten, L. Weihermüller, U. Schurr, H. Vereecken, Imaging water fluxes in porous media by magnetic resonance imaging using D_20 as a tracer, Magn. Reson. Imaging 27 (2009) 285-292.

[Pen55] R. Penrose, A generalized inverse for matrices, P. Camb. Philos. Soc. 51 (1955) 406-413.

[POP07] A. Pohlmeier, A. M. Oros-Peusquens, M. Javaux, M. I. Menzel, H. Vereecken, N. J. Shah, Investigation of water content and dynamics of a ricinus root system in unsaturated sand by means of SPRITE and CISS: correlation of root architecture and water content change, Magn. Reson. Imaging 25 (2007) 579-580.

[POP08] A. Pohlmeier, A. M. Oros-Peusquens, M. Javaux, M. I. Menzel, J. Vanderborght, J. Kaffanke, S. Romanzetti, J. Lindenmair, H. Vereecken, N. J. Shah, Changes in soil water content resulting from ricinus root uptake monitored by magnetic resonance imaging, Vadose Zone J. 7 (2008) 1010-1017.

[PRZ01] A. Peuke, M. Rokitta, U. Zimmermann, L. Schreiber, A. Haase, Simultaneous measurements of water flow velocity and solute transport in xylem and phloem of adult plants of *Ricinus communis* over a daily time course by nuclear magnetic resonance spectroscopy, Plant Cell Environ. 24 (2001) 491-503.

[QuF09] Data sheet quartz sand FH 31, Quarzwerke GmbH, Germany, 2009.

[Rot07] K. Roth, Soil physics – Lecture notes, Institute of Environmental Physics, University of Heidelberg, 2007.
(www.iup.uni-heidelberg.de/institut/forschung/groups/ts/students)

[RZH99] M. Rokitta, U. Zimmermann, A. Haase, Fast NMR flow measurements in plants using FLASH imaging, J. Magn. Reson. 137 (1999) 29-32.

[SC96] J. D. Seymour, P. T. Callaghan, "Flow-diffraction" structural characterization and measurement of hydrodynamic dispersion in porous media by PGSE NMR, J. Magn. Reson. Ser. A 122 (1996) 90-93.

[SDJ00-1] T. Scheenen, D. van Dusschoten, P. A. de Jager, H. van As, Microscopic displacement imaging with pulsed field gradient turbo spin-echo NMR, J. Magn Reson. 142 (2000) 207-215.

[SDJ00-2] T. Scheenen, D. van Dusschotenn, P. A. de Jager, H. van As, Quantification of water transport in plants with NMR imaging, J. Exp. Bot. 51 (2000) 1751-1759.

[SG07] F. Stallmach, P. Galvosas, Spin echo NMR diffusion studies, Ann. R. NMR S. 61 (2007) 51-131.

[SHJ02] T. Scheenen, A. Heemskerk, A. P. de Jager, F. J. Vergeldt, H. van As, Functional imaging of plants: A nuclear magnetic resonance study of a cucumber plant, Biophys. J. 82 (2002) 481-492.

[SPB09] L. R. Stingaciu, A. Pohlmeier, P. Blümler, L. Weihermüller, D. van Dusschoten, S. Stapf, H. Vereecken, Characterization of unsaturated porous media by high-field and low-field NMR relaxometry, Water Resour. Res. 45 (2009) W08412.

[ST65] E. O. Stejskal, J. E. Tanner, Spin diffusion measurements: Spin echoes in the presence of a time-dependent field gradient, J. Chem. Phys. 42 (1965) 288-292.

[Ste65] E. O. Stejskal, Use of spin echoes in a pulsed magnetic-field gradient to study anisotropic, restricted diffusion and flow, J. Chem. Phys. 43 (1965) 3597-3603.

[SVH02] Y.-Q. Song, L. Venkataramanan, M. D. Hürlimann, M. Flaum, P. Frulla, C. Straley, T_1-T_2 correlation spectra obtained using a fast two-dimensional Laplace inversion, J. Magn. Reson. 154 (2002) 261-268.

[SVW01] T. Scheenen, F. J. Vergeldt, C. W. Windt, P. A. de Jager, H. van As, Microscopic imaging of slow flow and diffusion: A pulsed field gradient stimulated echo sequence combined with turbo spin echo imaging, J. Magn. Reson. 151 (2001) 94-100.

[Tan70] J. E. Tanner, Use of stimulated echo in NMR diffusion studies, J. Chem. Phys. 52 (1970) 2523-2526.

[Tor56] H. C. Torrey, Bloch equations with diffusion terms, Phys. Rev. 104 (1956) 563-565.

[VAD97] H. van As, D. van Dusschoten, NMR methods for imaging of transport processes in micro-porous systems, Geoderma 80 (1997) 389-403.

[WEK91] Y. Waisel, A. Eshel, U. Kafkafi, Plant roots: The hidden half, Marcel Dekker Inc., New York, 1991.

[WF96] R. A. Waggoner, E. Fukushima, Velocity distribution of slow fluid flows in Bentheimer sandstone: an NMRI and propagator study, Magn. Reson. Imaging 14 (1996) 1085-1092.

[WRW00] N. Wistuba, R. Reich, H. J. Wagner, J. J. Zhu, H. Schneider, F. W. Bentrup, A. Haase, U. Zimmermann, Xylem flow and its driving forces in a tropical liana: Concomitant flow-sensitive NMR imaging and pressure probe measurements, Plant Biol. 2 (2000) 579-582.

[WSD07] L. Weihermüller, J. Siemens, M. Deurer, S. Knoblauch, H. Rupp, A. Göttlein, T. Pütz, In-situ soil water extraction: a review, J. Environ. Qual. 36 (2007) 1735-1748.

[ZP07] G. Zheng, W. S. Price, Suppression of background gradients in (B_0 gradient-based) NMR diffusion experiments, Concept Magn. Reson. A 30A (2007) 261-277.

List of Figures

1.1. Overview of investigations presented in this thesis for understanding root water uptake 4

2.1. Magnet systems used for the measurements presented in this thesis . 8
2.2. Picture of maize plant and roots 10

5.1. Principle of spin echo pulse sequence 30
5.2. Spin echo pulse sequence with pulsed field gradients 30
5.3. Spin echo pulse sequence with constant field gradients 35
5.4. Principle of stimulated echo pulse sequence 37
5.5. Stimulated echo pulse sequence with pulsed field gradients 38
5.6. 13-interval stimulated echo pulse sequence 41
5.7. DDCOSY pulse sequence 46
5.8. Exemplary 2D maps of diffusion coefficient distributions resulting from measurements with the DDCOSY pulse sequence 48
5.9. Imaging spin echo pulse sequence 51
5.10. Diffusion tensor imaging pulse sequence 53
5.11. Imaging stimulated echo pulse sequence 55
5.12. Stimulated echo pulse sequence for velocity imaging 59

6.1. sDDCOSY pulse sequence 62
6.2. 13-interval sDDCOSY pulse sequence 66
6.3. 13-interval STEMSI pulse sequence 67

8.1. Experimental setup for high resolution MRI and DTI measurements on plant roots 80
8.2. Optical microscopic slice of a maize root 81
8.3. Comparison of an optical microscopic slice with a high resolution anatomical NMR image of the maize spear 82

8.4. Side view of three-dimensional reconstructed root system of a maize plant resulting from MRI measurements 83
8.5. High resolution NMR image to identify regions containing plant roots 85
8.6. Intensity map from DTI measurement with zero PFG amplitudes . . 87
8.7. Decay of NMR signal with increasing b-value of selected pixels 89
8.8. Map of the highest eigenvalues of diffusion tensors 91
8.9. Map of fractional anisotropy FA 92
8.10. Three-dimensional tensor visualization of eigenvalues and eigenvectors 94
8.11. Three-dimensional tensor visualization of a single root 95
8.12. Experimental setup for one- and two-dimensional diffusion measurements on natural sand 97
8.13. Comparison of common stimulated echo pulse sequence with the 13-interval pulse sequence on water saturated sand 98
8.14. Map of the diffusion coefficient distribution of water in natural sand measured with sDDCOSY 101
8.15. Map of water diffusion coefficients in natural sand measured with 13-interval sDDCOSY 102
8.16. Experimental setup for velocity mapping of water flow through natural sand 104
8.17. Velocity maps and 1D mean velocity profiles at the highest applied pore velocity 106
8.18. Velocity maps and 1D mean velocity profiles of the lowest applied pore velocity 108
8.19. Histogram of the NMR detected pore flow velocity distribution of the highest applied pore flow velocity 109
8.20. Plot of dependency of the width of the velocity distribution from the applied pore flow velocity 110
8.21. Comparison of applied pore flow velocities and experimental determined mean pore flow velocities 111
8.22. Intensity maps and 1D mean intensity profiles of the lowest NMR detectable applied pore flow velocity 112
8.23. Plot of dependency of signal intensity from the applied flow velocity . 113
8.24. Dependence of the velocity detected with flow-encoding on the observation time Δ 115
8.25. Corrected velocity map of the recorded experimental data 117

A. Abbreviations and symbols

Abbreviations

1D ..... One Dimensional
2D ..... Two Dimensional
3D ..... Three Dimensional
APFG ..... Alternating Pulsed magnetic Field Gradient
CFG ..... Constant magnetic Field Gradient
DDCOSY ..... Diffusion Diffusion COrrelation Spectroscopy
DTI ..... Diffusion Tensor Imaging
FID ..... Free Induction Decay
FOV ..... Field Of View
LM ..... Levenberg-Marquardt
MP ..... Moore-Penrose
MRI ..... Magnetic Resonance Imaging
NMR ..... Nuclear Magnetic Resonance
PFG ..... Pulsed magnetic Field Gradient
RCF ..... Rotating Coordinate Frame
rf ..... radio frequency
sDDCOSY ..... short Diffusion Diffusion COrrelation Spectroscopy
SNR ..... Signal to Noise Ratio
SPRITE ..... Single-Point Ramped Imaging with T_1 Enhancement
STEMSI ..... STimulated Echo Multi Slice Imaging
TDR ..... Time Domain Reflectometry

Symbols

∇	nabla operator
$\delta(x)$	Dirac delta function
$\boldsymbol{e}_x$, $\boldsymbol{e}_y$, $\boldsymbol{e}_z$	unity vectors of a Cartesian coordinate system
x, y, z	main directions in the laboratory coordinate system

α	$[\mathrm{s}^{-1}]$	excitation profile
$\boldsymbol{\alpha}$	$[\mathrm{m}^2\,\mathrm{s}^{-1}]$	vector containing the fitted diffusion coefficients
γ	$[\mathrm{s}^{-1}\,\mathrm{T}^{-1}]$	gyromagnetic ratio
γ_p	$[\mathrm{s}^{-1}\,\mathrm{T}^{-1}]$	gyromagnetic ratio of protons
δ	[s]	duration of a PFG
δ_1	[s]	time delay before a PFG
δ_2	[s]	time delay after a PFG
Δ	[s]	observation time
Δ'	[s]	storage time in stimulated echo pulse sequence between the second and third 90° rf pulse
λ	$[\mathrm{m}^2\,\mathrm{s}^{-1}]$	eigenvalue of the diffusion tensor
λ_i	$[\mathrm{m}^2\,\mathrm{s}^{-1}]$	eigenvalue of the diffusion tensor in x, y, or z direction
Λ	[m]	dispersivity parameter
$\boldsymbol{\mu}$	$[\mathrm{J}\,\mathrm{T}^{-1}]$	magnetic moment
ρ	$[\mathrm{m}^{-3}]$	spin density
σ		standard deviation, unit depends on distributed variable
τ	[s]	time delay between exciting 90° and refocusing 180° rf pulse
φ		absolute receiver phase
ϕ		phase shift of NMR signal at velocity imaging
$\phi_{\boldsymbol{g}^*}$		phase shift of NMR signal at velocity imaging caused by internal magnetic field gradients
$\phi_{\boldsymbol{G}^*}$		phase shift of NMR signal at velocity imaging caused by pulsed magnetic field gradients
$\Delta\phi$		net phase shift of NMR signal at velocity imaging

Φ		phase, containing the time dependent evolution of the Larmor frequency ω_0
θ	$[\mathrm{cm^3\,cm^{-3}}]$	water content
ω	$[\mathrm{s^{-1}}]$	frequency
ω_0	$[\mathrm{s^{-1}}]$	Larmor frequency
ω_1	$[\mathrm{s^{-1}}]$	frequency of alternating magnetic field $\boldsymbol{B_1}$
$\Delta\omega$	$[\mathrm{s^{-1}}]$	offset frequency

a	[m]	slice thickness
A_c; A'_c	$[\mathrm{s^3\,T\,m^{-1}; s^3}]$	cross term, spin echo attenuation caused by pulsed and internal magnetic field gradients
$A_\mathrm{c,gen}$	$[\mathrm{s^3\,T\,m^{-1}}]$	generalized cross term, spin echo attenuation caused by pulsed and internal magnetic field gradients
A_i; A'_i	$[\mathrm{s^3\,T\,m^{-1}; s^3}]$	spin echo attenuation caused by internal magnetic field gradients
$A_\mathrm{i,gen}$	$[\mathrm{s^3\,T\,m^{-1}}]$	generalized spin echo attenuation caused by internal magnetic field gradients
A_p; A'_p	$[\mathrm{s^3\,T\,m^{-1}; s^3}]$	spin echo attenuation caused by pulsed magnetic field gradients
$A_\mathrm{p,gen}$	$[\mathrm{s^3\,T\,m^{-1}}]$	generalized spin echo attenuation caused by pulsed magnetic field gradients
$\boldsymbol{a}_i$		eigenvector of the diffusion tensor
b	$[\mathrm{s\,m^{-2}}]$	b-value, describing the influence of PFGs on the NMR signal
b_{ij}, $b_{ij(,1,2)}$	$[\mathrm{s\,m^{-2}}]$	element of the **b**-matrix, describing the influence of PFGs on the NMR signal
$B_{1,z}$	[T]	z component of the alternating magnetic field $\boldsymbol{B}_1$
B_PFG	[T]	magnetic field caused by a PFG
B_x, B_y, B_z	[T]	magnetic field strength in x, y, and z direction, respectively
ΔB_0	[T]	spread in magnetic field strength

$\boldsymbol{B}$	[T]	magnetic field strength
$\boldsymbol{B}_0$	[T]	external polarizing magnetic field strength
$\boldsymbol{B}_1$	[T]	strength of alternating magnetic field
B_i	$[\mathrm{s^2\,T\,m^{-1}}]$	spin echo phase shift caused by internal magnetic field gradients
B_p	$[\mathrm{s^2\,T\,m^{-1}}]$	spin echo phase shift caused by pulsed magnetic field gradients
$\mathbf{b}$	$[\mathrm{s\,m^{-2}}]$	**b**-matrix, describing the influence of PFGs on the NMR signal
$\mathbf{b}_{\boldsymbol{ij}}$, $\mathbf{b}_{6d}$	$[\mathrm{s\,m^{-2}}]$	re-defined **b**-matrix for data analyzing
c	$[\mathrm{mol\,m^{-3}}]$	concentration
C	[V]	NMR signal offset
C_model	[V]	NMR signal offset in model calculations
d		number of PFG steps in one direction
d_i	[m]	inner diameter of sand tube
D, $D_{ij(,1,2)}$	$[\mathrm{m^2\,s^{-1}}]$	diffusion coefficient
D_eff	$[\mathrm{m^2\,s^{-1}}]$	effective dispersion coefficient
$\mathbf{D}$	$[\mathrm{m^2\,s^{-1}}]$	diffusion tensor
$\mathbf{D}_\mathrm{model}$	$[\mathrm{m^2\,s^{-1}}]$	diffusion tensor in model calculations
E_m	[J]	energy of spins with magnetic quantum number m
ΔE	[J]	the gap between two energy levels
$\mathbf{E}$	[V]	experimental noise
$\mathcal{F}$	$[\mathrm{A\,m^{-1}}]$	probability density
g_x^*, g_y^*, g_z^*	$[\mathrm{T\,m^{-1}}]$	effective internal magnetic field gradient in x, y, and z direction, respectively
G_i	$[\mathrm{T\,m^{-1}}]$	component i of the magnetic field gradient vector $\boldsymbol{G}$
G_x, G_y, G_z	$[\mathrm{T\,m^{-1}}]$	pulsed magnetic field gradient in x, y, and z direction, respectively
G_x^*, G_y^*, G_z^*	$[\mathrm{T\,m^{-1}}]$	effective pulsed magnetic field gradient in x, y, and z direction, respectively
$\boldsymbol{g}$	$[\mathrm{T\,m^{-1}}]$	internal magnetic field gradient
$\boldsymbol{g^*}$	$[\mathrm{T\,m^{-1}}]$	effective internal magnetic field gradient
$\boldsymbol{G}$, $\boldsymbol{G}_\mathbf{min}$, $\boldsymbol{G}_\mathbf{max}$	$[\mathrm{T\,m^{-1}}]$	pulsed magnetic field gradient

$\lvert\boldsymbol{G}\rvert$	$[\mathrm{T\,m^{-1}}]$	amplitude of a PFG
$\Delta\boldsymbol{G}$	$[\mathrm{T\,m^{-1}}]$	difference between different PFGs
$\boldsymbol{G}^*$	$[\mathrm{T\,m^{-1}}]$	effective pulsed magnetic field gradient
$\boldsymbol{G_{ij}}$	$[\mathrm{T\,m^{-1}}]$	pulsed magnetic field gradients in the directions xx, yy, zz, xy, xz and yz
$\boldsymbol{G}_\mathrm{p}$	$[\mathrm{T\,m^{-1}}]$	phase-encoding magnetic field gradient
$\boldsymbol{G}_\mathrm{r}$	$[\mathrm{T\,m^{-1}}]$	read out magnetic field gradient
$\boldsymbol{G}_\mathrm{s}$	$[\mathrm{T\,m^{-1}}]$	slice selective magnetic field gradient
h	$[\mathrm{J\,s}]$	Planck's constant
I_p	$[\mathrm{s\,T\,m^{-1}}]$	integral over the effective magnetic field gradients during the preparation time
I_r	$[\mathrm{s\,T\,m^{-1}}]$	integral over the effective magnetic field gradients during the reading time
$\boldsymbol{I}$		nuclear spin
$\mathbf{I}$		identity matrix
J_max	$[\mathrm{L\,s^{-1}}]$	maximal volume flow applied
$\boldsymbol{j}$	$[\mathrm{mol\,m^{-2}\,s^{-1}}]$	diffusion flux
k		order of moments of the gradient function
k_1, k_2		mathematical description between parameters and the NMR signal
k_B	$[\mathrm{J\,K^{-1}}]$	Boltzmann's constant
$k_{x,y}$	$[\mathrm{m^{-1}}]$	x and y components of the reciprocal space vector $\boldsymbol{k}$
$\boldsymbol{k}$, $\boldsymbol{k}_\mathbf{min}$, $\boldsymbol{k}_\mathbf{max}$	$[\mathrm{m^{-1}}]$	reciprocal space vector
$\mathrm{d}\boldsymbol{k}$	$[\mathrm{m^{-1}}]$	infinitesimal reciprocal space vector
m	$[\mathrm{A\,m^{-1}}]$	magnetic quantum number
M_{xy}	$[\mathrm{A\,m^{-1}}]$	macroscopic transverse magnetization
$M_{x,y}$	$[\mathrm{A\,m^{-1}}]$	macroscopic magnetization in x and y direction, respectively
M_z	$[\mathrm{A\,m^{-1}}]$	macroscopic magnetization in z direction
$\mathcal{M}$	$[\mathrm{A\,m^{-1}}]$	complex linear combination of the magnetization in x and y direction
$\boldsymbol{m}_k$		moment of gradient function with order k
$\boldsymbol{m}_0$	$[\mathrm{s\,T\,m^{-1}}]$	moment of gradient function with order 0

$\boldsymbol{m}_1$	$[\mathrm{s^2\,T\,m^{-1}}]$	moment of gradient function with order 1
$\boldsymbol{M}$	$[\mathrm{A\,m^{-1}}]$	macroscopic magnetization vector
$\boldsymbol{M}_0$	$[\mathrm{A\,m^{-1}}]$	macroscopic magnetization vector in the thermodynamic equilibrium
$\mathbf{M}$	$[\mathrm{A\,m^{-1}}]$	two-dimensional array of the NMR signal
$n_{\max}$	[rpm]	highest pump rate
P	$[\mathrm{m^{-3}}]$	propagator of the diffusion process
$\boldsymbol{q}$, $\boldsymbol{q}_1$, $\boldsymbol{q}_2$	$[\mathrm{s\,m^{-1}}]$	reciprocal velocity vector
$\boldsymbol{r}$	[m]	coordinate in space
$\boldsymbol{r_i}$	[m]	position of spin i
$\mathrm{d}\boldsymbol{r}$	[m]	infinitesimal space vector
$\boldsymbol{r}_0$	[m]	spatial location at $t = 0$
$\boldsymbol{R}$	[m]	molecular mean displacement
S	[V]	NMR signal
S_0	[V]	NMR signal immediately following the excitation pulse
S_{model}		NMR signal in model calculations
$\boldsymbol{s}$, $\boldsymbol{s_{ij}}$		re-defined NMR signal S for data analyzing
t, t', t''	[s]	time
$\mathrm{d}t$, $\mathrm{d}t'$, $\mathrm{d}t''$	[s]	infinitesimal time
t_a, t_b	[s]	time at which rf pulses are applied
t_{e}	[s]	echo time
t_x, t_y	[s]	time periods depending on magnetic field gradients in x and y direction
T_1	[s]	longitudinal, spin-lattice relaxation time
T_2	[s]	pure transversal, spin-spin relaxation time
T_2^*	[s]	detectable time constant containing T_2 relaxation and T_{inhom}
T_{inhom}	[s]	relaxation time of NMR signal due to magnetic field inhomogeneities
TR	[s]	repetition time
v	$[\mathrm{m\,s^{-1}}]$	velocity
v_{appl}	$[\mathrm{m\,s^{-1}}]$	applied pore flow velocity
$v_{\mathrm{appl,max}}$	$[\mathrm{m\,s^{-1}}]$	highest applied pore flow velocity
$v_{\mathrm{appl,min}}$	$[\mathrm{m\,s^{-1}}]$	minimum detectable pore flow velocity

$v_{\mathrm{appl},0}$	$[\mathrm{m\,s^{-1}}]$	lowest applied pore flow velocity
V	$[\mathrm{m^3}]$	sample volume
$\boldsymbol{v}$	$[\mathrm{m\,s^{-1}}]$	velocity vector
$\boldsymbol{v}_0$	$[\mathrm{m\,s^{-1}}]$	velocity at $t = 0$

B. Acknowledgments

This PhD thesis was performed at the Institute of Bio- and Geosciences, Agrosphere (IBG-3) at the Forschungszentrum Jülich. It is now a pleasure for me to thank all those who have contributed to this exciting journey.

First and foremost, I wish to express my deep gratitude to Dr. Andreas Pohlmeier, who has introduced me to nuclear magnetic resonance in soil sciences and has guided me throughout these three years. Thank you Andreas for your constant support, motivation and kindness. You always made time for me to discuss measurement results and things beyond. It has been a privilege to perform my PhD under your supervision.

I greatfully acknowledge Prof. Dr. Bernhard Blümich for kindly accepting to report on my thesis, as well as for many discussions on the DTI measurements and suggestions for interpreting my experimental results of the flow investigations.

My special thank goes to Prof. Dr. Harry Vereecken for giving me the opportunity to perform this thesis in his institute and for agreeing to be the second thesis examiner. I gratefully acknowledge his confidence in me from the moment we first met and his constant support over the years. He has always made me feel at home at the IBG-3.

I heartily thank Dr. Marion Menzel who has been a great source of knowledge and inspiration for me. Thank you Marion for all your support and MRI teaching, your neverending motivation and your trust in me.

I warmly thank Dr. Petrik Galvosas for the very nice collaboration which has extended beyond my research stay in Wellington. He has always taken the time to explain to me in depth the concepts, which I sometimes struggled with. Petrik, I owe you so much.

My gratitude goes to Prof. Dr. Paul Callaghan for warmly welcoming and integrating me in his outstanding research group for seven months. Paul, I deeply admire your strength through the last months and wish you all the best. Your power gives me so much strength and motivated my work.

A great thank you goes to Dr. Laura Stingaciu, my lovely office colleague. Thank you Laura for all our discussions about NMR, science and the world behind.

I am grateful to Oscar Sucre for many inspiring discussions. Oscar, I thank you for introducing me to the secrets of the NMR endoscope.

Special thanks are addressed to Dr. Dagmar van Dusschoten for his day to day technical support during my measurements in the GreenNMRHouse. Sincere thanks are addressed to Jonas Bühler for his introduction to MeVisLab for root and tensor visualization.

I wish to thank Prof. Dr. Jan Vanderborght and Prof. Dr. Mathieu Javaux for many discussions and intellectual support.

I am thankful to Gaby Pillert, Marion Schlösser and Birgit Spellerberg who have guided me through the research center's administrative labyrinth.

My gratitude also goes to the computer specialists Thomas Schuster and Jens Heidbüchel for their quick and reliable help at any technical problems. I am very grateful to the mechanical workshop technicians, especially to Ayhan Egmen, for all the nice constructions they put into reality for my experimental setups.

I thank all PhD students from *Studium Universale* for the opportunity to look beyond science and administration at the Forschungszentrum Jülich. I am also very grateful for the trust of the Jülich PhD students to made me represent their concerns at the *Helmholtz Juniors*, the PhD initiative of the Helmholtz Association.

To all the colleagues and friends I met in Jülich, Aachen, and Wellington and who have accompanied me on my journey: thank you for the great time. Thereby special thanks go to Melissa Phillips, Catherine O'Sullivan and Phoebe for making me feeling home in New Zealand.

A special thank you goes to Prof. Dr. Bernhard Blümich, Dr. Andreas Pohlmeier, Dr. Marion Menzel, Dr. Petrik Galvosas and Dr. Christian Spindler who read my work (in whole or in part) and gave me fruitful suggestions for improving this thesis.

I would like to express my deepest gratitude to my parents and my brother André who had never any doubt in my abilities and always supported me in life and work.

My most deeply felt gratitude goes to my husband Christian, I would not have made it without him, giving me the patience and the strength to enjoy the last years. I thank you so much for all our discussions about our sciences and beyond, for your neverending motivation and your love, wherever one of us had been on this earth.

C. Curriculum Vitae

Personal data

Name	Natascha Spindler
Date of birth	26 August 1982
Place of birth	Naila

Education

since 01/2008	Research assistant and PhD student in the Institute for Bio- and Geosciences, Agrosphere (IBG-3), Forschungszentrum Jülich
09/2009–03/2010	Visiting PhD student in the group of Prof. Paul Callaghan at the Victoria University in Wellington, New Zealand
06/2007–12/2007	Research assistant in the Institute for Bio- and Geosciences, Phytosphere (IBG-2), Forschungszentrum Jülich
06/2006–05/2007	Diploma thesis in applied energy technology at the Bavarian Center for Applied Energy Research, Würzburg, on the topic: *Phase change materials – Packaging and Characterization*
10/2002–05/2007	Study of physics (Diploma degree) at the Bayerische Julius-Maximilians-University of Würzburg
09/1989–06/2002	Gymnasium Naila with emphasis on maths and sciences

Further NMR education

04/2010–07/2010	Lecture of Prof. Dr. Bernhard Blümich: *NMR in material science and chemical process engineering*
05/2008–06/2008	Summer School *7th PhD Course 'in vivo NMR'* at the Wageningen NMR Centre, the Netherlands
10/2007–02/2008	Lecture of Prof. Dr. Stefan Appelt: *Quantum mechanics of nuclear magnetic resonance*

Scholar ship, accompanying activity and interdisciplinary qualifications

10/2009–12/2009	DAAD scholar ship for financial support for visiting Prof. Paul Callaghans group in New Zealand
01/2009–12/2009	Forschungszentrum Jülich PhD students' representative in the Helmholtz Association
07/2010	Presentation technique: Free speech (Part III)
06/2010	Scientific writing course
05/2010	Creativity techniques for the working practice
04/2009	Target, time and team management
04/2009	Presentation technique: Rhetoric (Part II)
02/2009	Presentation technique: Basics (Part I)
01/2009	Leaders don't fall out of the sky – A review of your leadership competence

D. Publications

List of reviewed publications

Water flow investigation on quartz sand with 13-interval stimulated echo multi slice imaging, Natascha Spindler, Andreas Pohlmeier, Petrik Galvosas, Special Issue of AIP Conference Proceedings, in press.

NMR velocimetry with 13-interval stimulated echo multi slice imaging in natural porous media under small flow rates, Natascha Spindler, Petrik Galvosas, Andreas Pohlmeier, Harry Vereecken, Journal of Magnetic Resonance, in preparation.

Diffusion Tensor Imaging (DTI) on maize roots, Natascha Spindler, Marion I. Menzel, Andreas Pohlmeier, Harry Vereecken, Magnetic Resonance Imaging, in preparation.

Work conducted at the Bavarian Center for Applied Energy Research was not published due to intellectual property restrictions.

List of presentations on conferences

High resolution NMR Imaging and Relaxation Mapping to study the transition of activity of wood garlic (Allium ursinum) in natural soils: A Feasibility Study, Natascha Spindler, Dagmar van Dusschoten, Reiner Almstedt, Andreas Ulbrich, Heike U. Schneider, Marion I. Menzel, 2007, International Conference on Magnetic Resonance Microscopy (ICMRM, Aachen).

NMR-Relaxationszeitmessungen und hochauflösende Bildgebung an Bärlauch (Allium ursinum): Untersuchungen zur Kultivierung in einer Machbarkeitsstudie, Natascha Spindler, Dagmar van Dusschoten, Reiner Almstedt, Andreas Ulbrich,

Heike U. Schneider, Marion I. Menzel, 2007, Deutsche Physikerinnentagung (Osnabrück).

Geheimnis Wurzeln: Mit Magnetresonanztomographie gelingt ein Blick in den Boden, Natascha Spindler, Marion I. Menzel, Andreas Pohlmeier, Jonas Bühler, Dagmar van Dusschoten, Bernhard Blümich, Ulrich Schurr, Harry Vereecken, 2008, oral presentation at the Deutsche Physikerinnentagung (Münster).

Diffusion Tensor Magnetic Resonance Imaging on Maize Roots in Soil, Natascha Spindler, Marion I. Menzel, Andreas Pohlmeier, Bernhard Blümich, Ulrich Schurr, Harry Vereecken, 2009, oral presentation at the Frühjahrstagung der Deutschen Physikalischen Gesellschaft (Hamburg).

Diffusion Tensor Imaging of water dynamics in roots of Zea Mais Helix, Marion I. Menzel, Natascha Spindler, Bernhard Blümich, Andreas Pohlmeier, Harry Vereecken, Ulrich Schurr, 2009, EUROMAR Conference (Gothenburg).

13-interval Stimulated Echo Multi Slice Imaging for Flow Investigations on Quartz Sand, Natascha Spindler, Andreas Pohlmeier, Petrik Galvosas, 2010, Joint EUROMAR and 17th ISMAR Conference (Florence).

Water flow investigation on quartz sand with 13-interval stimulated echo multi slice imaging, Natascha Spindler, Andreas Pohlmeier, Petrik Galvosas, 2010, oral presentation at the MRPM 10 (Leipzig).

Schriften des Forschungszentrums Jülich
Reihe Energie & Umwelt / Energy & Environment

1. **Einsatz von multispektralen Satellitenbilddaten in der Wasserhaushalts- und Stoffstrommodellierung – dargestellt am Beispiel des Rureinzugsgebietes**
   von C. Montzka (2008), XX, 238 Seiten
   ISBN: 978-3-89336-508-1

2. **Ozone Production in the Atmosphere Simulation Chamber SAPHIR**
   by C. A. Richter (2008), XIV, 147 pages
   ISBN: 978-3-89336-513-5

3. **Entwicklung neuer Schutz- und Kontaktierungsschichten für Hochtemperatur-Brennstoffzellen**
   von T. Kiefer (2008), 138 Seiten
   ISBN: 978-3-89336-514-2

4. **Optimierung der Reflektivität keramischer Wärmedämmschichten aus Yttrium-teilstabilisiertem Zirkoniumdioxid für den Einsatz auf metallischen Komponenten in Gasturbinen**
   von A. Stuke (2008), X, 201 Seiten
   ISBN: 978-3-89336-515-9

5. **Lichtstreuende Oberflächen, Schichten und Schichtsysteme zur Verbesserung der Lichteinkopplung in Silizium-Dünnschichtsolarzellen**
   von M. Berginski (2008), XV, 171 Seiten
   ISBN: 978-3-89336-516-6

6. **Politikszenarien für den Klimaschutz IV – Szenarien bis 2030**
   hrsg.von P. Markewitz, F. Chr. Matthes (2008), 376 Seiten
   ISBN 978-3-89336-518-0

7. **Untersuchungen zum Verschmutzungsverhalten rheinischer Braunkohlen in Kohledampferzeugern**
   von A. Schlüter (2008), 164 Seiten
   ISBN 978-3-89336-524-1

8. **Inorganic Microporous Membranes for Gas Separation in Fossil Fuel Power Plants**
   by G. van der Donk (2008), VI, 120 pages
   ISBN: 978-3-89336-525-8

9. **Sinterung von Zirkoniumdioxid-Elektrolyten im Mehrlagenverbund der oxidkeramischen Brennstoffzelle (SOFC)**
   von R. Mücke (2008), VI, 165 Seiten
   ISBN: 978-3-89336-529-6

10. **Safety Considerations on Liquid Hydrogen**
    by K. Verfondern (2008), VIII, 167 pages
    ISBN: 978-3-89336-530-2

11. **Kerosinreformierung für Luftfahrtanwendungen**
von R. C. Samsun (2008), VII, 218 Seiten
ISBN: 978-3-89336-531-9

12. **Der 4. Deutsche Wasserstoff Congress 2008 – Tagungsband**
hrsg. von D. Stolten, B. Emonts, Th. Grube (2008), 269 Seiten
ISBN: 978-3-89336-533-3

13. **Organic matter in Late Devonian sediments as an indicator for environmental changes**
by M. Kloppisch (2008), XII, 188 pages
ISBN: 978-3-89336-534-0

14. **Entschwefelung von Mitteldestillaten für die Anwendung in mobilen Brennstoffzellen-Systemen**
von J. Latz (2008), XII, 215 Seiten
ISBN: 978-3-89336-535-7

15. **RED-IMPACT**
Impact of Partitioning, Transmutation and Waste Reduction Technologies on the Final Nuclear Waste Disposal
SYNTHESIS REPORT
ed. by W. von Lensa, R. Nabbi, M. Rossbach (2008), 178 pages
ISBN 978-3-89336-538-8

16. **Ferritic Steel Interconnectors and their Interactions with Ni Base Anodes in Solid Oxide Fuel Cells (SOFC)**
by J. H. Froitzheim (2008), 169 pages
ISBN: 978-3-89336-540-1

17. **Integrated Modelling of Nutrients in Selected River Basins of Turkey**
Results of a bilateral German-Turkish Research Project
project coord. M. Karpuzcu, F. Wendland (2008), XVI, 183 pages
ISBN: 978-3-89336-541-8

18. **Isotopengeochemische Studien zur klimatischen Ausprägung der Jüngeren Dryas in terrestrischen Archiven Eurasiens**
von J. Parplies (2008), XI, 155 Seiten, Anh.
ISBN: 978-3-89336-542-5

19. **Untersuchungen zur Klimavariabilität auf dem Tibetischen Plateau - Ein Beitrag auf der Basis stabiler Kohlenstoff- und Sauerstoffisotope in Jahrringen von Bäumen waldgrenznaher Standorte**
von J. Griessinger (2008), XIII, 172 Seiten
ISBN: 978-3-89336-544-9

20. **Neutron-Irradiation + Helium Hardening & Embrittlement Modeling of 9%Cr-Steels in an Engineering Perspective (HELENA)**
by R. Chaouadi (2008), VIII, 139 pages
ISBN: 978-3-89336-545-6

21. **in Bearbeitung**

22. **Verbundvorhaben APAWAGS (AOEV und Wassergenerierung) – Teilprojekt: Brennstoffreformierung – Schlussbericht**
von R. Peters, R. C. Samsun, J. Pasel, Z. Porš, D. Stolten (2008), VI, 106 Seiten
ISBN: 978-3-89336-547-0

23. **FREEVAL**
Evaluation of a Fire Radiative Power Product derived from Meteosat 8/9 and Identification of Operational User Needs
Final Report
project coord. M. Schultz, M. Wooster (2008), 139 pages
ISBN: 978-3-89336-549-4

24. **Untersuchungen zum Alkaliverhalten unter Oxycoal-Bedingungen**
von C. Weber (2008), VII, 143, XII Seiten
ISBN: 978-3-89336-551-7

25. **Grundlegende Untersuchungen zur Freisetzung von Spurstoffen, Heißgaschemie, Korrosionsbeständigkeit keramischer Werkstoffe und Alkalirückhaltung in der Druckkohlenstaubfeuerung**
von M. Müller (2008), 207 Seiten
ISBN: 978-3-89336-552-4

26. **Analytik von ozoninduzierten phenolischen Sekundärmetaboliten in *Nicotiana tabacum* L. cv Bel W3 mittels LC-MS**
von I. Koch (2008), III, V, 153 Seiten
ISBN 978-3-89336-553-1

27. **IEF-3 Report 2009. Grundlagenforschung für die Anwendung**
(2009), ca. 230 Seiten
ISBN: 978-3-89336-554-8

28. **Influence of Composition and Processing in the Oxidation Behavior of MCrAlY-Coatings for TBC Applications**
by J. Toscano (2009), 168 pages
ISBN: 978-3-89336-556-2

29. **Modellgestützte Analyse signifikanter Phosphorbelastungen in hessischen Oberflächengewässern aus diffusen und punktuellen Quellen**
von B. Tetzlaff (2009), 149 Seiten
ISBN: 978-3-89336-557-9

30. **Nickelreaktivlot / Oxidkeramik – Fügungen als elektrisch isolierende Dichtungskonzepte für Hochtemperatur-Brennstoffzellen-Stacks**
von S. Zügner (2009), 136 Seiten
ISBN: 978-3-89336-558-6

31. **Langzeitbeobachtung der Dosisbelastung der Bevölkerung in radioaktiv kontaminierten Gebieten Weißrusslands – Korma-Studie**
von H. Dederichs, J. Pillath, B. Heuel-Fabianek, P. Hill, R. Lennartz (2009), Getr. Pag.
ISBN: 978-3-89336-532-3

32. **Herstellung von Hochtemperatur-Brennstoffzellen über physikalische Gasphasenabscheidung**
von N. Jordán Escalona (2009), 148 Seiten
ISBN: 978-3-89336-532-3

33. **Real-time Digital Control of Plasma Position and Shape on the TEXTOR Tokamak**
by M. Mitri (2009), IV, 128 pages
ISBN: 978-3-89336-567-8

34. **Freisetzung und Einbindung von Alkalimetallverbindungen in kohlebefeuerten Kombikraftwerken**
von M. Müller (2009), 155 Seiten
ISBN: 978-3-89336-568-5

35. **Kosten von Brennstoffzellensystemen auf Massenbasis in Abhängigkeit von der Absatzmenge**
von J. Werhahn (2009), 242 Seiten
ISBN: 978-3-89336-569-2

36. **Einfluss von Reoxidationszyklen auf die Betriebsfestigkeit von anodengestützten Festoxid-Brennstoffzellen**
von M. Ettler (2009), 138 Seiten
ISBN: 978-3-89336-570-8

37. **Großflächige Plasmaabscheidung von mikrokristallinem Silizium für mikromorphe Dünnschichtsolarmodule**
von T. Kilper (2009), XVII, 154 Seiten
ISBN: 978-3-89336-572-2

38. **Generalized detailed balance theory of solar cells**
by T. Kirchartz (2009), IV, 198 pages
ISBN: 978-3-89336-573-9

39. **The Influence of the Dynamic Ergodic Divertor on the Radial Electric Field at the Tokamak TEXTOR**
von J. W. Coenen (2009), xii, 122, XXVI pages
ISBN: 978-3-89336-574-6

40. **Sicherheitstechnik im Wandel Nuklearer Systeme**
von K. Nünighoff (2009), viii, 215 Seiten
ISBN: 978-3-89336-578-4

41. **Pulvermetallurgie hochporöser NiTi-Legierungen für Implanat- und Dämpfungsanwendungen**
von M. Köhl (2009), XVII, 199 Seiten
ISBN: 978-3-89336-580-7

42. **Einfluss der Bondcoatzusammensetzung und Herstellungsparameter auf die Lebensdauer von Wärmedämmschichten bei zyklischer Temperaturbelastung**
von M. Subanovic (2009), 188, VI Seiten
ISBN: 978-3-89336-582-1

43. **Oxygen Permeation and Thermo-Chemical Stability of Oxygen Permeation Membrane Materials for the Oxyfuel Process**
by A. J. Ellett (2009), 176 pages
ISBN: 978-3-89336-581-4

44. **Korrosion von polykristallinem Aluminiumoxid (PCA) durch Metalljodidschmelzen sowie deren Benetzungseigenschaften**
von S. C. Fischer (2009), 148 Seiten
ISBN: 978-3-89336-584-5

45. **IEF-3 Report 2009. Basic Research for Applications**
(2009), 217 Seiten
ISBN: 978-3-89336-585-2

46. **Verbundvorhaben ELBASYS (Elektrische Basissysteme in einem CFK-Rumpf) - Teilprojekt: Brennstoffzellenabgase zur Tankinertisierung - Schlussbericht**
von R. Peters, J. Latz, J. Pasel, R. C. Samsun, D. Stolten
(2009), xi, 202 Seiten
ISBN: 978-3-89336-587-6

47. **Aging of ^{14}C-labeled Atrazine Residues in Soil: Location, Characterization and Biological Accessibility**
by N. D. Jablonowski (2009), IX, 104 pages
ISBN: 978-3-89336-588-3

48. **Entwicklung eines energetischen Sanierungsmodells für den europäischen Wohngebäudesektor unter dem Aspekt der Erstellung von Szenarien für Energie- und CO_2 - Einsparpotenziale bis 2030**
von P. Hansen (2009), XXII, 281 Seiten
ISBN: 978-3-89336-590-6

49. **Reduktion der Chromfreisetzung aus metallischen Interkonnektoren für Hochtemperaturbrennstofzellen durch Schutzschichtsysteme**
von R. Trebbels (2009), iii, 135 Seiten
ISBN: 978-3-89336-591-3

50. **Bruchmechanische Untersuchung von Metall / Keramik-Verbundsystemen für die Anwendung in der Hochtemperaturbrennstoffzelle**
von B. Kuhn (2009), 118 Seiten
ISBN: 978-3-89336-592-0

51. **Wasserstoff-Emissionen und ihre Auswirkungen auf den arktischen Ozonverlust**
Risikoanalyse einer globalen Wasserstoffwirtschaft
von T. Feck (2009), 180 Seiten
ISBN: 978-3-89336-593-7

52. **Development of a new Online Method for Compound Specific Measurements of Organic Aerosols**
by T. Hohaus (2009), 156 pages
ISBN: 978-3-89336-596-8

53. **Entwicklung einer FPGA basierten Ansteuerungselektronik für Justageeinheiten im Michelson Interferometer**
von H. Nöldgen (2009), 121 Seiten
ISBN: 978-3-89336-599-9

54. **Observation – and model – based study of the extratropical UT/LS**
by A. Kunz (2010), xii, 120, xii pages
ISBN: 978-3-89336-603-3

55. **Herstellung polykristalliner Szintillatoren für die Positronen-Emissions-Tomographie (PET)**
von S. K. Karim (2010), VIII, 154 Seiten
ISBN: 978-3-89336-610-1

56. **Kombination eines Gebäudekondensators mit H2-Rekombinatorelementen in Leichwasserreaktoren**
von S. Kelm (2010), vii, 119 Seiten
ISBN: 978-3-89336-611-8

57. **Plant Leaf Motion Estimation Using A 5D Affine Optical Flow Model**
by T. Schuchert (2010), X, 143 pages
ISBN: 978-3-89336-613-2

58. **Tracer-tracer relations as a tool for research on polar ozone loss**
by R. Müller (2010), 116 pages
ISBN: 978-3-89336-614-9

59. **Sorption of polycyclic aromatic hydrocarbon (PAH) to Yangtze River sediments and their components**
by J. Zhang (2010), X, 109 pages
ISBN: 978-3-89336-616-3

60. **Weltweite Innovationen bei der Entwicklung von CCS-Technologien und Möglichkeiten der Nutzung und des Recyclings von CO_2**
Studie im Auftrag des BMWi
von W. Kuckshinrichs et al. (2010), X, 139 Seiten
ISBN: 978-3-89336-617-0

61. **Herstellung und Charakterisierung von sauerstoffionenleitenden Dünnschichtmembranstrukturen**
von M. Betz (2010), XII, 112 Seiten
ISBN: 978-3-89336-618-7

62. **Politikszenarien für den Klimaschutz V – auf dem Weg zum Strukturwandel, Treibhausgas-Emissionsszenarien bis zum Jahr 2030**
hrsg. von P. Hansen, F. Chr. Matthes (2010), 276 Seiten
ISBN: 978-3-89336-619-4

63. **Charakterisierung Biogener Sekundärer Organischer Aerosole mit Statistischen Methoden**
von C. Spindler (2010), iv, 163 Seiten
ISBN: 978-3-89336-622-4

64. **Stabile Algorithmen für die Magnetotomographie an Brennstoffzellen**
von M. Wannert (2010), ix, 119 Seiten
ISBN: 978-3-89336-623-1

65. **Sauerstofftransport und Degradationsverhalten von Hochtemperaturmembranen für CO2-freie Kraftwerke**
von D. Schlehuber (2010), VII, 139 Seiten
ISBN: 978-3-89336-630-9

66. **Entwicklung und Herstellung von foliengegossenen, anodengestützten Festoxidbrennstoffzellen**
von W. Schafbauer (2010), VI, 164 Seiten
ISBN: 978-3-89336-631-6

67. **Disposal strategy of proton irradiated mercury from high power spallation sources**
by S. Chiriki (2010), xiv, 124 pages
ISBN: 978-3-89336-632-3

68. **Oxides with polyatomic anions considered as new electrolyte materials for solid oxide fuel cells (SOFCs)**
by O. H. Bin Hassan (2010), vii, 121 pages
ISBN: 978-3-89336-633-0

69. **Von der Komponente zum Stack: Entwicklung und Auslegung von HT-PEFC-Stacks der 5 kW-Klasse**
von A. Bendzulla (2010), IX, 203 Seiten
ISBN: 978-3-89336-634-7

70. **Satellitengestützte Schwerewellenmessungen in der Atmosphäre und Perspektiven einer zukünftigen ESA Mission (PREMIER)**
von S. Höfer (2010), 81 Seiten
ISBN: 978-3-89336-637-8

71. **Untersuchungen der Verhältnisse stabiler Kohlenstoffisotope in atmosphärisch relevanten VOC in Simulations- und Feldexperimenten**
von H. Spahn (2010), IV, 210 Seiten
ISBN: 978-3-89336-638-5

72. **Entwicklung und Charakterisierung eines metallischen Substrats für nanostrukturierte keramische Gastrennmembranen**
von K. Brands (2010), vii, 137 Seiten
ISBN: 978-3-89336-640-8

73. **Hybridisierung und Regelung eines mobilen Direktmethanol-Brennstoffzellen-Systems**
von J. Chr. Wilhelm (2010), 220 Seiten
ISBN: 978-3-89336-642-2

74. **Charakterisierung perowskitischer Hochtemperaturmembranen zur Sauerstoffbereitstellung für fossil gefeuerte Kraftwerksprozesse**
von S.A. Möbius (2010) III, 208 Seiten
ISBN: 978-3-89336-643-9

75. **Characterization of natural porous media by NMR and MRI techniques: High and low magnetic field studies for estimation of hydraulic properties**
by L.-R. Stingaciu (2010), 96 pages
ISBN: 978-3-89336-645-3

76. **Hydrological Characterization of a Forest Soil Using Electrical Resistivity Tomography**
by Chr. Oberdörster (2010), XXI, 151 pages
ISBN: 978-3-89336-647-7

77. **Ableitung von atomarem Sauerstoff und Wasserstoff aus Satellitendaten und deren Abhängigkeit vom solaren Zyklus**
von C. Lehmann (2010), 127 Seiten
ISBN: 978-3-89336-649-1

78. **18th World Hydrogen Energy Conference 2010 – WHEC2010 Proceedings**
Speeches and Plenary Talks
ed. by D. Stolten, B. Emonts (2010)
ISBN: 978-3-89336-658-3

78-1. **18th World Hydrogen Energy Conference 2010 – WHEC2010 Proceedings**
Parallel Sessions Book 1:
Fuel Cell Basics / Fuel Infrastructures
ed. by D. Stolten, T. Grube (2010), ca. 460 pages
ISBN: 978-3-89336-651-4

78-2. **18th World Hydrogen Energy Conference 2010 – WHEC2010 Proceedings**
Parallel Sessions Book 2:
Hydrogen Production Technologies – Part 1
ed. by D. Stolten, T. Grube (2010), ca. 400 pages
ISBN: 978-3-89336-652-1

78-3. **18th World Hydrogen Energy Conference 2010 – WHEC2010 Proceedings**
Parallel Sessions Book 3:
Hydrogen Production Technologies – Part 2
ed. by D. Stolten, T. Grube (2010), ca. 640 pages
ISBN: 978-3-89336-653-8

78-4. **18th World Hydrogen Energy Conference 2010 – WHEC2010 Proceedings**
Parallel Sessions Book 4:
Storage Systems / Policy Perspectives, Initiatives and Cooperations
ed. by D. Stolten, T. Grube (2010), ca. 500 pages
ISBN: 978-3-89336-654-5

78-5. **18th World Hydrogen Energy Conference 2010 – WHEC2010 Proceedings**
Parallel Sessions Book 5:
Stategic Analysis / Safety Issues / Existing and Emerging Markets
ed. by D. Stolten, T. Grube (2010), ca. 530 pages
ISBN: 978-3-89336-655-2

78-6. **18th World Hydrogen Energy Conference 2010 – WHEC2010 Proceedings**
Parallel Sessions Book 6:
Stationary Applications / Transportation Applications
ed. by D. Stolten, T. Grube (2010), ca. 330 pages
ISBN: 978-3-89336-656-9

78 Set (complete book series)

18th World Hydrogen Energy Conference 2010 – WHEC2010 Proceedings
ed. by D. Stolten, T. Grube, B. Emonts (2010)
ISBN: 978-3-89336-657-6

79. **Ultrafast voltex core dynamics investigated by finite-element micromagnetic simulations**
by S. Gliga (2010), vi, 144 pages
ISBN: 978-3-89336-660-6

80. **Herstellung und Charakterisierung von keramik- und metallgestützten Membranschichten für die CO_2-Abtrennung in fossilen Kraftwerken**
von F. Hauler (2010), XVIII, 178 Seiten
ISBN: 978-3-89336-662-0

81. **Experiments and numerical studies on transport of sulfadiazine in soil columns**
by M. Unold (2010), xvi, 115 pages
ISBN: 978-3-89336-663-7

82. **Prompt-Gamma-Neutronen-Aktivierungs-Analyse zur zerstörungsfreien Charakterisierung radioaktiver Abfälle**
von J.P.H. Kettler (2010), iv, 205 Seiten
ISBN: 978-3-89336-665-1

83. **Transportparameter dünner geträgerter Kathodenschichten der oxidkeramischen Brennstoffzelle**
von C. Wedershoven (2010), vi, 137 Seiten
ISBN: 978-3-89336-666-8

84. **Charakterisierung der Quellverteilung von Feinstaub und Stickoxiden in ländlichem und städtischem Gebiet**
von S. Urban (2010), vi, 211 Seiten
ISBN: 978-3-89336-669-9

85. **Optics of Nanostructured Thin-Film Silicon Solar Cells**
by C. Haase (2010), 150 pages
ISBN: 978-3-89336-671-2

86. **Entwicklung einer Isolationsschicht für einen Leichtbau-SOFC-Stack**
von R. Berhane (2010), X, 162 Seiten
ISBN: 978-3-89336-672-9

87. **Hydrogen recycling and transport in the helical divertor of TEXTOR**
by M. Clever (2010), x, 172 pages
ISBN: 978-3-89336-673-6

88. **Räumlich differenzierte Quantifizierung der N- und P-Einträge in Grundwasser und Oberflächengewässer in Nordrhein-Westfalen unter besonderer Berücksichtigung diffuser landwirtschaftlicher Quellen**
von F. Wendland et. al. (2010), xii, 216 Seiten
ISBN: 978-3-89336-674-3

89. **Oxidationskinetik innovativer Kohlenstoffmaterialien hinsichtlich schwerer Lufteinbruchstörfälle in HTR´s und Graphitentsorgung oder Aufarbeitung**
von B. Schlögl (2010), ix, 117 Seiten
ISBN: 978-3-89336-676-7

90. **Chemische Heißgasreinigung bei Biomassenvergasungsprozessen**
von M. Stemmler (2010), xv, 196 Seiten
ISBN: 978-3-89336-678-1

91. **Untersuchung und Optimierung der Serienverschaltung von Silizium-Dünnschicht-Solarmodulen**
von S. Haas (2010), ii, 202 Seiten
ISBN: 978-3-89336-680-4

92. **Non-invasive monitoring of water and solute fluxes in a cropped soil**
by S. Garré (2010), xxiv, 133 pages
ISBN: 978-3-89336-681-1

93. **Improved hydrogen sorption kinetics in wet ball milled Mg hydrides**
by L. Meng (2011), II, 119 pages
ISBN: 978-3-89336-687-3

94. **Materials for Advanced Power Engineering 2010**
ed. by J. Lecomte-Beckers, Q. Contrepois, T. Beck and B. Kuhn
(2010), 1327 pages
ISBN: 978-3-89336-685-9

95. **2D cross-hole MMR – Survey design and sensitivity analysis for cross-hole applications of the magnetometric resistivity**
by D. Fielitz (2011), xvi, 123 pages
ISBN: 978-3-89336-689-7

96. **Untersuchungen zur Oberflächenspannung von Kohleschlacken unter Vergasungsbedingungen**
von T. Melchior (2011), xvii, 270 Seiten
ISBN: 978-3-89336-690-3

97. **Secondary Organic Aerosols: Chemical Aging, Hygroscopicity, and Cloud Droplet Activation**
by A. Buchholz (2011), xiv, 134 pages
ISBN: 978-3-89336-691-0

98. **Chrom-bezogene Degradation von Festoxid-Brennstoffzellen**
von A. Neumann (2011), xvi, 218 Seiten
ISBN: 978-3-89336-692-7

99. **Amorphous and microcrystalline silicon applied in very thin tandem solar cells**
by S. Schicho (2011), XII, 190 pages
ISBN: 978-3-89336-693-4

100. **Sol-gel and nano-suspension electrolyte layers for high performance solid oxide fuel cells**
by F. Han (2011), iv, 131 pages
ISBN: 978-3-89336-694-1

101. **Impact of different vertical transport representations on simulating processes in the tropical tropopause layer (TTL)**
by F. Plöger (2011), vi, 104 pages
ISBN: 978-3-89336-695-8

102. **Untersuchung optischer Nanostrukturen für die Photovoltaik mit Nahfeldmikroskopie**
von T. Beckers (2011), xiii, 128 Seiten
ISBN: 978-3-89336-696-5

103. **Impact of contamination on hydrogenated amorphous silicon thin films & solar cells**
by J. Wördenweber (2011), XIV, 138 pages
ISBN: 978-3-89336-697-2

104. **Water and Organic Nitrate Detection in an AMS: Laboratory Characterization and Application to Ambient Measurements**
by A. Mensah (2011), XI, 111 pages
ISBN: 978-3-89336-698-9

105. **Entwicklung eines neuen Konzepts zur Steuerung der thermischen Ausdehnung von glaskeramischen Verbundwerkstoffen mit angepasster Fließfähigkeit am Beispiel der Hochtemperatur-Brennstoffzelle**
von E. Wanko (2011), xi, 134 Seiten
ISBN: 978-3-89336-705-4

106. **Tomographic reconstruction of atmospheric volumes from infrared limb-imager measurements**
by J. Ungermann (2011), xiv, 153 pages
ISBN: 978-3-89336-708-5

107. **Synthese und Identifizierung von substituierten Mg-Al-Cl Doppelhydroxidverbindungen mit Schwerpunkt IR-Spektroskopie**
von B. Hansen (2011), XII, 121 Seiten
ISBN: 978-3-89336-709-2

108. **Analysis of spatial soil moisture dynamics using wireless sensor networks**
by U. Rosenbaum (2011), xxii, 120 pages
ISBN: 978-3-89336-710-8

109. **Optimierung von APS-ZrO2-Wärmedämmschichten durch Variation der Kriechfestigkeit und der Grenzflächenrauhigkeit**
von M. E. Schweda (2011), 168 Seiten
ISBN: 978-3-89336-711-5

110. **Sorption of a branched nonylphenol isomer and perfluorooctanoic acid on geosorbents and carbon nanotubes**
by C. Li (2011), X, 102 pages
ISBN: 978-3-89336-716-0

111. **Electron Transport in the Plasma Edge with Rotating Resonant Magnetic Perturbations at the TEXTOR Tokamak**
by H. Stoschus (2011), iv, 113 pages
ISBN: 978-3-89336-718-4

112. **Diffusion and Flow Investigations in Natural Porous Media by Nuclear Magnetic Resonance**
by N. Spindler (2011), viii, 144 pages
ISBN: 978-3-89336-719-1

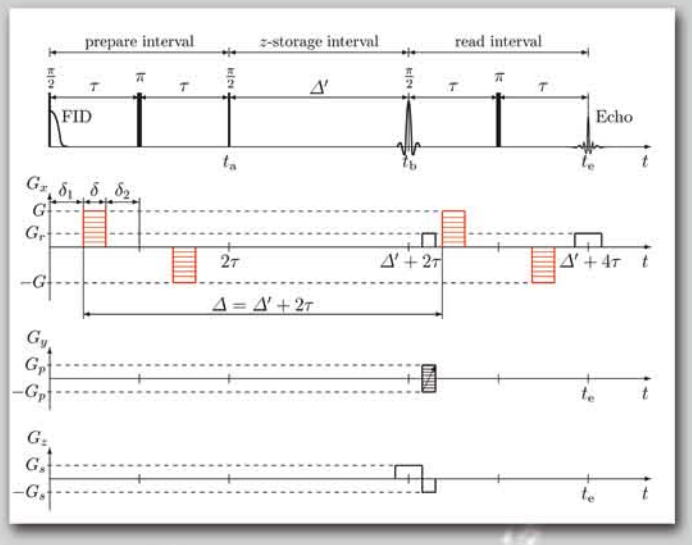

Energie & Umwelt / Energy & Environment
Band / Volume 112
ISBN 978-3-89336-719-1

JÜLICH
FORSCHUNGSZENTRUM